Symmetric 6,6′-Biazulenic π-Linkers Asymmetrically Terminated Along Their Molecular Axes

By

Xavier Alexis Ortiz-Medina © 2021

Submitted to the graduate degree program in the Department of Chemistry and the Graduate Faculty of the University of Kansas in partial fulfillment of the requirements for the degree of Master of Science.

_____

Co-Chair: Dr. Mikhail V. Barybin

_____

Co-Chair: Dr. Cindy L. Berrie

_____

Dr. James D. Blakemore

_____

Dr. Timothy A. Jackson

Date Defended: May 17th, 2021

The thesis committee for Xavier Alexis Ortiz-Medina certifies that this is the approved version
of the following thesis:

Symmetric 6,6′-Biazulenic π-Linkers Asymmetrically Terminated Along Their Molecular Axes

_____

Co-Chair: Dr. Mikhail V. Barybin

_____

Co-Chair: Dr. Cindy L. Berrie

Date Approved: May 17th, 2021

Abstract

During the past four decades, the field of molecular electronics relied on the design of molecules capable of fulfilling the roles of electronic components such as wires, diodes, and rectifiers. The work described in this thesis involved developing a synthetic strategy to build linear 6,6′-biazulenic π-linkers asymmetrically terminated with mercapto and cyano groups along their molecular axes as well as probing electronic coupling of the azulenic sub-units of several asymmetrically substituted 6,6′-biazulene derivatives by cyclic voltammetry and infrared spectroscopy.

Chapter I discusses self-assembled monolayers of organic molecules chemisorbed to Au(111) surfaces through thiolate junctions, with special emphasis on the thiolate-gold coordination and factors affecting monolayer formation. Thin film characterization methods employed in this thesis, including reflection-absorption infrared spectroscopy (RAIRS) and optical ellipsometry, are also discussed. An example of how RAIRS selection rules are used to characterize orientation and packing of self-assembled monolayers with respect to gold surfaces is provided.

Chapter II offers background on the reactivity and physicochemical properties of azulene followed by a discussion of silicon-based electronic components and their possible molecular counterparts. Applications of azulenic and biazulenic derivatives as potential wires and diodes are considered, particularly those featuring asymmetrically substituted 6,6′-biazulenic motifs. An overview of self-assembly of 6,6′-biazulenic derivatives through isocyano and thiolate junctions on Au(111) surfaces is provided, focusing on using RAIRS and ellipsometry to investigate packing within these monolayer films and orientation of their molecular constituents with respect to the gold surface.

Chapter III describes a synthetic approach to asymmetrically functionalize the 6,6′-biazulenic scaffold with cyano (-CN) and mercapto (-SH) groups at the 2 and 2′ positions of the 6,6′-biazulenic scaffold. Spectroscopic characterization of the asymmetrically substituted 6,6′-biazulenic precursors is discussed, as well as the changes in electronic absorption caused by different functionalities along the molecular axis of the biazulenic scaffold. The extent of electronic coupling between the azulenic sub-units of the 6,6′-biazulenic π-linker is also explored

through cyclic voltammetry and infrared spectroscopy. Experiments on the self-assembly of the -SH and -CN functionalized 6,6′-biazulene on Au(111) are outlined and discussed. However, attempts at gathering IR spectroscopic and ellipsometric evidence of monolayer formation were unsuccessful. Several experimental suggestions are offered for future work on self-assembly of the aforementioned π-linker.

The final chapter of this thesis summarizes key conclusions and offers future work suggestions pertaining to the new 6,6′-biazulenic π-linker described in Chapter III towards a better understanding of its applicability in the field of molecular electronics. The experimental suggestions include several changes to the conditions for monolayer formation, conductivity measurements to be performed with conductive atomic force microscopy, and probing electron transport dynamics using Auger electron spectroscopy. Additionally, several synthetic alternatives to the synthesis used in chapter III are explored with the goal of improving atom economy and increasing overall yields.

Acknowledgements

First and foremost, I would like to thank Professor Mikhail (Misha) Barybin and Professor Cindy Berrie. Your support, mentorship, and guidance through the last three years have been amazing and I never imagined how spectacularly both of you would impact my life. I owe you a great deal of gratitude for helping me develop my scientific and personal skills to become the person I am today. You are absolutely amazing people, and it has been an honor working with you both!

Before undergraduate and graduate studies, I would like to thank my high school teachers. Thank you to Melissa Sedwick and Charles Effinger for igniting my passion for chemistry by making learning fun and engaging. Thanks to Stacey Peters for making derivatives and integrals fun for high school student! I still remember…low d high, minus high d low, over low low! Thank you to Scott Johnson and Michael Carpenter for giving me a place where I felt like I belonged even if everything was unfamiliar to me at the time and thank you for helping me develop the work ethic that got me here in the first place.

To Dr. Brad Neal, I can't thank you enough for showing me the 2016 Chem. Sci. paper and for your guidance during my final year at the University of Indianapolis. It was your undeniable passion for chemistry that inspired me to do research at the University of Kansas with my current "bosses." To Dr. Levi Mielke and Dr. Steve Spicklemire, thank you for your patience, mentorship, and everything you taught me, your advice has been invaluable through my graduate career.

I would also like to thank the chemistry department at the University of Kansas. My time here has been wonderful and all of you have contributed to that. It has been an honor serving as a teaching assistant under Dr. Mikhail (Misha) Barybin, Dr. David Weis, Dr. Drew Vartia, Dr. Roderick Black, and Dr. Marina Rubin. I have learned so much from all of you and I am sure that the skills I have acquired in the classroom or in the labs will be invaluable to me in the future. Thank you to Sarah Neuenswander and Dr. Justin Douglas for all the assistance with NMR facilities. Thanks to Dr. Victor Day for trying his best to acquire data from my poorly form crystals. A special thank you to Dr. Timothy Jackson and Dr. James Blakemore for agreeing to serve in my defense committee.

I owe a huge thank you to all of the past and current members of the Barybin and Berrie groups, it has been amazing working with you all! Thank you, Jason, Nate, Moni, David, Tu,

Georgii, Patrick, Shawn, Levi, Sasanka, Nilan, Jen, Yasmine, Sam, Tyler, and Sarah for the time in and outside of the group activities. I specially need to thank Jason for showing me the basics in the Barybin lab, and Sasanka and Nilan for walking me through all of the instrumentation in the Berrie lab. Thank you to the Blakemore and Jackson groups for their comradery and all your advice through the years. Special thanks to Wade Hanke and Amit Kumar for all of your help with crystallography. You guys are awesome!

A mis padres, gracias por todos los sacrificios que han hecho para que Kevin, Izander, y yo salgamos adelante con un mejor futuro. Gracias por todo su apoyo durante mis estudios y espero que estén felices con el camino que llevamos cada uno. Ustedes son mi inspiración y la razón por la cual tengo los valores que me hacen la persona que soy, y por eso estoy extremadamente orgulloso de ser su hijo. ¡Gracias a ambos, los amo mucho!

Nicole, you have been there for me since the beginning of this adventure, and I would like to thank you for all your love, support, and patience. You have been incredibly kind and supportive through the most difficult times of my life. Thank you. To my baby boy, I can't wait to meet you! I am so excited and grateful for my family! I love you all and I am looking forward to our future.

Table of Contents

List of Figures

List of Schemes

Abbreviations

AC – Alternating Current

ADC – Analog-to-Digital Converter

AFM – Atomic Force Microscopy

C-AFM – Conductive Atomic Force Microscopy

COC – Core-hole-clock

CV – Cyclic Voltammetry

DBU – 1,8-diazabicyclo[5.4.0]undec-7-ene

DC – Direct Current

DIBA – 1,1′,3,3′-Tetraethoxicarbonyl-2,2′-diisocyano-6,6′-biazulene

DMA – 2,6-dimercaptoazylenyl-1,3-dicarboxylate

EDG – Electron Donating Group

EWG – Electron Withdrawing Group

FMO – Frontier Molecular Orbital

FTIR – Fourier Transform Infrared Spectroscopy

HOMO – Highest Occupied Molecular Orbital

LUMO – Lowest Unoccupied Molecular Orbital

PSDS – Position Sensitive Photo Detector

RAES – Resonant Auger Electron Spectroscopy

RAIRS – Reflection Absorption Infrared Spectroscopy

SAMs – Self-Assembled Monolayers

STM – Scanning Tunneling Microscopy

THF – Tetrahydrofuran

XPS – X-ray photoelectron spectroscopy

XRD – X-ray diffraction

CHAPTER I

I. An Overview of Formation, Characterization, and Physicochemical Properties of Molecular Self-Assembled Monolayers

II.1   Introduction

Self-assembled monolayers (SAM) are one-molecule thick ordered assemblies that form spontaneously by submerging a substrate into a solution of a compound that can bind to said surface.[1] Detection and characterization of SAMs can be challenging due to the limited number of molecules chemisorbed to the surface, but several analytical techniques are sensitive enough to overcome this challenge. Characterization of SAMs can be accomplished by employing the aid of ellipsometry, Reflection-Absorption Infrared (RAIR) spectroscopy, Atomic Force Microscopy (AFM), goniometry, and Scanning Tunneling Microscopy, among others, to probe the packing, orientation, and thickness of these thin films.[1]

In the past decade, the Barybin and Berrie groups have synthesized and characterized the packing and orientation of azulenic derivatives on Au(111) surfaces as they self-assemble through isocyanide or thiolate junctions.[2-6] These azulenic SAMs were primarily characterized with RAIR using spectroscopic reporters such as -CN, -NC, and [(-NC)Cr(CO)$_5$], showing that the azulenic derivatives adopt a near upright orientation with respect to the surface.[2, 4, 5] These findings were supported by agreement of ellipsometric thickness with theoretically calculated values. The goal of these studies is to apply these azulenic systems as molecular electronic components like wires, diodes, rectifiers, and electron reservoirs.[7] Self-assembly of the azulenic systems on gold surfaces provides a way of measuring electronic properties through the azulenic backbone that include conductivity, rectification, or diode-like behavior, although these properties are still to be measured. This work utilizes these same spectroscopic and ellipsometric techniques to probe self-assembly, packing, and orientation of a newly synthesized biazulenic π-linker, which is asymmetrically substituted with cyano (-CN) and mercapto (-SH) functionalities, on Au(111) surfaces.

I.2   Self-Assembled Monolayers

Self-assembled monolayers have played a crucial role in surface chemistry with applications towards molecular electronics in the past 40 years.[1, 6, 8] The potential ease of formation, reliability, and reproducibility make self-assembly an attractive method for surface chemists. SAMs form spontaneously by immersing a substrate in a solution of compounds with functionalities capable of self-assembly.[1] There are several types of substrates that produce organic monolayer and these include silicon-containing organic compounds on hydroxylated surfaces like SiO_2 on Si, and alkanethiols on gold; silver; and copper, among others.[1, 9] Gold substrates are especially attractive towards molecular electronics applications as gold is commonly used in electronic components and it also provides a conductive medium that can be used as an electrode.[10, 11] Monolayers usually have three components shown in Figure **1.1,** a junction group chemisorbed to the metal surface, a bridge or spacer group, and a surface head group. This section will discuss monolayers of alkanethiols on gold as it is more relevant to this thesis.
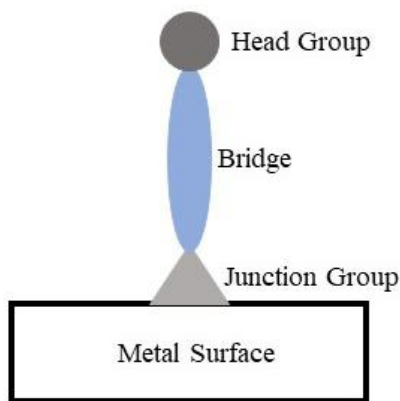
Figure 1.1. Terminology for SAMs on metal surfaces.

Self-assembly of alkanethiols on gold surfaces are among the most used thin films because of their thermal stability, strong S-Au interactions, and a lack of a stable gold oxide which allows samples to be handled in ambient conditions.[1, 9, 12] Alkanethiol SAMs usually form by immersing a freshly cleaned gold sample into a dilute solution, usually in the mM range, of the desired compound. The Au(111) plane is used more often than others due to the hexagonal symmetry and S-Au hollow-site coordination which gives these thiolate films a linear S-Au junction and optimal

S↔S distance for a densely packed upright film. Additionally, the Au(111) face is easier to manufacture since it is the energetically favorable surface. In contrast, Au(100) surfaces provide base-centered square symmetry which makes S↔S spacing problematic. To compensate for the spacing, the molecules chemisorbed to the surface adopt a tilt angle of about 32° which affects the packing density on the gold surface.[8, 13] There are several important factors to consider when performing these experiments, mainly the gold lattice, immersion times, and concentration of the compound itself in solution.

The solution concentration plays an important role in how well monolayers from. Solutions that are dilute (~10^{-3}M) tend to form more densely packed monolayers than their more concentrated counter parts.[1, 14] In a more concentrated medium there are more molecules per unit volume which gives rise to more electrostatic interactions. These interactions will possibly create large clumps deposited on the surface producing multilayer structures which would reduce the packing density.[15]

Another important factor to consider is immersion time. The kinetics of monolayer formation of alkanethiols on gold is varied and depends on the identity of the compound. A study done by Bain *et al.* found that alkanethiol monolayer formation takes place in two kinetic steps: a fast step by which the contact angles come close to their limiting values and thicknesses close to maximum values, and a slow step in which the thicknesses and contact angles reach their final value.[1, 16] This is depicted in Figure **1.2.** showing kinetics of absorption of octadecanethiol in ethanol onto gold as a function of concentration. In all, it takes a few minutes to a few hours to form alkanethiol monolayers.
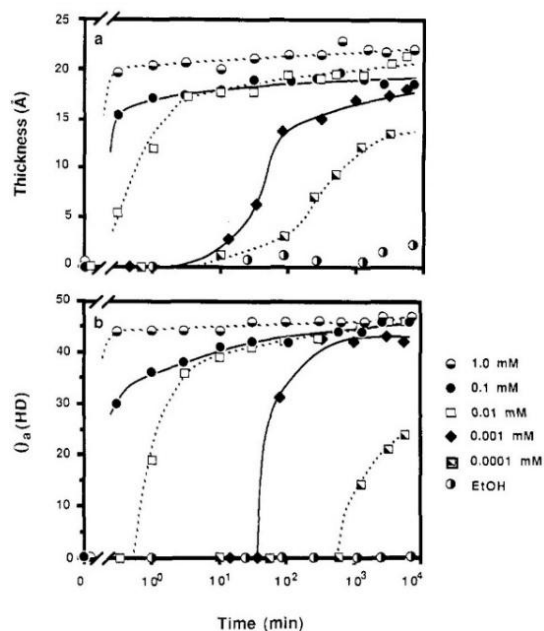
Figure 1.2. Kinetics of absorption of octadecanethiol in ethanol onto gold as a function of concentration: (a) thickness, (b) contact angle. (Reproduced with permission from Bain *et al.* © 1989, J. Am. Chem. Soc.)[16]

Alkanethiols chemisorption onto gold surfaces is still being studied and it is not completely understood.[1, 13] The process of SAM formation of alkanethiols involves physisorption onto the surface followed by chemisorption through the sulfur to the gold surface.[13] Figure **1.3** shows a simple depiction of how this process takes place where gray are free molecules and red shows molecules chemisorbed to the surface.
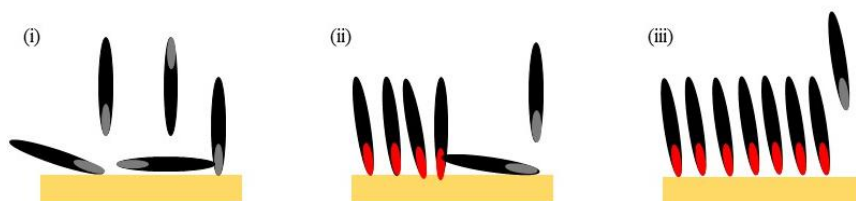
Figure 1.3. Depiction of self-assembly of alkanethiols on gold. (i) physisorption, (ii) nucleation phase, (iii) completion of upright phase.[13]

The currently accepted mechanism for the formation of alkanethiol monolayers involves oxidative adsorption of the RS-H bond to the gold substrate following the reactions below.[1, 13, 16] However, there is still a debate on whether the mechanism of the S-H bond cleavage involves homolytic or, ionic pathway, or a combination thereof.[1, 13, 17]

$$RSH + Au \rightarrow (RSH)_{phys}Au \quad (a)$$

$$(RSH)_{phys}Au \rightarrow RS{-}Au + 1/2H_2 \quad (b)$$

Although there is evidence by XPS, vibrational spectroscopy, mass spectrometry, and electrochemical techniques to support the formation of Au—S bonds in which the sulfur exists as a thiolate, there is still uncertainty on the fate of the thiol hydrogen. The most common hypothesis is that the hydrogen atoms of the mercapto groups react to form H_2, but the amount of hydrogen formed is about 10^{14} H_2 molecules for a 1 cm^2 Au(111) sample which makes detection extremely challenging. It has also been proposed that hydrogen atoms could react with the surface to yield metal hydrides, and if combined with an oxidant, the hydrogen atoms might react to form water or hydrogen peroxide.[13, 17] However, there is no concrete evidence to date to confirm any of these hypotheses.

The surface lattice dictates the orientation of the thin film with respect to the metal surface.[18] As mentioned before, Au(111) provides the optimal S↔S distance to form linear S-Au bonds. This work uses Au (111) as substrate for thiol monolayer formation. The term Au (111) describes the (111) face of the gold crystal lattice. Crystalline gold adopts a face-centered cubic crystal structure, and the Miller indices specify where the plane of the surface will intercept the x-, y-, and z- coordinates of the unit cell as shown in Figure **1.4.**[19]
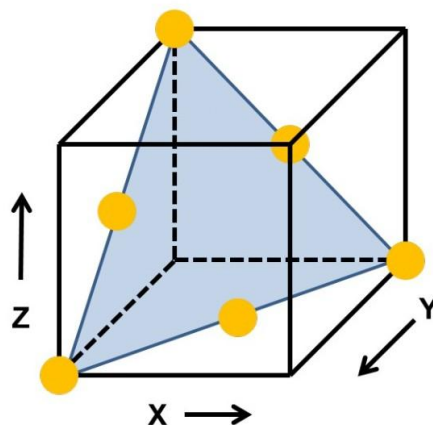
Figure 1.4. Pictorial representation of the (111) face on a fcc crystalline lattice.[18]

In an experiment performed by Strong and Whitesides, where they studied monolayers of docosanethiol using electron diffraction, it was found that the symmetry of the sulfur atoms in the monolayer of the compound on Au (111) was hexagonal with a 4.97Å spacing between sulfur atoms.[20] Following this study, Sellers *et al.* performed geometry optimizations of thiolates and methylthiolate groups on Au (111) surface models at the PECR Hartree-Fock + electron correlation (MBPT2) levels.[21] They found that sulfur binding to the hollow site of the Au (111) face is 6.03 kcal/mol more stable than the on-top coordination. Since binding to the hollow site is more stable and the distance between each hollow site is 4.99Å apart, epitaxial growth of monolayers on the hollow sites of the Au (111) surface is the accepted mode of binding for alkanethiol SAMs.[16, 19, 22, 23] Furthermore, Hoffmann and coworkers studied the orbital interactions of methylthiolate SAMs on Au(111) through various methods of interaction. In their elegant approach, they used crystal orbital overlap population (COOP) and crystal orbital Hamiltonian population (COHP) to examine the binding mode of the thiolate junction onto the Au(111) lattice and found that there was a preference for the three-point hollow coordination model as opposed to the bridge or on-top model. They also found that π-type interactions play an crucial role in the hollow site model and are maximized when the methylthiolate is oriented upright with respect to the surface.[24] Figure **1.5** shows the structure of the lattice of Au(111) as well as the binding sites for thiolate thin films.
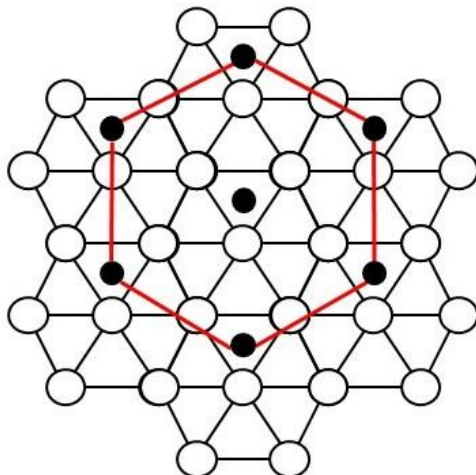
Figure 1.5. Schematic of proposed coverage of alkanethiols on Au (111) where the dark spots are sulfur atoms, and the white spots are gold atoms.

Bonding in the hollow site between gold and sulfur atoms can be explained by examining the bonding character and it involves both σ- and π- interactions. The σ-bonding comes primarily from the sulfur p-orbital and the gold 6s-orbitals, with considerable interactions from the gold p- and d- orbitals. The π-bonding arises from the gold p-orbitals interactions with sulfur and is responsible for the linear structure of the hollow site.[1, 17] Thus, S-Au bonds in hollow sites are relatively strong and stable.

Characterization methods for SAMs are extensive and range from ellipsometry, to infrared spectroscopy, to electron diffraction just to name a few. The methods involved in this thesis are mainly ellipsometry and Reflectance-Absorbance Infrared spectroscopy. A discussion of the theory of each method follows.

I.3   Optical Ellipsometry

Ellipsometry is an optical analytical technique that uses polarized light to determine the properties of thin films. Those properties can be used to determine the thickness and refractive index of molecular assemblies on a substrate.[25] This method provides a nondestructive and sensitive way to characterize thin films.
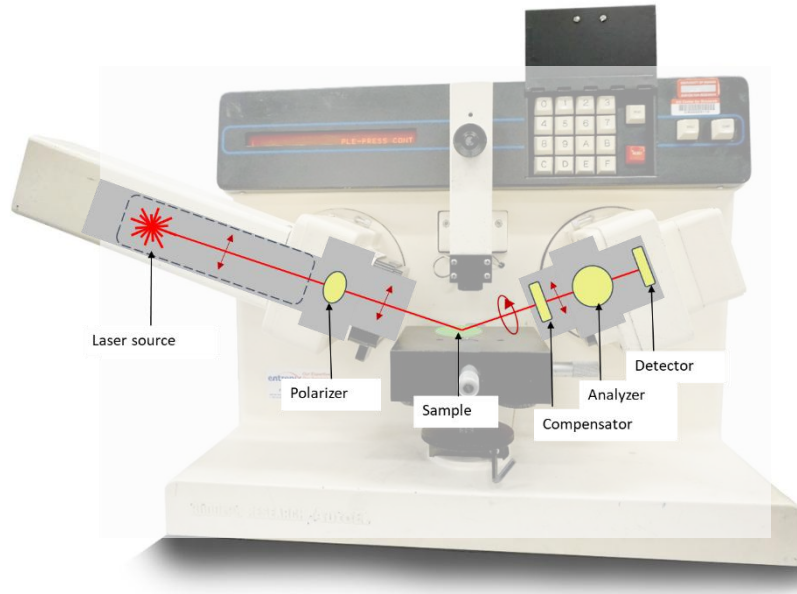
Figure 1.6 Schematic of ellipsometric experiment.[26]

Ellipsometers consist of six basic components, a light source, a polarizer, a sample, a compensator, a polarization state analyzer, and a light detector. Figure **1.6** shows the schematic of the components in an ellipsometer. The light source is commonly a He/Ne laser that produces monochromatic light. Once the beam hits the polarizer, the incident light becomes linearly plane-polarized, where the two orthogonal light waves are in phase. The compensator uses a quarter-wave plate to shift the phases of the orthogonal light waves, thus becoming elliptically polarized light and giving ellipsometry its name.[27] Figure **1.7** shows the difference in phase and amplitude of linearly and elliptically polarized light.
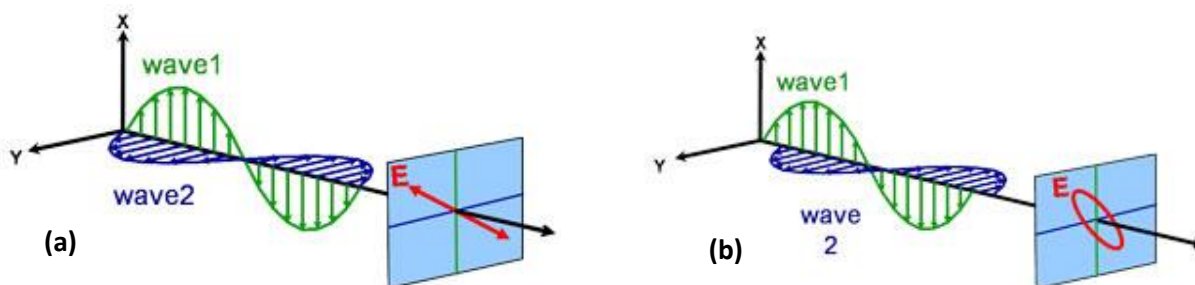
Figure 1.7 Graphical depiction of (**a**) linearly polarized light and (**b**) elliptically polarized light.[28]

The elliptically polarized light then strikes, interacts, and reflects off the sample, thus changing the polarization based on interactions with the analyte on the substrate. Next, the polarized light passes through an analyzer which rotates until a minimum signal is found by the light detector.[29] Based on the alignment of the polarizer, compensator, and analyzer the software can calculate values necessary to compute film thicknesses.

The first step in performing an ellipsometry experiment is to determine two values that are used to describe optical properties that will determine how light interacts with substances. These values are the index of refraction, n, and the extinction coefficient, k.[28] The aforementioned values are related by the complex refractive index, $\tilde{n}$, shown in Equation 1 where i is a complex number:

$$\tilde{n} = n + ik \quad (1)$$

The index of refraction describes the velocity of the light wave phases compared to the speed of light in a vacuum, c:

$$v = \frac{c}{n} \quad (2)$$

As shown in Equation 2, the phase velocity decreases as it interacts with materials of high refraction index. This effect holds the wave frequency constant, thus shortening the wavelength.[28, 29] The extinction coefficient describes the loss of wave energy to the material, and it is related to the absorption coefficient, α, by Equation 3, where λ is wavelength:

$$\alpha = \frac{4\pi k}{\lambda} \quad (3)$$
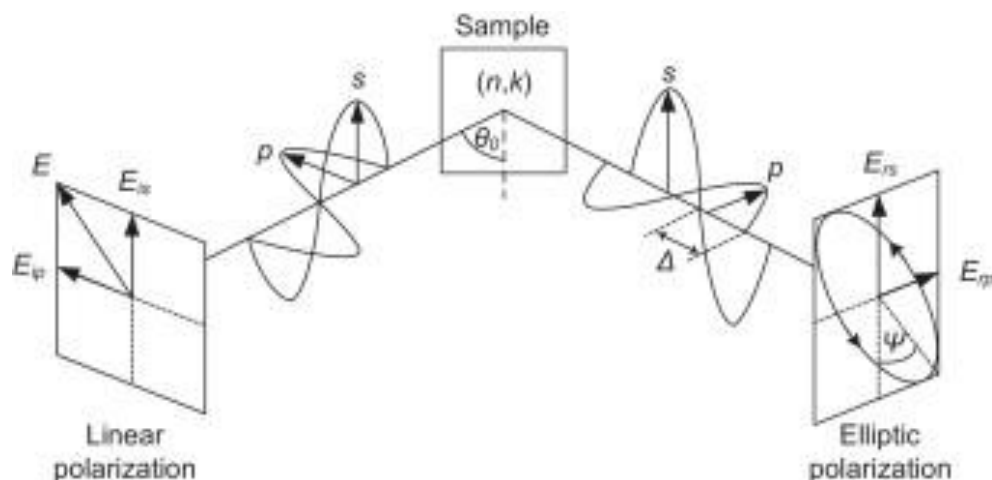
Figure 1.8. Pictorial representation of the changes that polarized light undergoes on an ellipsometry experiment.[30] Adapted with permission of Benes *et al.* © 2015 Elsevier.

Once a compound is placed on the substrate, the reflected light at angle θ changes phase and amplitude. The phase shift between the parallel and perpendicular components of the polarized light, Δ, and the change in the ratio of amplitude, ψ, are determined by the complex refractive indices of both the substrate and the thin film.[29] Once these values are determined, both *n* and *k* values can be calculated and a film thickness can be established. Figure **1.8** shows an ellipsometry experiment and how the polarized light changes in every stage. The film thicknesses in this thesis range from 1-3nm in length and ellipsometry can resolve film thicknesses at the angstrom scale, which make ellipsometry essential to characterize azulenic SAMs.

I.4   Reflection-Absorption Infrared Spectroscopy

Reflection-Absorption Infrared (RAIR) spectroscopy is an analytical technique that provides information about the orientation of transition dipoles on a substrate.[31, 32] The signal observed for this technique directly depends on the number of molecules capable of oscillating during the experiment. To increase the signal, infrared light is reflected off a surface at a high incidence angle and enhanced through polarization. With high incidence angles, there is more light covering the surface which increases the number of molecules radiated compared to a measurement taken with no angle of incidence. Figure **1.9** shows a simple optical set up for a RAIR spectrometer.
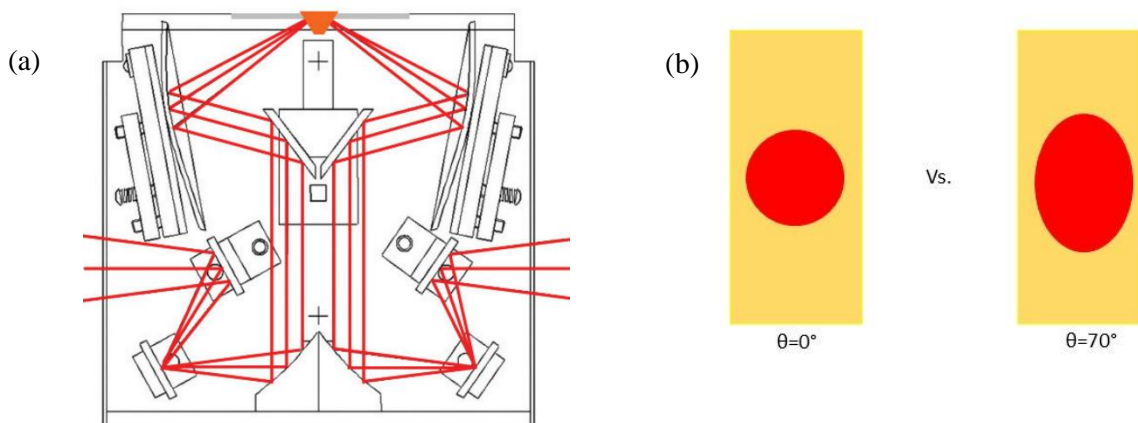
Figure 1.9. (a) Simple optical arrangement for measuring polarized reflection-absorption spectra of a thin film on a reflective surface. (b) Comparison of surface coverage of light source with and without incidence angle θ.

In the case of SAMs and other thin films on substrates, there are additional factors to consider in addition to the usual selection rules of infrared spectroscopy.[31, 32] The electric vector of the polarized light is phase shifted by reflection off a metal surface depending on the polarization. At almost all incident angles the polarized light perpendicular to the surface (s-polarized) undergoes a phase shift of π which renders the sum of the electric vectors at the surface to be near zero, thus producing no electric field. In contrast, the phase of the radiation parallel to the surface (p- polarized) is shifted by $\pi/2$ resulting in constructive vector intensities that produces a non-zero electric field and is oriented along the surface normal.[32] Figure **1.10** shows the constructive and destructive effects of the electric vectors of radiation reflected off a metal surface.
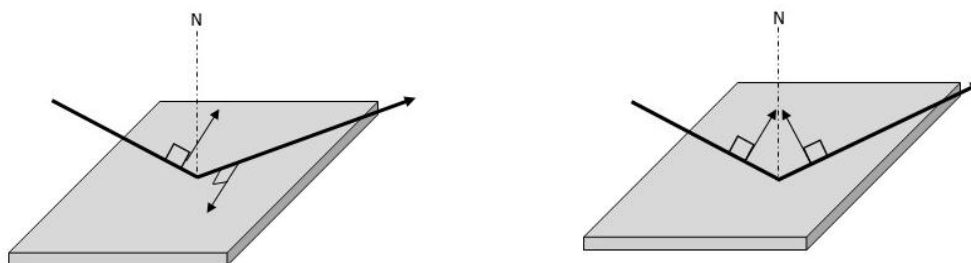
Figure 1.10. Left: Electric vectors cancel producing no electric field. Right: Electric vectors add and produce an electric field.

As a result of the phase shift of p- and s- polarized light, only monolayers or thin films that have components where the dynamic dipole moment is perpendicular to the surface normal will interact with p- polarized light and produce measurable absorption.[2, 31, 32] Using this principle, the orientation of the dipole relative to the surface can be determined. If the dipole is oriented parallel to the surface, the metal will create an image dipole and it will decrease or eliminate the expected signal. On the other hand, if the dipole is perpendicular to the surface, the image dipole from the metal will amplify the expected signal as seen in Figure **1.11**.
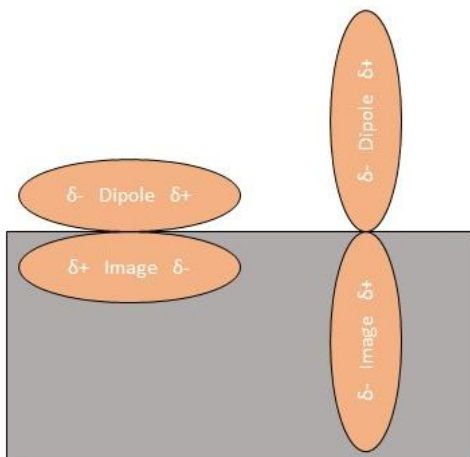
Figure 1.11. Dipoles and their corresponding images on the metal. Left: The dipole is effectively cancelled by the mirror dipole. Right: Dipoles add to intensify signal.

A great example of using RAIR selection rules was demonstrated by Applegate and Okeowo *et al.* where they used a [$Cr(CO)_5$] unit attached to an isocyanoazulenic derivative to determine the orientation of the SAMs chemisorbed by a thiolate junction onto Au (111). The solution FTIR in CH_2Cl_2 shows characteristic IR frequencies for v_{NC} band at 2140 cm^{-1} and v_{SH} band at 2583 cm^{-1}. Additionally, the usual stretching vibrational bands for carbonyl groups in a compound of shape $LM(CO)_5$ are also observed.[33] All of these features can be seen in Figure **1.12** which shows the FTIR spectra of the molecule in question in CH_2Cl_2 and in KBr.
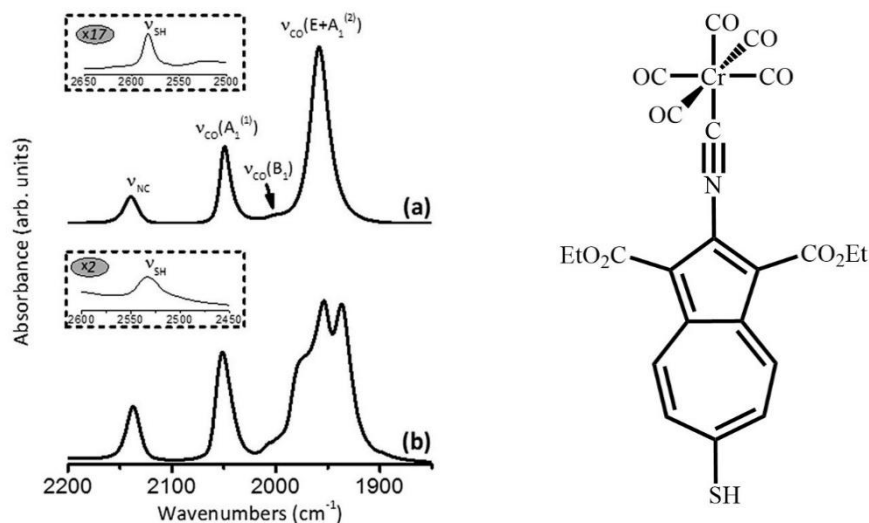
Figure 1.12. Left: FTIR spectra in (a) CH_2Cl_2 and (b) KBr.[2] Right: Molecule in question. Reproduced with permission from Barybin *et al.* © 2016 The Royal Society of Chemistry.

The observed features for the CO ligands are the $A_1^{(1)}$ band at 2059 cm^{-1} that arises from the in-phase vibrations of all the CO ligands, the B_1 band at 1992 cm^{-1} which is IR forbidden but can still be seen from a small deviation of the C_{4v} symmetry of the molecule, and the feature at 1969 cm^{-1} which is mainly attributed to the doubly degenerate E stretching mode that, in turn, obscures the $A_1^{(2)}$ mode. In the solid state, crystal packing interaction further disrupts the C_{4v} symmetry of the molecule, separating the doubly degenerate E band from the $A_1^{(2)}$ band and also eliminates the double degeneracy.[2, 19]

Once coordinated to the Au (111) surface through the thiolate junction, the RAIR spectrum shows a dramatic change compared to the solution spectrum as seen in Figure **1.13**. As seen, the intense band corresponding to the E stretching mode practically vanishes leaving behind the previously obscured $A_1^{(2)}$ band. By surface IR selection rules, this implies that the *cis*-CO ligands are approximately parallel to the surface, effectively cancelling the CO dipole with the image dipole from the gold surface. It follows that any dipole that is not perfectly perpendicular to the surface will decrease the intensity of the IR signal. These observations coupled with the relatively large intensity of the isocyanide band, which is expected to be linear, suggests a nearly upright orientation of the molecule relative to the surface.[2, 5]
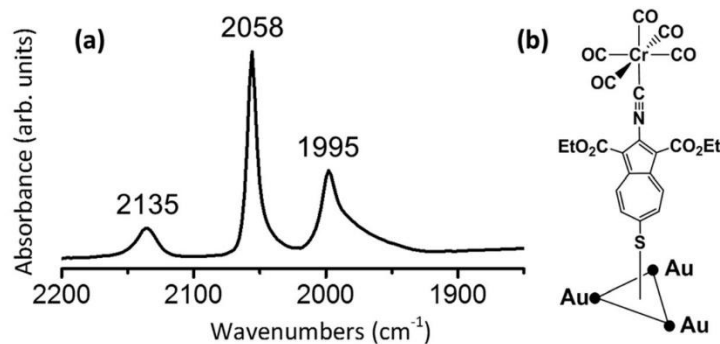
Figure 1.13. (a) RAIR spectrum of (b) coordinated to Au (111) surface.[2] Reproduced with permission from Barybin *et al.* © 2016 The Royal Society of Chemistry.

In conclusion, packing and orientation of SAMs can be characterized with a wide range of techniques. Experimental and theoretical studies have determined that linear S-Au bonds forms spontaneously on Au(111) surfaces giving thin films a near upright orientation. This thesis employs ellipsometry and RAIR spectroscopy to characterize the SAM formation, packing, and orientation of a newly synthesized 6,6'-biazulenic π-linker featuring mercapto and cyano anchoring groups towards the potential use as molecular electronic devices.

I.5   References

1.   Ulman, A., Self-Assembled Monolayers. In *An Introduction to Ultrathin Organic Films From Langmuir-Blodgett to Self-Assembly*, 1 ed.; Academic Press: San Diego, CA, 1991; pp 237-301.

2.   Applegate, J. C.; Okeowo, M. K.; Erickson, N. R.; Neal, B. M.; Berrie, C. L.; Gerasimchuk, N. N.; Barybin, M. V., First π-linker featuring mercapto and isocyano anchoring groups within the same molecule: synthesis, heterobimetallic complexation and self-assembly on Au(111). *Chemical Science* **2016,** *7* (2), 1422-1429.

3.   DuBose, D. L.; Robinson, R. E.; Holovics, T. C.; Moody, D. R.; Weintrob, E. C.; Berrie, C. L.; Barybin, M. V., Interaction of Mono- and Diisocyanoazulenes with Gold Surfaces: First Examples of Self-Assembled Monolayer Films Involving Azulenic Scaffolds. *Langmuir* **2006,** *22* (10), 4599-4606.

4.   Maher, T. R.; Spaeth, A. D.; Neal, B. M.; Berrie, C. L.; Thompson, W. H.; Day, V. W.; Barybin, M. V., Linear 6,6′-Biazulenyl Framework Featuring Isocyanide Termini: Synthesis, Structure, Redox Behavior, Complexation, and Self-Assembly on Au(111). *Journal of the American Chemical Society* **2010,** *132* (45), 15924-15926.

5.   Neal, B. M.; Vorushilov, A. S.; DeLaRosa, A. M.; Robinson, R. E.; Berrie, C. L.; Barybin, M. V., Ancillary nitrile substituents as convenient IR spectroscopic reporters for self-assembly of mercapto- and isocyanoazulenes on Au(111). *Chemical Communications* **2011,** *47* (38), 10803-10805.

6.   Wächter, T.; Scheetz, K. J.; Spaeth, A. D.; Barybin, M. V.; Zharnikov, M., Dynamics of Electron Transfer in Azulene-Based Self-Assembled Monolayers. *The Journal of Physical Chemistry C* **2017,** *121* (25), 13777-13785.

7.   Xin, H.; Hou, B.; Gao, X., Azulene-Based π-Functional Materials: Design, Synthesis, and Applications. *Accounts of Chemical Research* **2021**.

8.   Ulman, A., Formation and Structure of Self-Assembled Monolayers. *Chemical Reviews* **1996,** *96* (4), 1533-1554.

9.   Singh, M.; Kaur, N.; Comini, E., The role of self-assembled monolayers in electronic devices. *Journal of Materials Chemistry C* **2020,** *8* (12), 3938-3955.

10.   Casero, E.; Darder, M.; Díaz, D. J.; Pariente, F.; Martín-Gago, J. A.; Abruña, H.; Lorenzo, E., XPS and AFM Characterization of Oligonucleotides Immobilized on Gold Substrates. *Langmuir* **2003,** *19* (15), 6230-6235.

11.   Guo, D.-Z.; Hou, S.-M.; Zhang, G.-M.; Xue, Z.-Q., Conductance fluctuation and degeneracy in nanocontact between a conductive AFM tip and a granular surface under small-load conditions. *Applied Surface Science* **2006,** *252* (14), 5149-5157.

12.   Gschneidtner, T. A.; Diaz Fernandez, Y. A.; Moth-Poulsen, K., Progress in self-assembled single-molecule electronic devices. *Journal of Materials Chemistry C* **2013,** *1* (43), 7127-7133.

13.   Vericat, C.; Vela, M. E.; Benitez, G.; Carro, P.; Salvarezza, R. C., Self-assembled monolayers of thiols and dithiols on gold: new challenges for a well-known system. *Chemical Society Reviews* **2010,** *39* (5), 1805-1834.

14.   Wang, X.; Zeng, T.; Nourrein, M.; Lai, B.-H.; Shen, K.; Wang, C.-L.; Sun, B.; Zhu, M., Concentration-dependent self-assembly structures of an amphiphilic perylene diimide with tri(ethylene glycol) substituents at bay positions. *RSC Advances* **2017,** *7* (42), 26074-26081.

15.   Doudevski, I.; Hayes, W. A.; Woodward, J. T.; Schwartz, D. K., Atomic force microscope imaging of molecular aggregation during self-assembled monolayer growth. *Colloids and Surfaces A: Physicochemical and Engineering Aspects* **2000,** *174* (1), 233-243.

16.   Bain, C. D.; Troughton, E. B.; Tao, Y. T.; Evall, J.; Whitesides, G. M.; Nuzzo, R. G., Formation of monolayer films by the spontaneous assembly of organic thiols from solution onto gold. *Journal of the American Chemical Society* **1989,** *111* (1), 321-335.

17.   R. Colorado, J. T. R. L., Thiol Self-Assembled Monolayers: Formation and Organization. *Elsevier Encyclopedia of Materials* **2001**, 9332-9344.

18.   Neal, B. M. Self-Assembly of Azulenic Monolayer Films on Metallic Gold Surfaces. University of Kansas, Lawrence, KS, 2012.
19.   Simon, S. H., *The Oxford Solid State Basics*. Oxford University Press: United States, 2016.
20.   Strong, L.; Whitesides, G. M., Structures of self-assembled monolayer films of organosulfur compounds adsorbed on gold single crystals: electron diffraction studies. *Langmuir* **1988,** *4* (3), 546-558.
21.   Sellers, H.; Ulman, A.; Shnidman, Y.; Eilers, J. E., Structure and binding of alkanethiolates on gold and silver surfaces: implications for self-assembled monolayers. *Journal of the American Chemical Society* **1993,** *115* (21), 9389-9401.
22.   Lavrich, D. J.; Wetterer, S. M.; Bernasek, S. L.; Scoles, G., Physisorption and Chemisorption of Alkanethiols and Alkyl Sulfides on Au(111). *The Journal of Physical Chemistry B* **1998,** *102* (18), 3456-3465.
23.   O'Dwyer, C.; Gay, G.; Viaris de Lesegno, B.; Weiner, J., The Nature of Alkanethiol Self-Assembled Monolayer Adsorption on Sputtered Gold Substrates. *Langmuir* **2004,** *20* (19), 8172-8182.
24.   Tachibana, M.; Yoshizawa, K.; Ogawa, A.; Fujimoto, H.; Hoffmann, R., Sulfur−Gold Orbital Interactions which Determine the Structure of Alkanethiolate/Au(111) Self-Assembled Monolayer Systems. *The Journal of Physical Chemistry B* **2002,** *106* (49), 12727-12736.
25.   Podraza, N. J.; Jellison, G. E., Ellipsometry. In *Encyclopedia of Spectroscopy and Spectrometry (Third Edition)*, Lindon, J. C.; Tranter, G. E.; Koppenaal, D. W., Eds. Academic Press: Oxford, 2017; pp 482-489.
26.   Ulapane, S. B. Harnessing the Control of Metallic Nanostructures on Interfaces Towards Biosensing, Plasmonics and More. The University of Kansas, Lawrence, KS, 2019.
27.   Todorov, R.; Tasseva, J.; Lozanova, V.; Lalova, A.; Iliev, T.; Paneva, A., Ellipsometric Characterization of Thin Films from Multicomponent Chalcogenide Glasses for Application in Modern Optical Devices. *Advances in Condensed Matter Physics* **2013,** *2013*, 308258.
28.   Woollam, J. A. Ellipsometry Tutorial. (accessed March 25).
29.   Ulman, A., Analytical Tools. In *An Introduction to Ultrathin Organic Films From Langmuir-Blodgett to Self-Assembly*, San Diego, CA, 1991; pp 1-83.
30.   Ogieglo, W.; Wormeester, H.; Eichhorn, K.-J.; Wessling, M.; Benes, N. E., In situ ellipsometry studies on swelling of thin polymer films: A review. *Progress in Polymer Science* **2015,** *42*, 42-78.
31.   Finke, S. J. Infrared Reflection-Absorption Spectroscopy of Thin Film Structures Iowa State University, Iowa, US, 1988.
32.   Golden, W. G.; Saperstein, D. D.; Severson, M. W.; Overend, J., Infrared reflection-absorption spectroscopy of surface species: a comparison of Fourier transform and dispersion methods. *The Journal of Physical Chemistry* **1984,** *88* (3), 574-580.
33.   Darensbourg, M. Y., Ion Pairing Effects on Transition Metal Carbonyl Anions. *Progress in Inorganic Chemistry* **1985**, 221-274.

CHAPTER II

II. Azulene as a Component in Molecular Electronic Materials: Reactivity, Electrochemical Behavior, and Self-Assembly

II.1   Introduction

Azulene, $C_{10}H_8$, a bicyclic non-benzenoid aromatic hydrocarbon and isomer of naphthalene, has been applied to numerous fields including molecular and opto- electronics, sensing, medicine, and even cosmetics.[1, 2] Azulene has peculiar properties arising from electron delocalization which creates an electron-rich five-membered ring and an electron-deficient seven-membered ring as seen in the resonance forms depicted in Figure **2.1**.[1] With this resonance delocalization, azulene gains aromatic stabilization producing an intrinsic dipole moment of 1.08 D aligned along the molecular axis.[3]
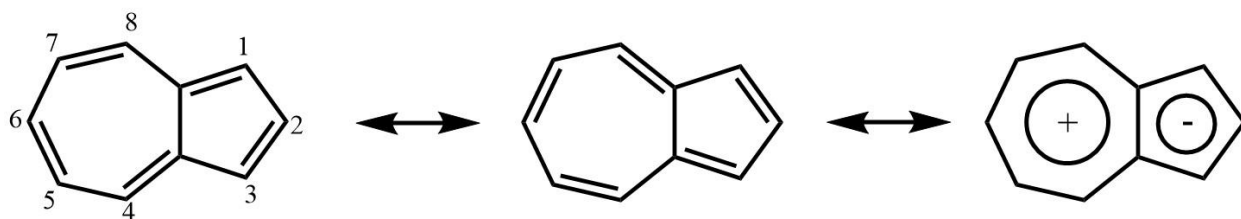
Figure 2.1. Conventional numbering scheme for the azulenic scaffold and its polar resonance structure.

The non-alternant nature of azulene produces non-mirror-related Highest Occupied Molecular Orbital (HOMO) and the Lowest Unoccupied Molecular Orbital (LUMO) where the HOMO density resides mainly on the odd numbered carbons, and the LUMO density is confined to the even numbered carbons. The electron repulsion is reduced upon HOMO-LUMO excitation and this gives rise to a relatively small transition energy between molecular orbitals giving azulene its characteristic deep blue color.[1, 2, 4]
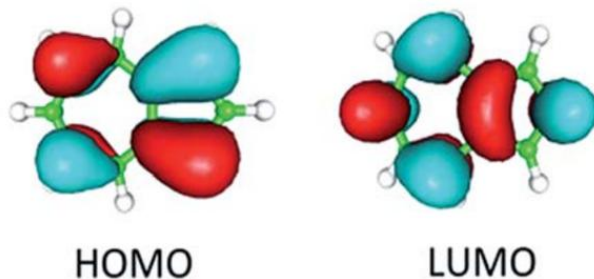
Figure 2.2. Complementary nature of Frontier Molecular Orbitals (FMO) in unsubstituted azulene.[5]

The small energy gap between FMOs and its tunability makes azulene an attractive platform for the development of molecular electronic components, mainly molecular wires, diodes, and rectifiers.[6] The field of molecular electronics has gained momentum in the last 50 years out of the necessity to fabricate smaller electronic devices as we reach a limit on silicon-based technology.[7] This chapter will provide background on silicon-based electronics and their molecular counterpart, as well as a discussion on the reactivity, electrochemical behavior, and self-assembly of azulene based derivatives in the context of molecular electronics applications.

II.2   Reactivity of Azulene

In azulene the reactivity of even-numbered carbon atoms is different to that of the odd-numbered carbon atoms due to the complementary nature of the FMOs. The 1, 3, 5, and 7 positions are electron rich, thus can readily react with electrophilic reagents. On the other hand, the 2, 4, 6, and 8 positions are electron deficient and prefer to react with nucleophilic reagents as seen in figure **2.3**.[1, 2, 8]
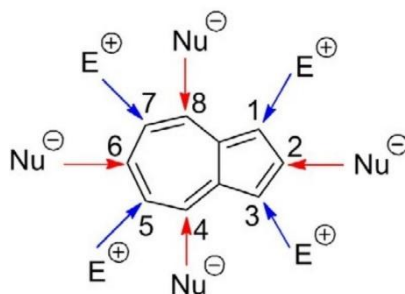
Figure 2.3. Schematic of direct functionalization of azulene.

Based on these principles, it follows that substitution can affect the FMOs independently, tuning the HOMO-LUMO gap depending on the electron withdrawing or donating abilities of the substituents. The FMOs energy gap decreases upon attaching an electron-donating substituent (EDG) to an odd position or an electron withdrawing-substituent (EWG) to an even position. On the contrary, the HOMO-LUMO energy gap increases if an electron-withdrawing group is attached to an odd position of the azulenic scaffold or an electron-donating group is attached to an even-numbered carbon atom. This process is depicted in fig. **2.4** with non-specified EDG and EWG.

20

The tunability of the HOMO-LUMO gap in azulene can be exploited to modulate the semiconductor behavior of these materials.[8]
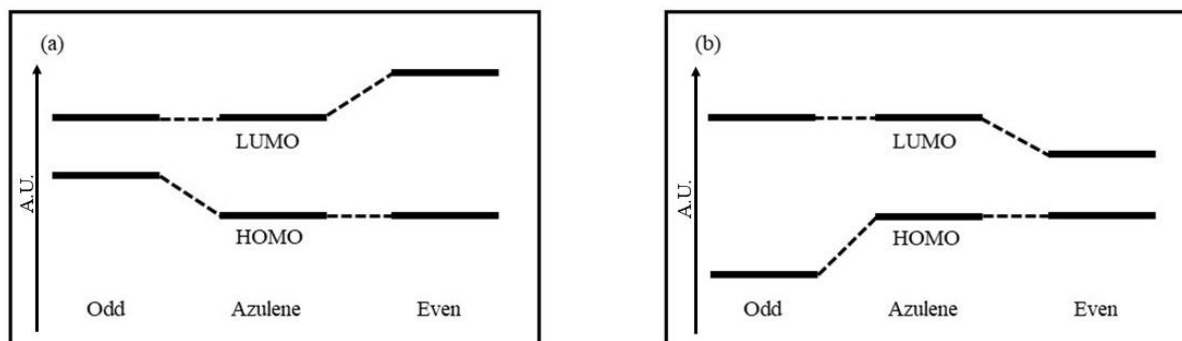
Figure 2.4. The change in HOMO and LUMO energies upon addition of substituents to azulene. (a) Addition of (EDG) to the odd-numbered and even-numbered carbon atoms in azulene. (b) Addition of (EWG) to odd-numbered and even-numbered carbon atoms in azulene.

Azulene undergoes electrophilic substitution at the 1- and 3- positions exclusively as they are the most reactive.[2] Many examples of reactions targeting the 1- and 3- positions exist in the literature, which include polymers,[9] sulfonium salts,[2] halide substitution,[4] among others. However, the electrophilic selectivity towards the 1-, and 3- positions of azulene can be a challenging problem to circumvent if the target for substitution is any other of the odd-numbered positions. Moreover, this thesis applies substitutions along the molecular axis and reactions with the 1- and 3- positions are not desired. The simplest strategy to avoid reactions with these highly reactive positions is to install protecting groups. This thesis employs ethoxycabonyl groups attached to the 1- and 3- positions to provide reliable manipulations along the azulenic scaffold's molecular axis and to increase solubility. The 5- and 7- positions are much less reactive in comparison with the 1- and 3- positions. To ensure proper substitution at the 5- or 7- positions, the 1- and 3- positions need to be blocked. The reactivity at the 5- and 7- positions is not well-explored, but the Barybin group has recently embarked on exploring such reactivity installing a bromine substituent at the 5-position of the azulenic nucleus.

Nucleophilic addition at the 4- and 8- positions often competes with addition at the 6-position producing a mixture of isomers. However, selective addition can be achieved based on the nature of the nucleophile and the substitution pattern on the azulene skeleton.[10, 11] The 2-

position has lower LUMO orbital density compared to the other even-numbered positions and it is therefore more challenging to access.[2] Nonetheless, 2-substituted azulenes can be accessed directly based on the tropolone derivative used in syntheses similar to scheme **2.1**. An amino group is rather useful as it can be subject to a variety of reactions that would afford new substituent groups.[5, 12-15]

The starting material, 2-amino-1,3-diethoxycarbonylazulene, for this thesis was synthesized from cyclopentadiene (CpH). The synthesis involves a retro Diels-Alder reaction with dicyclopentadiene, a [2+2] cycloaddition between CpH and dichloroacetyl chloride, the ring opening of the [2+2] addition product to afford 2-hydroxytropolone, the sulfonation of 2-hydroxytropolone to afford 2-benzenesulfonyltropolone, and, finally, the transformation of 2-benzenesulfonyltropolone into 2-amino-1,3-diethoxycarbonyl azulene (Scheme **1**). By having the 1- and 3- positions in use, manipulations with any other position are possible without unwanted reactions involving the most reactive carbon atoms of the azulenic scaffold.

Scheme 1. Synthesis of the starting azulenic derivative employed in this thesis. (a) Retro Diels-Alder reaction isolated by distillation, (b) dichloroacetyl chloride and triethylamine in pentane, (c) sodium hydroxide in acetic acid, (d) benzene sulfonyl chloride in pyridine, (e) ethyl cyanoacetate and di-isopropylamine in ethanol.[16]
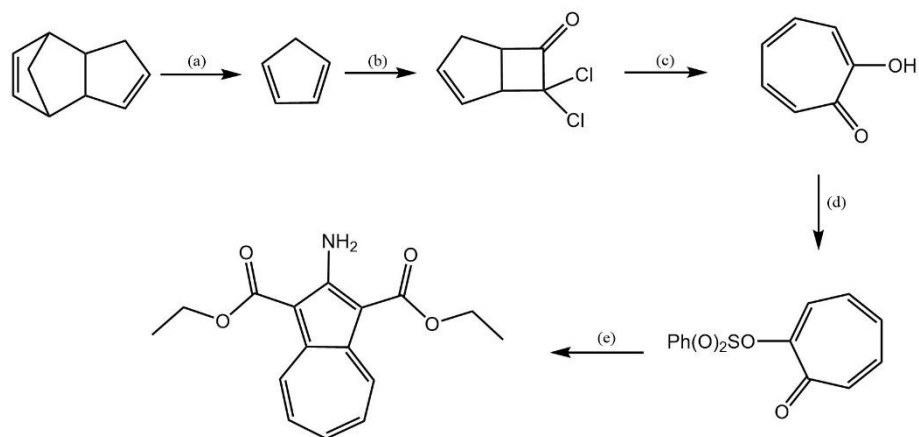
The azulene moiety may undergo coupling reactions with itself, under certain conditions, to produce biazulenes, terazulenes, and other oligomers and polymers.[17] This capability is useful since it allows extended π-functional materials to be created and applied towards other fields such as molecular electronics.

II. 3   Molecular Electronics: Wires, Diodes, and Rectifiers

The interdisciplinary field of molecular electronics has been gaining attention during the last few decades due to the need to fabricate electronic devices in a smaller scale. In the 1980's the average gate length of a silicon-based transistor was about 10 μm, yet in recent reports, that length has shrunken to less than 10 nm.[18] With the progress in miniaturization of electronic devices, it has become extremely challenging to develop methods to take that miniaturization even further in silicon-based electronics. Molecules offer an attractive platform to design and develop single-molecule or bulk electronic devices that are capable of performing the same tasks as their silicon-based counterparts.[18-20]

Perhaps the most common electronic component is a wire. Wires are usually made from conductive metals or alloys with large thermal stability and low resistivity and are usually protected with insulating materials. The main function of a wire is to conduct electricity (flow of electrons) from one electronic device to another. By this definition, contacts in a circuit that allow for the uninterrupted flow of electricity are also classified as wires. It follows that molecular wires must be capable of linking two or more molecular electronic components together and allowing the uninterrupted flow of electrons.[21] Molecular wires have several components which include two or more junction groups, where the wire will be attached to other components, and a bridge, which should be a conjugated system where electrons can flow with minimal resistance.[19] The most common molecular wires to date are made of oligomers of thiophenes, phenylene vinylene, and phenylene ethynylene derivatives. Figure **2.5** shows an oligofluorene molecular wire attached to electrodes using methylsulfide junction groups.[7]
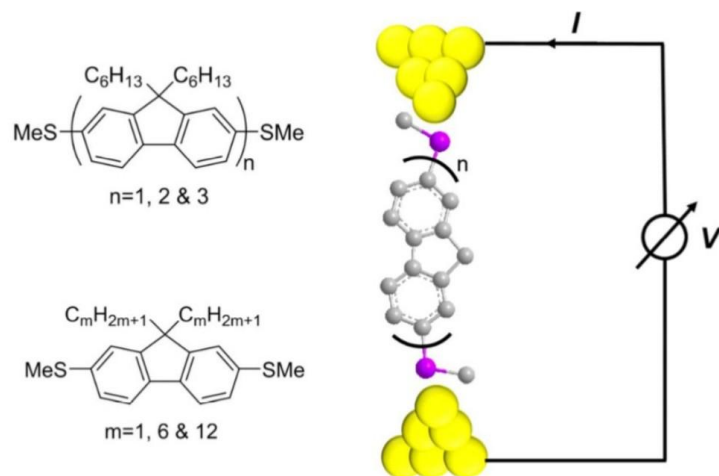
Figure 2.5. Oligofluorenes functioning as molecular wires between two electrodes (Adapted with permission from Sagan *et al*. © 2017 American Chemical Society).[21]

Diodes are also a crucial part of any electronic circuit. Their main function is to achieve a unidirectional flow of electrons based on the bias direction. A silicon-based diode usually consists of three components, a positive p-type semiconductor at the cathode where there is a large number of holes due to doping, a negative n-type semiconductor at the anode where doping creates a large number of free electrons, and the interface where the n- and p- regions meet called the depletion zone (Figure **2.6**). In the depletion zone, some electrons in the n- region migrate to the p- region occupying some holes and creating partial negative charge in the p- region and partial positive in the n- region.[22] This creates a potential barrier between both interfaces for electron flow. Forward bias refers to when electrons flow from the n- regime to the p- regime and can be achieved by connecting the negative end of the power source to the anode. This will create repulsion between electrons and the negative terminal, which will push electrons to fill holes, attracted by the positive terminal, which creates current. If the power source is inverted, the opposite electrical charges would attract, increasing the size of the depletion zone and rendering no current.[22]
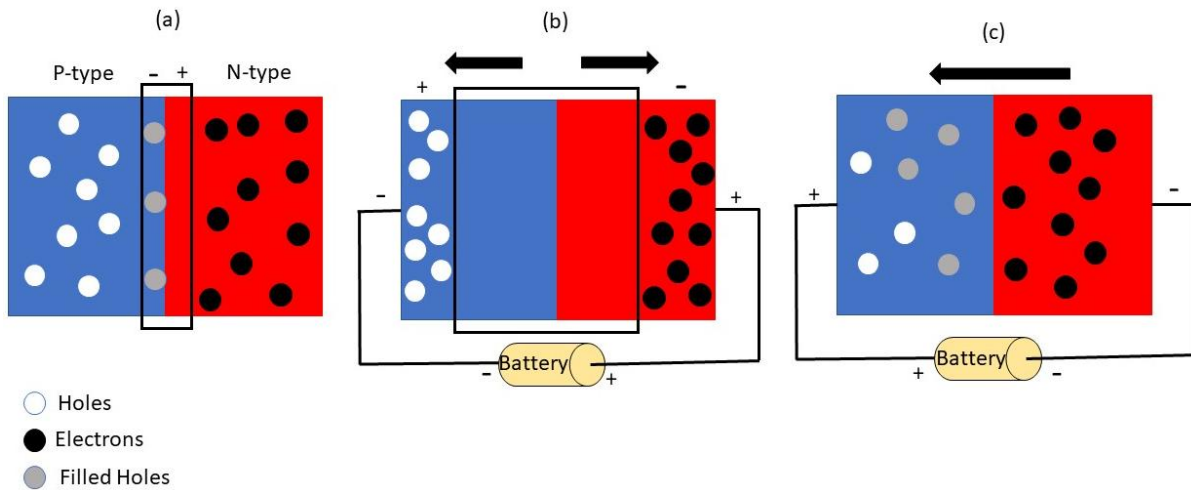
Figure 2.6. Representative diode behavior. (a) no bias applied, electrostatic repulsion from partial charges creates depletion zone, (b) reverse bias where electrons are attracted to positive terminal, (c) forward bias where electrons move toward the holes and positive terminal creating current.

A rectifier is a type of diode system that converts alternating current to direct current. Alternating current (AC) periodically switches direction and direct current (DC) only flows in one direction. A single diode acts as a half-wave rectifier as only a forward bias will produce a current (Figure **2.7**). A full-wave rectifier is capable of converting both, reverse and forward bias into DC. These devices find their usefulness mainly in power supplies, which is the backbone of electronic usage.[22] Figure **2.7** shows what happens to alternating current in half-wave and full-wave rectifiers. Only the forward bias will be visible as the output signal for a single diode in contrast to a full-wave rectifier which produces oscillating direct current by correcting the reverse bias. It is worth noting that capacitors are needed to compensate for the oscillating nature of the rectified signal.[23]
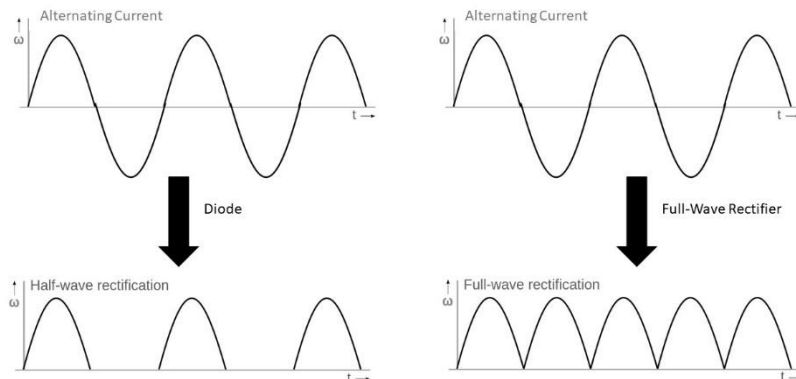
Figure 2.7. Extent of rectification of half- and full-wave rectifiers as output voltage.

The molecular electronics picture is inspired by silicon-based devices but uses different principles. In 1974, Aviram *et al.* first proposed molecular rectifiers and suggested a model based on donor and acceptor substituents.[24] Taking inspiration from the p-n diodes molecular rectifiers are comprised of three sections: an electron-rich fragment (donor), an electron-deficient fragment (acceptor), and a decoupling bridge that serves the same purpose as the depletion zone in silicon-based diodes. The rectification mechanism of these donor-acceptor rectifiers is depicted in figure **2.8**. When attached to electrode, these devices exhibit unidirectional current flow based on the formation of a zwitter-ionic species (D^+A^-) which collapses back to its neutral state (D^0A^0), where the energies of the FMOs of the donor and acceptors are shown relative to the Fermi level energies of the electrodes in arbitrary units.
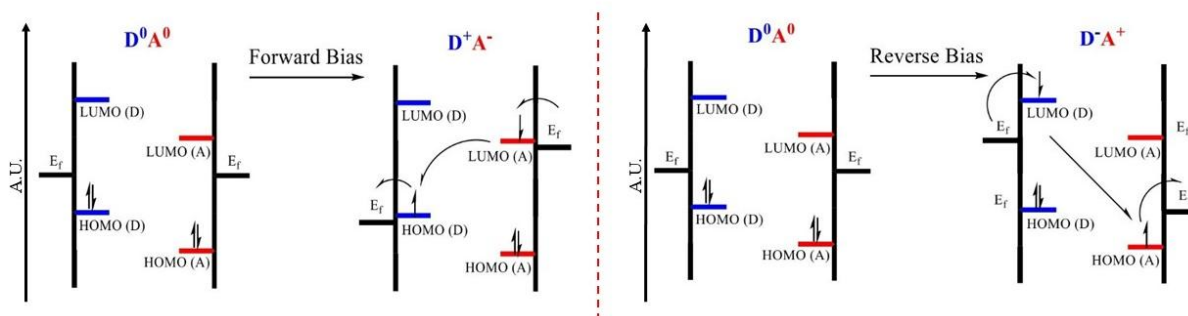
Figure 2.8. Depiction of original donor-acceptor theory of electron flow. Left: favorable forward bias. Right: unfavorable reverse bias due to relatively large energy separation of E_f to LUMO (D).[25] Adapted with permission from Ratner *et al.* © 2015 American Chemical Society.

The original theory of electron flow shows a preference for flow from acceptor to donor. Yet, recent studies by Van Dyck and Ratner suggest an electron flow from donor to acceptor in a new model.[25] In this model Fermi level pinning contributes to a smaller energy gap separating the HOMO-LUMO of the donor and acceptor respectively. The pinning effect comes from the ability of each fragment to align its orbital energy with that of the metal electrodes. Figure **2.9** shows the effect of Fermi level pinning and the further reduction of the energy gap upon application of a bias potential, where the energies of the FMOs of the donor and acceptor are shown relative to the Fermi level energies of the electrodes in arbitrary units.
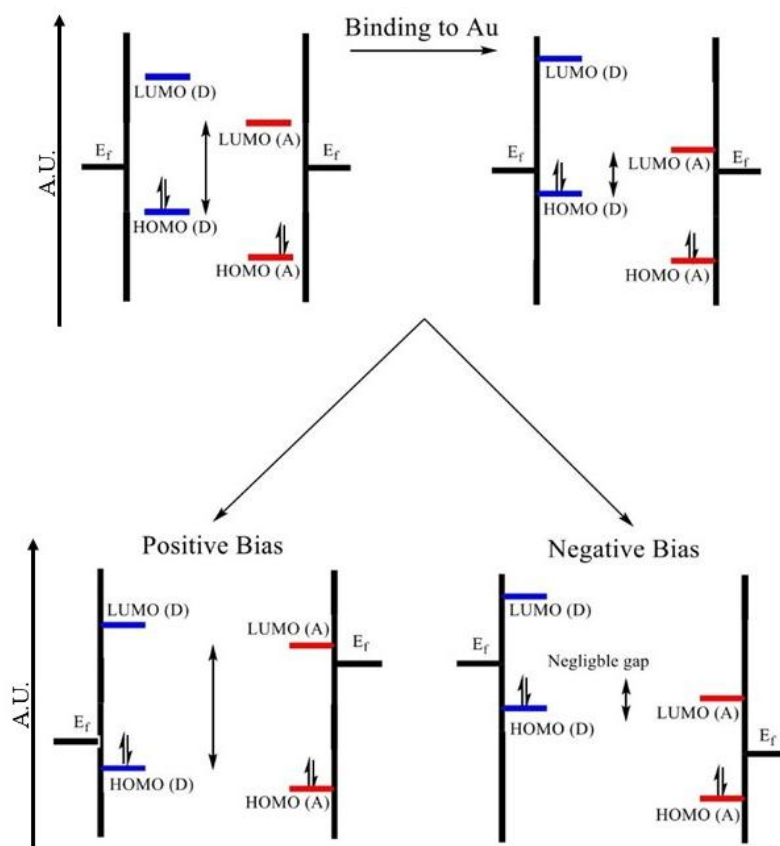
Figure 2.9. Top: Effect of coordination to gold on energy gap. Bottom left: Unfavorable electron flow from acceptor to donor due to the large energy gap between HOMO (D) and LUMO (A). Bottom right: Favorable electron flow from donor to acceptor due to negligible HOMO (D) LUMO (A) energy gap.[25] Adapted with permission from Ratner *et al.* © 2015 American Chemical Society.

The theoretical example given by Van Dyck and Ratner consists of the same three components as mentioned previously. This time they proposed having a mercapto (-SH) donor group and a cyano (-CN) acceptor group connected by conjugated fragments and decoupled by a saturated hydrocarbon (Figure **2.10**). Although promising, this model is synthetically impossible to achieve, the lack of rigidity is non-ideal, and the saturated hydrocarbon bridge would hinder conductivity.[26]
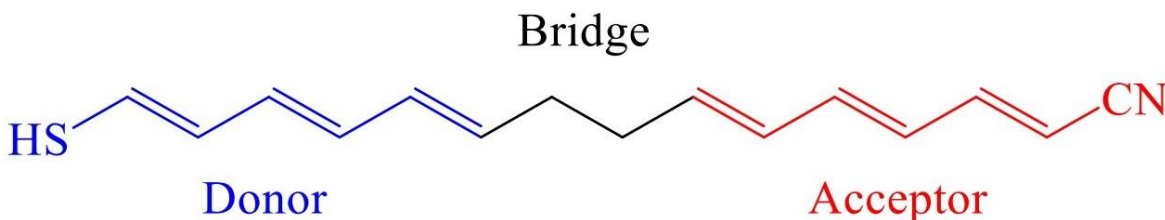
Figure 2.10. Rectifier structure proposed by Van Dyck and Ratner.[25]

II.4   Azulene as a Component in Molecular Electronics

Azulene has gathered some interest from the scientific community as a potential backbone for molecular electronics.[3-5, 13, 27] Azulene exhibits good diode-like behavior due to the intrinsic dipole moment, and this behavior can be amplified based on substitution. Indeed, azulene exhibits good conductivity relative to its isomer, naphthalene, which can be rationalized by stabilization of aromaticity through charge transfer, making azulene an effective molecular wire.[28]

An effective molecular wire needs to have good communication between each termini, but the extent of communication is sometimes hindered by distance.[18] Azulenes substituted with both, mercapto and cyano junctions are known to display good electron transfer properties through a backbone of almost 1 nm[29] which raises questions of communication in a larger π-extended system. Symmetrically substituted molecular linkers have been commonly used to probe conductivity, rectification, and electronic properties through the linker. As a matter of fact, the Barybin group has developed π-extended molecular linkers employing the 6,6′-biazulenic motif as the bridge. The symmetric 2,2′-diisocyano-1,1′,3,3′-tetraethoxycarbonyl-6,6′-biazulene (DIBA, Figure **2.11**) has been used as a quasi-molecular rectifier, and as components in micro-supercapacitors.[30, 31] These

linkers are almost 2 nm long and can be attached to Au(111) surfaces through the isocyanide junctions.
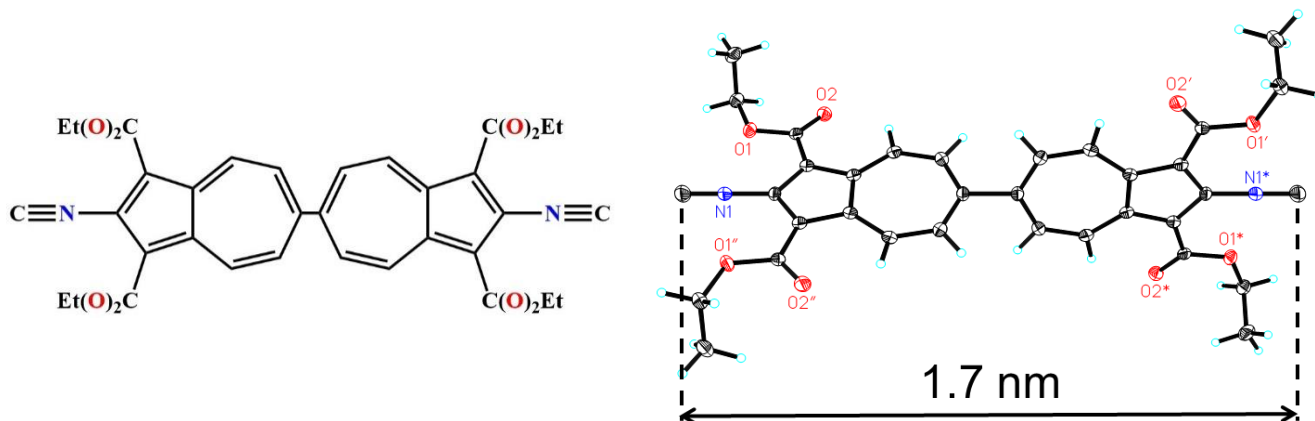
Figure 2.11. Symmetrically substituted 6,6′-biazulenic linker and its X-ray crystal structure (50% thermal ellipsoids).[13]

Electrochemistry can be used to probe the extent of communication between the two isocyanide termini of the 6,6′-biazulenic linker. DIBA undergoes a reversible single-wave 2e$^-$ reduction as opposed to its monomeric counterpart, 2-isocyano-1,3-diethoxycarbonylazulene, which undergoes an irreversible 1e$^-$ reduction (Figure **2.12** and **2.13**). The electrochemical behavior of 2-isocyano-1,3-diethoxycarbonylazulene is irreversible due to decomposition by radical polymerization.
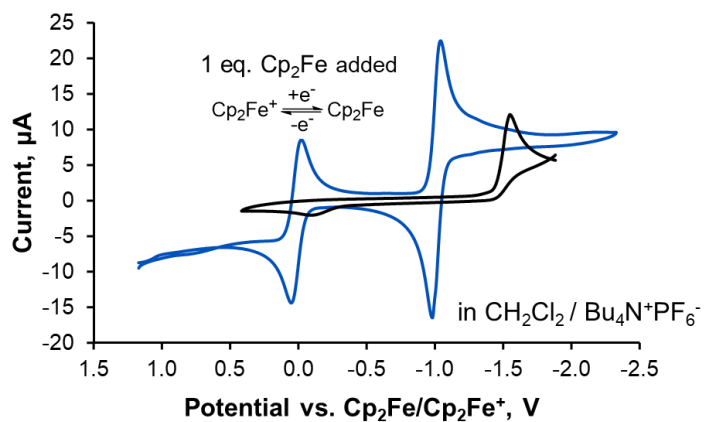
Figure 2.12. Cyclic voltammetry (CV) trace of DIBA (blue) 2-isocyano-1,3-diethoxycarbonylazulene (black) in dichloromethane solution referenced against ferrocene/ferrocenium with tetrabutylammonium hexafluorophosphate (TBA$^+$PF$_6^-$) as supporting electrolyte.[13] Adapted with permission of Maher, Spaeth, Neal *et al.* © 2015 American Chemical Society.

The 6,6′-biazulenic molecular linker undergoes a 2e⁻ reduction by adopting a decreased interazulenic dihedral angle, which increases conjugation, as the 6,6′-biazulenic scaffold takes the shape of a heptafulvalene fused between two cyclopentadienyl anionic rings. By adapting a more planar shape, the second 1e⁻ reduction becomes as, or even more facile than the first reduction, which leads to potential compression (i.e., when the difference in $E_{1/2}$ values is compressed) or possibly potential inversion (i.e., when the second reduction is more facile than the first and $E_{1/2}$ values invert). Another source of potential inversion could be attributed to stabilization of the singly-reduced biazulenic radical anion through contact-ion pairing interactions with $[^nBu_4N]^+$ cation, making the second reduction as facile as the first.[32, 33] A chemical reductant can be used to further evidence the 2e⁻ reduction process of the 6,6'-biazulenic scaffold. By using decamethylcobaltocene as a chemical reducing agent in a stoichiometric titration of DIBA, the Barybin group was able to evidence the 2e⁻ reduction using UV-Vis spectroscopy, obtaining spectra for the singly and doubly reduced species shown in fig. **2.14**.[6]
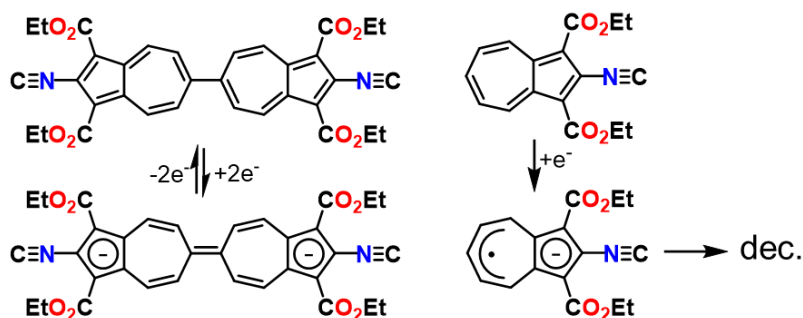
Figure 2.13. Left: predicted reversible 2e⁻ redox behavior of DIBA. Right: predicted decomposition route of monomeric unit.
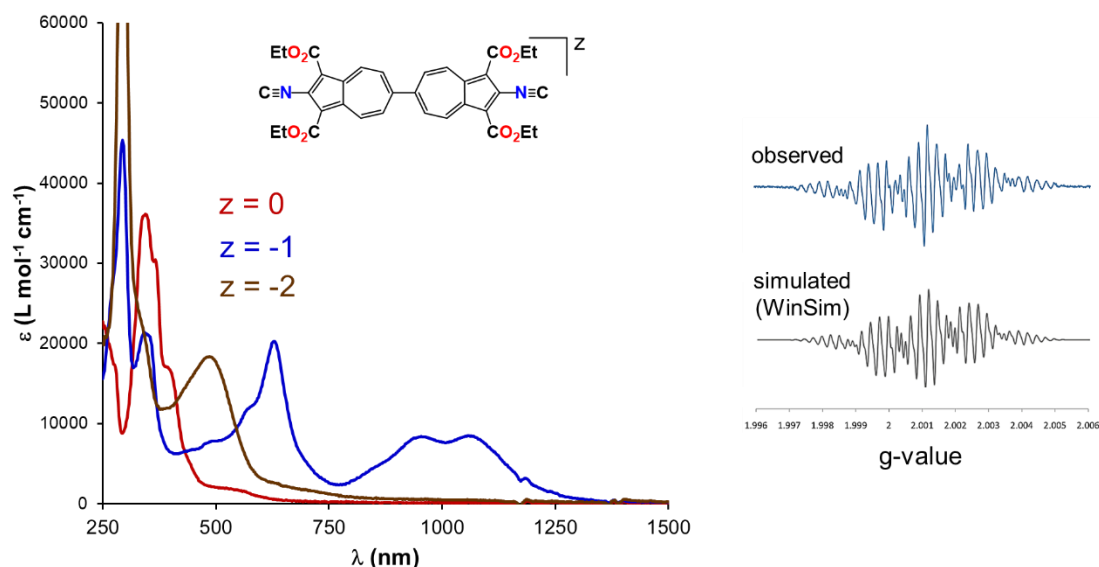
Figure 2.14. Right: UV-Vis spectrum of DIBA as neutral (red), singly reduced (blue), and doubly reduced (brown) using decamethylcobaltocene as reducing agent. Left: EPR of singly reduced DIBA in CH_2Cl_2 at -70°C (Adapted from J.C. Applegate's doctoral dissertation).[6]

The communication between the termini of the asymmetrically substituted 6,6′-biazulenic framework was further analyzed by varying the substituents at the 2 and 2′ positions (Figure **2.15** (a)). The 2 and 2′ substituents were altered to include isocyano, protected thiol, and amino groups symmetrically substituted along the molecular axis of the biazulenic scaffold. Indeed, a shift of the single 2e⁻ reduction wave was observed based on the electronic nature of the substituents without splitting into two 1e⁻ reduction waves. This suggests effective communication between termini but could also be attributed to the symmetric nature of the molecules. The true extent of communication can be analyzed by introducing asymmetry to the linker.

One could imagine a case where asymmetrical substitution is introduced into the 6,6′-biazulenic linker at the 2 and 2′ positions. In the event that there is no communication between the termini, two 1e⁻ reduction waves would be observed in the CV trace at different $E_{1/2}$ values due to the incoming electrons not being delocalized through the entire biazulenic scaffold. Conversely, in the event that there is electronic coupling between the asymmetrically substituted termini, only a single 2e⁻ reduction wave would be observed, and the wave would move as a single reduction

peak while the substituents are varied. That is exactly what was observed in a series of CV traces where the substituent at the 2-position was held constant as a $[Cr(CO)_5]$ unit attached by an isocyano junction to the biazulenic framework. The substituent at the 2′ termini was varied to include a range of electron donating and withdrawing substituents as shown on figure **II.4.5**. This unambiguously shows efficient communication between both azulenic units as the electrons are placed in molecular orbitals spanning the entire biazulenic framework.
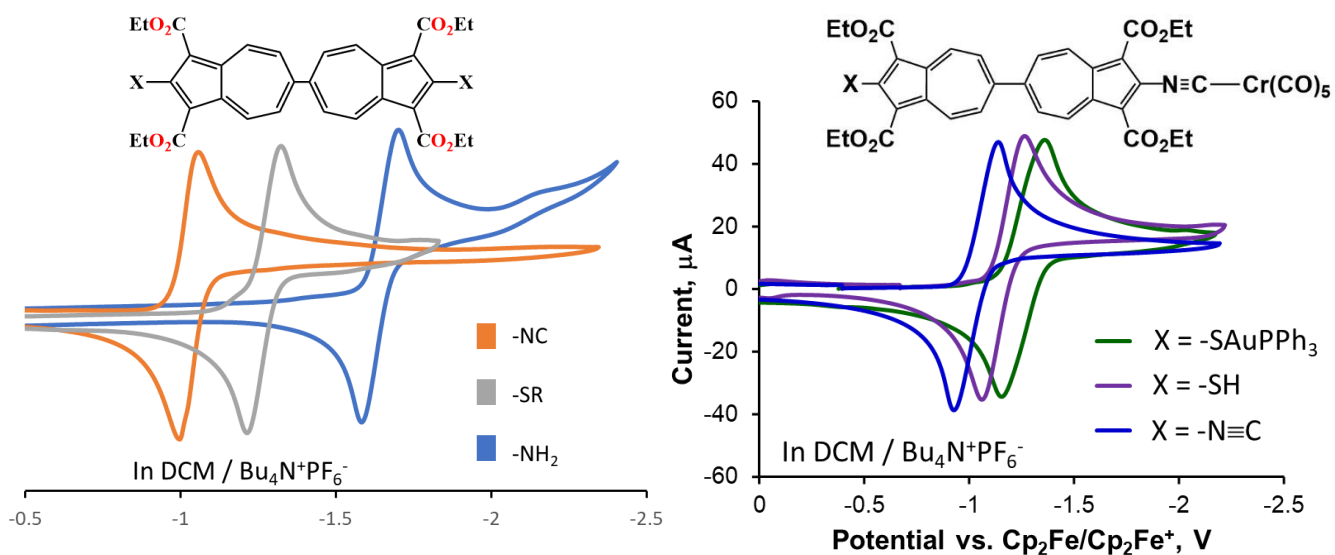
Figure 2.15. (a) CV traces of symmetrically substituted 6,6'-biazulene linker and (b) CV traces of asymmetrically substituted 6,6′-biazulene linker (adapted from J.C. Applegate's doctotral dissertation).[6] Both in dichloromethane solution, referenced against ferrocene, and TBA^+ as the supporting electrolyte.

II.5   Self-Assembly of 6,6′-Biazulene Derivatives on Au (111)

The first example of a 6,6′-biazulenic linker was achieved by the Barybin and Berrie groups in 2010[13], where they succeeded in showing self-assembly of DIBA on Au (111). They used RAIR and isocyano substituents as spectroscopic reporters as proof of coordination to the metal surface and corroborated SAM thickness using ellipsometry. The results were promising as RAIR showed two peaks, one at higher energy, $\nu_{NC}=2170$ cm^{-1}, corresponding to the isocyanide bound to the surface, and a second peak at lower energies, $\nu_{NC}=2119$ cm^{-1}, corresponding to the free isocyanide.

Ellipsometric and theoretically calculated thicknesses were also consistent suggesting an upright orientation of DIBA with respect to the metal surface.
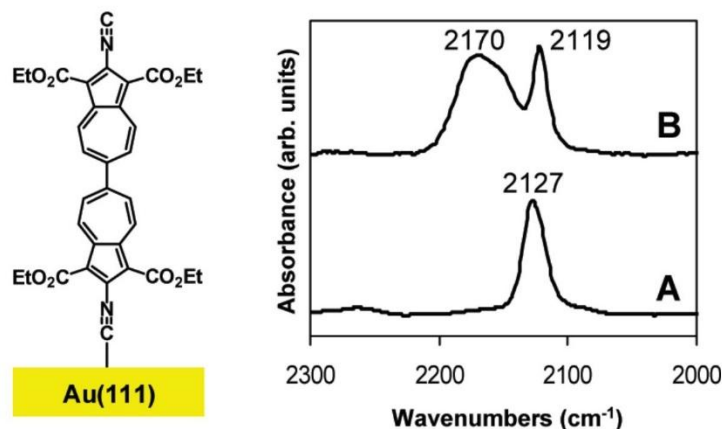
Figure 2.16. Left: Representation of upright orientation of DIBA on Au (111). Right: (A) Solution spectrum of DIBA in CH_2Cl_2 (B) Reflection Absorption Infrared spectrum of DIBA bound to Au (111).[13] Adapted with permission of Maher, Spaeth, Neal; *et al.* © 2015 American Chemical Society.

Asymmetrically substituted 6,6'-biazulenes have also found usefulness in surface chemistry employing thiolate junctions. Thiolate junctions are generally stronger and more favorable than isocyanide junction as the hollow-linear nature of the junction forms strong charge transfer between the sulfur and gold surface.[34] However, characterization of SAMs containing a thiolate junction is challenging due to the lack of spectroscopic markers attainable with RAIR techniques. Nonetheless, spectroscopic reporters can be added to give spectroscopic evidence of SAM behavior. An excellent spectroscopic reporter used for this purpose is the $[(NC)Cr(CO)_5]$ as the stretching frequencies for the CO ligands are intense are readily recognizable. This spectroscopic reporter can provide information on SAM packing and orientation, as well as provide some information about the extent of communication between the thiolate junction and the chromium terminated linker. The 6,6'-biazulenic linker synthesized by Jason Applegate consists of a symmetrical biazulene bridge with a mercapto junction group and capped with an isocyano chromium pentacarbonyl unit as shown in figure **2.17**.

33
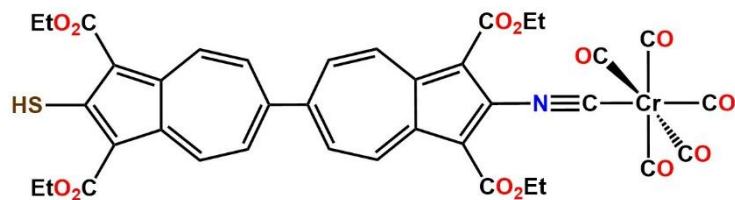
Figure 2.17. Asymmetrically substituted 2-isocyanochromiumpentacarbonyl-1,1',3,3'-tetraethoxycarbonyl-2'-mercapto-6,6'-biazulene (IMBA) molecular linker.

Self-assembly of this IMBA linker onto a Au(111) surface affords monolayers more than 2 nm long chemisorbed onto the surface by a thiolate junction. While comparing solution vs. surface IR (fig. **2.18**), there are several key differences that provide information on packing and orientation of the monolayer film. In the solution IR spectrum, the expected signals are a coordinated isocyanide stretch v_{NC}= 2138 cm^{-1}, and three carbonyl signals including a doubly degenerate E band $v_{cis\text{-}CO}$=1960 cm^{-1}, and $A_1^{(1)}$ $v_{trans\text{-}CO}$=2046 cm^{-1} and an $A_1^{(2)}$ band $v_{trans\text{-}CO}$=1960 cm^{-1} originating from in-phase and out-of-phase stretches of the *trans*-CO with respect to the *cis*-CO. There are several key differences between solution and surface IR spectra upon coordination to the metal substrate, mainly, there is a suppression of the E band and a blue shift of the $A_1^{(1)}$ and $A_1^{(2)}$ bands. The E band suppression comes as a consequence of IR selection rules discussed in the previous chapter. Only dipoles perpendicular to the surface will absorb IR radiation, but it is worth noting that the E band does not completely disappear as a shoulder can still be seen. This suppression suggests that the IMBA molecule adopts a nearly upright orientation with respect to the gold surface. Further supporting this conclusion is excellent agreement between ellipsometric and theoretically calculated thicknesses of 23.8 ± 2.7 Å and 23.7 Å respectively. The blue shifts of the $A_1^{(1)}$ and $A_1^{(2)}$ bands correspond to the chemisorption of the thiolate junction onto the gold as it adapts a hollow-linear coordination.[34] In essence, the gold surface acts as an electron withdrawing group, increasing the π-acidity of the isocyanide ligand, therefore decreasing the electron richness of the [Cr(CO)$_5$] unit and triggering the observed blue shift.[13]

Although SAM formation is effective and organized there is still a residual E signal that indicates some disorder in the thin film. A way to form better organized monolayers is through a SAM displacement approach where SAMs with isocyanide junction are exposed to a thiol-containing molecular linker. RAIR monitoring suggests that the original isocyanide monolayer film is effectively replaced by the thiol-containing molecules forming a more uniform monolayer. Evidence of displacement is evident by considering the bound isocyanide stretch at v_{NC}=2175 cm$^-$

[1] on the left spectrum of figure **2.19**. Once the film is treated with the thiol-containing linker, the surface-bound isocyanide stretch is eliminated as seen on the right spectrum of the aforementioned figure. Also, the $A_1^{(2)}$ band appears to be sharper compared to the RAIR spectrum for the thiolate monolayer depicted in figure **2.18** suggesting a more efficiently packed monolayer.
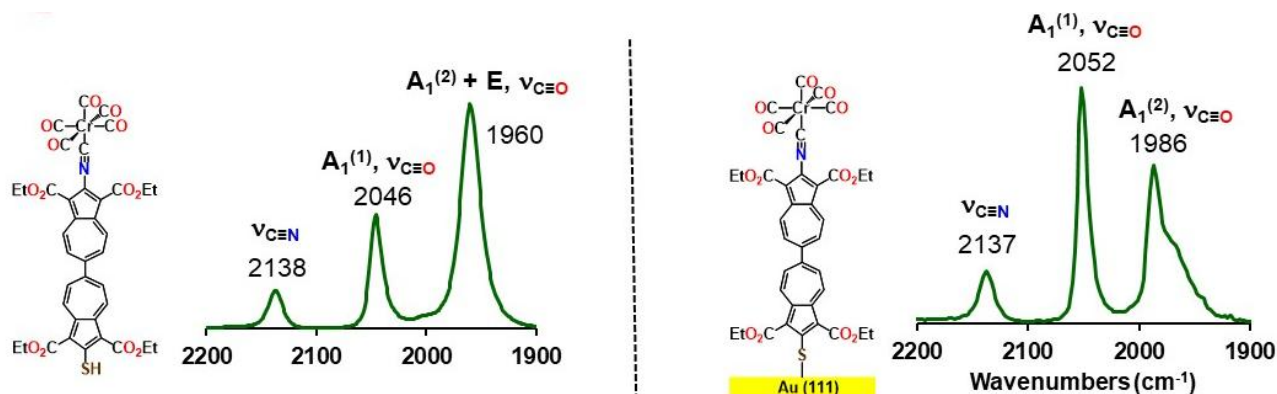
Figure 2.18. Left: Solution FTIR spectrum of IMBA in dichloromethane. Right: SAM of IMBA on Au(111).
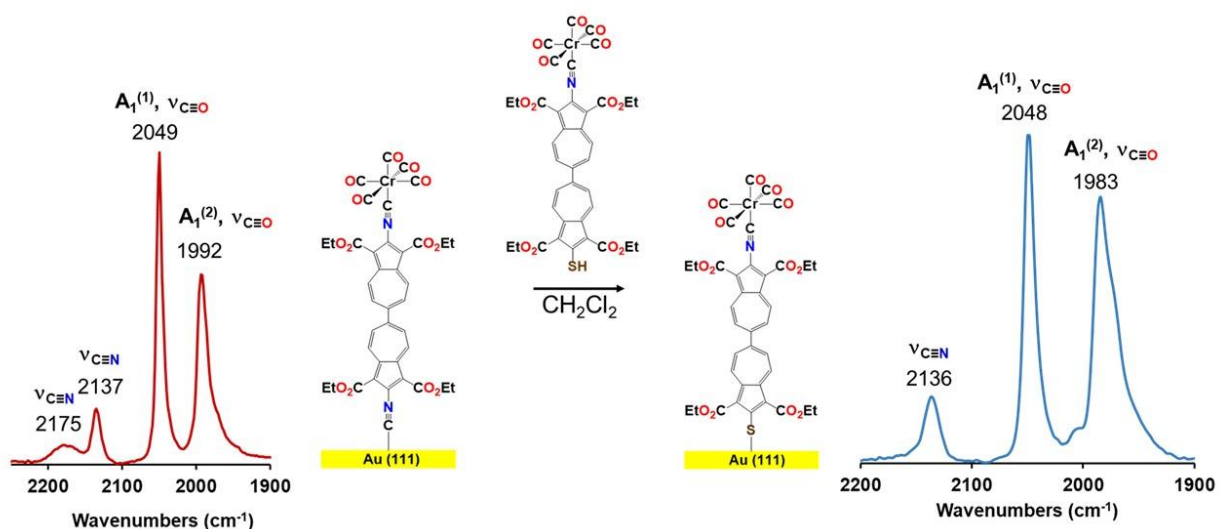
Figure 2.19. Displacement route showing RAIR spectra of before and after treatment with the thiol-containing molecular linker.

II.6   Conclusions and Outlook

Biazulenic linkers have proven to be useful in a variety of fields, especially in molecular electronics applications. Electrochemical evidence suggests electronic coupling through the entire backbone of symmetrically and asymmetrically substituted 6,6′-biazulene molecular linkers making them prime candidates for molecular wire, diode, and rectifier building blocks. The $E_{1/2}$ potential for the 6,6′-biazulenic linkers can be tuned based on the substitution pattern at the 2 and 2′ termini. Coordination of azulenylthiol derivatives to Au(111) surfaces afforded monolayer films featuring nearly upright orientation with respect to the gold surface and RAIR spectroscopy suggested electronic coupling between the thiolate junction and the $[(NC)Cr(CO)_5]$ unit.

The following chapter explores a new molecular linker featuring cyano and mercapto groups incorporated at the 2,2′ positions of the 6,6′-biazulene linker.

II.7   References

1. Gordon, M., The Azulenes. *Chemical Reviews* **1952,** *50* (1), 127-200.
2. Xin, H.; Gao, X., Application of Azulene in Constructing Organic Optoelectronic Materials: New Tricks for an Old Dog. *ChemPlusChem* **2017,** *82* (7), 945-956.
3. Razus, A. C., Azulene Moiety as Electron Reservoir in Positively Charged Systems; A Short Survey. *Symmetry* **2021,** *13* (4).
4. Dong, J.-X.; Zhang, H.-L., Azulene-based organic functional molecules for optoelectronics. *Chinese Chemical Letters* **2016,** *27* (8), 1097-1104.
5. Applegate, J. C.; Okeowo, M. K.; Erickson, N. R.; Neal, B. M.; Berrie, C. L.; Gerasimchuk, N. N.; Barybin, M. V., First π-linker featuring mercapto and isocyano anchoring groups within the same molecule: synthesis, heterobimetallic complexation and self-assembly on Au(111). *Chemical Science* **2016,** *7* (2), 1422-1429.
6. Applegate, J. C. Development of New Electron-rich Organometallic Platforms Featuring Linear Azulenic and 6,6'-Biazulenic pi-Linkers Equipped with Isocyanide and Thiolate Junctions. University of Kansas, Lawrence, KS, 2019.
7. Cuevas, J. C.; Scheer, E., *Molecular Electronics*. WORLD SCIENTIFIC: 2017; Vol. Volume 15, p 848.
8. Xin, H.; Hou, B.; Gao, X., Azulene-Based π-Functional Materials: Design, Synthesis, and Applications. *Accounts of Chemical Research* **2021**.
9. Wang, F.; Lai, Y.-H.; Kocherginsky, N. M.; Kosteski, Y. Y., The First Fully Characterized 1,3-Polyazulene: High Electrical Conductivity Resulting from Cation Radicals and Polycations Generated upon Protonation. *Organic Letters* **2003,** *5* (7), 995-998.
10. Mągoikosza, M.; Kuciak, R.; Wojciechowski, K., Vicarious Nucleophilic Substitution (VNS) of Hydrogen in Azulenes. *Liebigs Annalen der Chemie* **1994,** *1994* (6), 615-618.
11. McDonald, R. N.; Petty, H. E.; Wolfe, N. L.; Paukstelis, J. V., Nonbenzenoid aromatic systems. X. Formation, nuclear magnetic resonance spectral identification, and reactions of both Meisenheimer type and methyleneazulenate anions. *The Journal of Organic Chemistry* **1974,** *39* (13), 1877-1887.
12. DuBose, D. L.; Robinson, R. E.; Holovics, T. C.; Moody, D. R.; Weintrob, E. C.; Berrie, C. L.; Barybin, M. V., Interaction of Mono- and Diisocyanoazulenes with Gold Surfaces: First Examples of Self-Assembled Monolayer Films Involving Azulenic Scaffolds. *Langmuir* **2006,** *22* (10), 4599-4606.
13. Maher, T. R.; Spaeth, A. D.; Neal, B. M.; Berrie, C. L.; Thompson, W. H.; Day, V. W.; Barybin, M. V., Linear 6,6′-Biazulenyl Framework Featuring Isocyanide Termini: Synthesis, Structure, Redox Behavior, Complexation, and Self-Assembly on Au(111). *Journal of the American Chemical Society* **2010,** *132* (45), 15924-15926.
14. Neal, B. M.; Vorushilov, A. S.; DeLaRosa, A. M.; Robinson, R. E.; Berrie, C. L.; Barybin, M. V., Ancillary nitrile substituents as convenient IR spectroscopic reporters for self-assembly of mercapto- and isocyanoazulenes on Au(111). *Chemical Communications* **2011,** *47* (38), 10803-10805.
15. Scheetz, K. J.; Spaeth, A. D.; Vorushilov, A. S.; Powell, D. R.; Day, V. W.; Barybin, M. V., The 2,6-dimercaptoazulene motif: efficient synthesis and completely regioselective metallation of its 6-mercapto terminus. *Chemical Science* **2013,** *4* (11), 4267-4272.
16. Nozoe, T.; Takase, K.; Nakazawa, T.; Fukuda, S., The formation of azulene derivatives from 2H-cyclohepta[b]furan-2-one derivatives. *Tetrahedron* **1971,** *27* (15), 3357-3368.
17. Huang, J.; Huang, S.; Zhao, Y.; Feng, B.; Jiang, K.; Sun, S.; Ke, C.; Kymakis, E.; Zhuang, X., Azulene-Based Molecules, Polymers, and Frameworks for Optoelectronic and Energy Applications. *Small Methods* **2020,** *4* (10), 2000628.
18. Xiang, D.; Wang, X.; Jia, C.; Lee, T.; Guo, X., Molecular-Scale Electronics: From Concept to Function. *Chemical Reviews* **2016,** *116* (7), 4318-4440.
19. Mathew, P. T.; Fang, F., Advances in Molecular Electronics: A Brief Review. *Engineering* **2018,** *4* (6), 760-771.

20.   Vilan, A.; Aswal, D.; Cahen, D., Large-Area, Ensemble Molecular Electronics: Motivation and Challenges. *Chemical Reviews* **2017,** *117* (5), 4248-4286.

21.   Bingrun Chen, K. X., Single Molecule-Based Electronic Devices: A Review. *NANO: Brief Reports and Reviews* **2019,** *14* (11).

22.   Walker, J. S., *Physics*. 4th ed.; Jim Smith: San Francisco, CA 2010.

23.   Ruth W. Chabay, B. A. S., *Matter and Interactions*. 4 ed.; John Wiley and Sons, Inc.: USA, 2015; Vol. 2.

24.   Aviram, A.; Ratner, M. A., Molecular rectifiers. *Chemical Physics Letters* **1974,** *29* (2), 277-283.

25.   Van Dyck, C.; Ratner, M. A., Molecular Rectifiers: A New Design Based on Asymmetric Anchoring Moieties. *Nano Letters* **2015,** *15* (3), 1577-1584.

26.   Watanabe, H.; Kato, H., Thermal Conductivity and Thermal Diffusivity of Twenty-Nine Liquids: Alkenes, Cyclic (Alkanes, Alkenes, Alkadienes, Aromatics), and Deuterated Hydrocarbons. *Journal of Chemical & Engineering Data* **2004,** *49* (4), 809-825.

27.   El-Nahas, A. M.; Staykov, A.; Yoshizawa, K., Electrical Conductance and Diode-Like Behavior of Substituted Azulene. *The Journal of Physical Chemistry C* **2017,** *121* (5), 2504-2511.

28.   Dutta, S.; Lakshmi, S.; Pati, S. K., Comparative study of electron conduction in azulene and naphthalene. *Bulletin of Materials Science* **2008,** *31* (3), 353-358.

29.   Wächter, T.; Scheetz, K. J.; Spaeth, A. D.; Barybin, M. V.; Zharnikov, M., Dynamics of Electron Transfer in Azulene-Based Self-Assembled Monolayers. *The Journal of Physical Chemistry C* **2017,** *121* (25), 13777-13785.

30.   Sun, S.; Zhuang, X.; Wang, L.; Zhang, B.; Ding, J.; Zhang, F.; Chen, Y., Azulene-bridged coordinated framework based quasi-molecular rectifier. *Journal of Materials Chemistry C* **2017,** *5* (9), 2223-2229.

31.   Zhang, P.; Wang, J.; Sheng, W.; Wang, F.; Zhang, J.; Zhu, F.; Zhuang, X.; Jordan, R.; Schmidt, O. G.; Feng, X., Thermoswitchable on-chip microsupercapacitors: one potential self-protection solution for electronic devices. *Energy & Environmental Science* **2018,** *11* (7), 1717-1722.

32.   Bird, M. J.; Iyoda, T.; Bonura, N.; Bakalis, J.; Ledbetter, A. J.; Miller, J. R., Effects of electrolytes on redox potentials through ion pairing. *Journal of Electroanalytical Chemistry* **2017,** *804*, 107-115.

33.   Fry, A. J., Effects of Strong Ion-Pairing on the Electrochemical Reduction of Cyclooctatetraene in Tetrahydrofuran in the Presence of Lithium Ion. Peak Coalescence Does Not Imply Potential Inversion. *Electroanalysis* **2006,** *18* (4), 391-398.

34.   Ulman, A., *An Introduction to Ultrathin Organic Films From Langmuir-Blodgett to Self-Assembly*. Academic Press: San Diego, CA, 1991.

CHAPTER III

III. A Symmetric Biazulenic π-Linker Asymmetrically Terminated with Mercapto and Cyano Anchoring Groups Along its Molecular Axis

III.1 Introduction

Herein we introduce a synthetic approach to access asymmetrically substituted 6,6′-biazulenic π-linkers by employing Pd-catalyzed coupling of two strategically substituted mono-azulenic derivatives. The electronic communication between the two azulenic constituents within this biazulenic linker was assessed electrochemically. Efforts to introduce self-assembly of this π-linker on Au(111) are discussed as well, but there was no observed spectroscopic or ellipsometric evidence of monolayer formation. Several possible reasons for the lack of ordered self-assembly are provided, as well as an overview of experimental modifications to the general self-assembly procedure performed in hopes of attaining monolayer growth.

Organic mercaptans (R-SH) have been known to efficiently and reproducibly bind to metallic gold surfaces, forming a relatively stable gold-thiolate (Au-S) interface between the metal surface and the organic monolayer film.[1] In the case of self-assembly on Au(111) surface, the most energetically favorable binding mode involves "hollow-linear" coordination of the thiolate unit to the hexagonal Au(111) face. The good thermodynamic stability of the Au-S bonds in such self-assembled monolayer films likely arises from the S→Au charge transfer via S(3p)-Au(111) π-backbonding. [1-4] Typically, a π-conducting molecuar linker features identical junction groups (e.g., -SH termini at both ends). If, in addition to conductivity, rectification is desired, the backbone of the π-linker must be decorated with electron-withdrawing and electron-donating substituents at the opposite extremes.[5]

In 2015, Ratner and Van Dyke proposed a new concept for the design of efficient molecular rectifiers which features two π-conjugated fragments asymmetrically anchored to metallic electrodes and connected by a decoupling bridge.[6] Their theoretical study suggested the use of mercapto and cyano junctions as a way to align the linker's HOMO (Highest Occupied Molecular Orbital) and LUMO (Lowest Unoccupied Molecular Orbital), respectively, to the metal electrodes at opposite ends of the molecule through Fermi level pinning.[6] Although intriguing, the proposed model presents major synthetic challenges that need to be overcome. First, the installation of vastly electronically different -SH and -CN junction groups is a significant synthetic challenge. Moreover, the decoupling unit separating the conjugated fragments would decrease conductivity through the molecular backbone and the long aliphatic backbone lacks rigidity. As a first case study to develop a synthetic strategy to build asymmetrically anchoring π-linkers, probe

communication through the π-linker's backbone, and analyze self-assembly of such π-linker on Au(111) surfaces, we sought to design a linear, symmetric biazulenic molecular linker asymmetrically terminated with mercapto and cyano junctions groups along its molecular axis.

III.2   Experimental

III.2.1 General Procedures

Unless otherwise noted, all manipulations were conducted under 99.5% argon atmosphere subjected to flow through columns of activated BAFS catalyst and molecular sieves. The apparatus to purify argon was made of glass, metal, or other materials impermeable to air. For air-free manipulations, standard Schlenk techniques with double manifold vacuum lines were employed. Solvents were transferred using stainless steel cannulas. Dichloromethane was distilled over CaH_2. Dimethyl sulfoxide and dimethyl formamide were dried with $MgSO_4$ and distilled over activated molecular sieves. Pentane was distilled from Na/benzophenone dissolved in a minimum amount of diglyme. Pyridine was kept over KOH and distilled over activated molecular sieves. Methanol and ethanol were distilled over magnesium turnings. All other solvents were used as received from commercial sources.

Solution infrared spectra were collected with a PerkinElmer Spectrum 100 FTIR spectrometer. The solution samples were sealed in 0.1mm NaCl cells and solid samples were made as KBr pellets. Surface infrared spectra was collected in a nitrogen-purged ThermoNicolet Nexus 670 E.S.P. FTIR spectrometer with a VeeMax reflection-absorption accessory. NMR samples were analyzed using either a Bruker Avance III HD 400 MHz or Avance III 500 MHz spectrometers. Hydrogen and carbon NMR chemical shifts were referenced to tetramethylsilane by using residual NMR solvent resonances. UV-Vis spectra were collected at 25°C using a CARY 100 Bio UV-Vis spectrophotometer.

Cyclic voltammetry experiments were conducted under argon atmosphere on 0.02 mM solutions of analytes in distilled CH_2Cl_2 using an EPSILON (Bioanalytical Systems Inc., West Lafayette, IN) electrochemical potentiometer workstation. The supporting electrolyte was 0.1 M $[nBu_4N]^+[PF_4]^-$ solution in dichloromethane. A system consisting of a glassy carbon working electrode, a platinum wire auxiliary electrode, and a glass-encased non-aqueous Ag/AgCl

reference electrode was used. All cyclic voltammograms were recorded at a scan rate of 100mV/s. External and the potential values were referenced to the external Cp_2Fe/Cp_2Fe^+ couple.

Gold samples were purchased from Platypus Technologies and consisted of a silicon wafer coated with a 50 Å titanium adhesion layer and then with 1000 Å of gold. The gold substrates for self-assembled monolayers formation were prepared by cleaning a 1×1 cm gold sample with sequential portions of toluene, chloroform, acetone, and ethanol, followed by drying under a nitrogen stream. The cleaned gold substrates were immersed in either 2.0 mM or 5.0 μM solutions of the desired compound in dichloromethane. Three replicate samples were prepared and characterized for each experiment.

Melting point measurements were obtained for samples sealed in a glass capillary tube using a MEL-TEMP Electrothermal apparatus. Elemental analysis samples were performed by Micro-Analysis, Inc., Wilmington, Delaware. X-ray crystal structural data were collected by Dr. Victor Day of the University of Kansas or Dr. Allen Oliver of the University of Notre Dame. High-resolution mass-spectral data were collected in the mass-spectrometry facility at the University of Kansas.

III.2.2. Synthesis of compound **3.1**
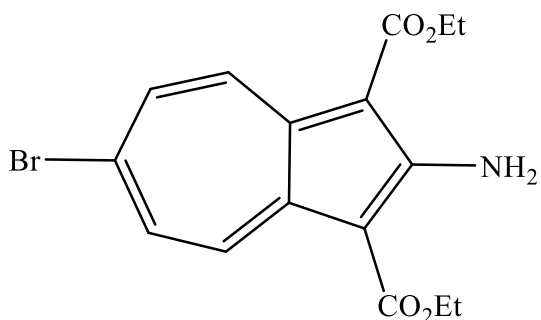
2-Amino-6-bromo-1,3-diethoxycarbonylazulene. 2-amino-1,3-diethoxycarbonylazulene (75.0 g, 261 mmol) was dissolved in 500 mL of $CHCl_3$ in a 1 L round-bottom flask. The solution was left stirring at 5°C for 30 minutes. Bromine (13.4 mL, 261 mmol) was diluted to 150 mL using ice-cold $CHCl_3$ and the resulted solution was loaded into an addition funnel. The Br_2 solution was slowly added over the course of an hour to the reaction flask chilled in an ice bath. Once the addition was complete, the reaction mixture was left to warm to room temperature with stirring. Then the content of the reaction flask was washed with deionized H_2O (3×200 mL). The bright red organic layer was separated, dried over anhydrous Na_2SO_4, and filtered. The filtrate was concentrated under reduced pressure to afford a dark red oil. The oil was taken up in hot benzene to afford a bright yellow crystalline precipitate upon cooling. The solid was filtered off and dried under vacuum (10^{-2} torr) to isolate compound **3.1** (59.0 g, 161 mmol) in a 62% yield. ^{1}H NMR (400 MHz, $CDCl_3$, 25°C): δ 1.48 (t, $^3J_{HH}= 7.13$ Hz, 6H, CH_3), 4.46 (q, $^3J_{HH}= 7.13$ Hz, 4H, CH_2), 7.79 (s, 2H, NH_2), 7.80 (d, 2H, $H^{5,7}$), 8.82 (d, $^3J_{HH}= 11.29$ Hz, 2H, $H^{4,8}$) ppm.

III.2.3. Synthesis of compound **3.2**
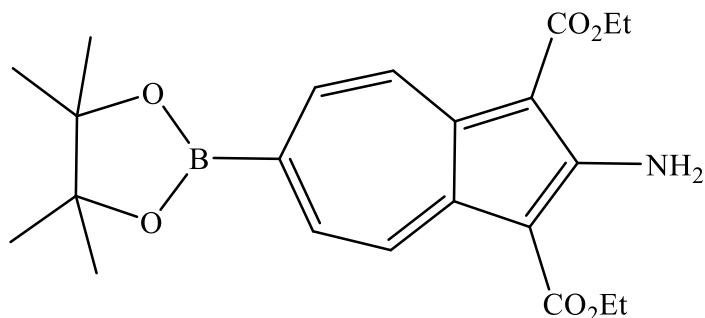
2-Amino-1,3-diethoxycarbonyl- 6-pinacolatoborylazulene. A solid mixture of 2-amino-6-bromo-1,3-diethoxycarbonylazulene (10.0 g, 27.3 mmol), [1,1′-bis(diphenylposphino)ferrocene]dichloropalladium(II) (0.669 g, 0.819 mmol), bis(pinacolato)diboron (7.63 g, 30.0 mmol), and potassium acetate (8.04 g, 81.9 mmol) was dissolved in 150 mL of dimethylsulfoxide (distilled over CaH_2). The resulting mixture was heated at 90°C. After 3 hours, the temperature was reduced to 50 °C and the reaction was left to stir overnight. The reaction was quenched with deionized H_2O (300 mL) and extracted with a 1:1 mixture of toluene/ethyl acetate. The organic layer was dried over anhydrous Na_2SO_4, filtered, and the solvent was removed under reduced pressure to afford a dark yellow oil. This oil was subjected to column chromatography (silica gel, 12 cm) using neat dichloromethane as eluent. The first (orange) fraction was collected. Slow evaporation of the solvent afforded an orange powder which was recrystallized from hot methanol to produce flaky orange crystals of **3.2** (9.08 g, 22.0 mmol) in an 80% yield. ^{1}H NMR (400 MHz, $CDCl_3$, 25°C): δ 1.38 (s, 12H, CH_3), 1.47 (t, $^3J_{HH}$= 7.13 Hz, 6H, CH_3), 4.45 (q, $^3J_{HH}$= 7.13 Hz, 4H, CH_2), 7.93 (s, 2H, NH_2), 8.04 (d, $^3J_{HH}$= 10.98 Hz, 2H, $H^{5,7}$), 9.08 (d, $^3J_{HH}$= 10.98 Hz, 2H, $H^{4,8}$) ppm

III.2.4. Synthesis of compound **3.3**
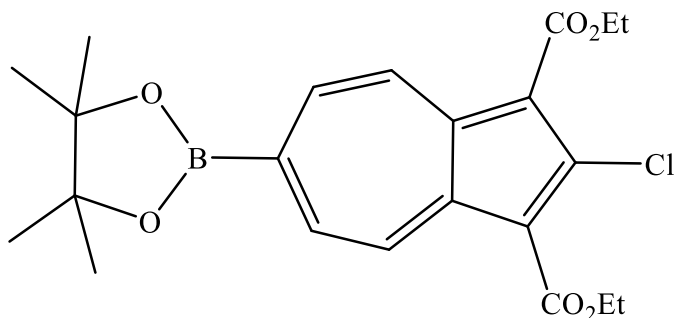
2-Chloro-1,3-diethoxycarbonyl-6-pinacolatoborylazulene. A solution of 2-amino-1,3-diethoxycarbonyl-6-pinacolatoborylazulene (5.00 g, 12.0 mmol) in 150 mL of toluene was cooled to 5°C. Upon cooling, dry HCl, generated by slowly dropping concentrated H_2SO_4 over NaCl, was bubbled through the above solution for 2 hours. The resulting HCl saturated solution was treated with isoamyl nitrite (3.32 mL, 24.2 mmol) dropwise. The reaction mixture was warmed to room temperature and left to stir for 15 hours. During this time, color changes from orange, to forest green, and finally to purple were observed. Subsequently, the mixture was quenched with 150 mL of deionized H_2O. The organic phase was washed with saturated aqueous $NaHCO_3$ (2×150 mL) and dried over anhydrous Na_2SO_4. The solvent was removed under reduced pressure to afford a purple paste. The paste was subjected to column chromatography (silica gel, 10 cm) with a 5:1 hexane/ethyl acetate mixture as eluent. The first (purple) band was collected, and the solvent was slowly evaporated to afford purple needle-shaped crystals of **3.3** (4.82 g, 11.2 mmol) in a 92% yield. Mp: 135-137°C. ^{1}H NMR (400 MHz, CDCl₃, 25°C): δ 1.40 (s, 12H, CH₃), 1.47 (t, $^3J_{HH}$= 7.13 Hz, 6H, CH₃), 4.46 (q, $^3J_{HH}$= 7.13 Hz, 4H, CH₂), 8.23 (d, $^3J_{HH}$= 10.68 Hz, 2H, H^{5,7}), 9.48 (d, $^3J_{HH}$= 10.68 Hz, 2H, H^{4,8}) ppm.

III.2.5. Synthesis of compound **3.4**

R= -CH₂CH₂C(O)OCH₂CH₃
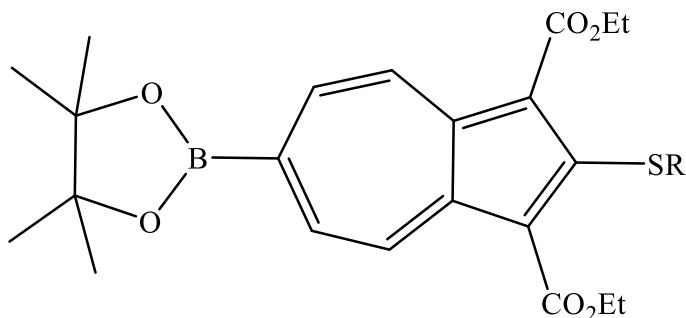
1,3-Diethoxycarbonyl-2-(ethyl-3-mercaptopropionyl)-6-pinacolatoborylazulene. 2-Chloro-1,3-diethoxycarbonyl-6-pinacolatoborylazulene (8.00 g, 18.49 mmol) was dissolved in 75 mL of pyridine. Ethyl-3-mercaptopropionate (3.00 mL, 28.0 mmol) was added slowly to the solution. The mixture was refluxed at 115°C for 4 hours and then left to stir overnight at room temperature. The pyridine solvent was removed under vacuum and the residue was dissolved in 100 mL of dichloromethane. The solution was washed with deionized water (3×150 mL), and dried under anhydrous Na_2SO_4. The drying agent was filtered off and the filtrate was concentrated under reduced pressure to afford a deep purple oil. The oil was subjected to column chromatography (silica gel, 20 cm) with a 5:1 hexane/ethyl acetate mixture as eluent. The second (red) band was collected, and the solvent was slowly evaporated to afford a dark red oil which was dissolved in 100 mL of boiling pentane and left to cool at 5°C overnight. Deep purple crystals of **3.4** (7.17 g, 13.52 mmol) were collected in a 73.1% yield. Mp: 58-59°C. ^{1}H NMR (400 MHz, CDCl₃, 25°C): δ 1.21 (t, $^3J_{HH}$=7.15 Hz, 3H, CH₃), 1.39 (s, 12H, CH₃), 1.47 (t, $^3J_{HH}$=7.15 Hz, 6H, CH₃), 2.60 (dd, $^3J_{HH}$=(8.06, 7.25) Hz, 2H, CH₂), 3.33 (dd, $^3J_{HH}$=(8.06, 7.25) Hz, 2H, CH₂), 4.10 (q, $^3J_{HH}$=7.15 Hz, 2H, CH₂), 4.49 (q, $^3J_{HH}$=7.15 Hz, 4H, CH₂), 8.11 (d, $^3J_{HH}$=10.72 Hz, 2H, H^{5,7}), 9.11 (d, $^3J_{HH}$=10.72 Hz, 2H, H^{4,8}) ppm.

III.2.6. Synthesis of compound **3.5**
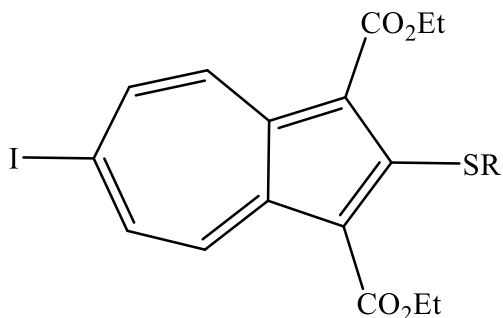
R= -CH$_2$CH$_2$COOCH$_2$CH$_3$

1,3-Diethoxycarbonyl-2-(ethyl-3-mercaptopropionyl)-6-iodoazulene. 1,3-Diethoxycarbonyl-2-(ethyl-3-mercaptopropionyl)-6-pinacolatoborylazulene (0.130 g, 0.250 mmol) was dissolved in a 50 mL suspension of CuI (0.0526 g, 0.280 mmol) and dimethylformamide heated to 90°C for 3 hours. Then the mixture was left stirring at room temperature for 12 hours. The reaction was quenched with deionized water and washed with brine (3×100 mL), extracted with 1:1 toluene/ethyl acetate, and dried over anhydrous MgSO$_4$. The drying agent was filtered off and the filtrate was concentrated to dryness to afford a red oil. The oil was subjected to column chromatography (silica gel, 10 cm) using 5:1 hexane/ethyl acetate mixture as eluent. The first (orange) band was collected, and the solvent was slowly evaporated to afford red needle-like crystals of **3.5** (0.0408 g, 0.0770 mmol) in a 40% yield. Mp: 87-88°C. ^{1}HNMR (400 MHz, CDCl$_3$, 25°C): δ 1.21 (t, $^3J_{HH}$=7.13 Hz, 3H, CH$_3$), 1.46 (t, $^3J_{HH}$=7.16 Hz, 6H, CH$_3$), 2.59 (t, $^3J_{HH}$=7.61 Hz, 2H, CH$_2$), 3.30 (t, $^3J_{HH}$=7.61 Hz, 2H, CH$_2$), 4.10 (q, $^3J_{HH}$=7.13 Hz, 2H, CH$_2$), 4.48 (q, $^3J_{HH}$=7.16 Hz, 4H, CH$_2$), 8.14 (d, $^3J_{HH}$=11.30 Hz, 2H, H^{5,7}), 8.63 (d, $^3J_{HH}$=11.30 Hz, 2H, H^{4,8}) ppm.

III.2.7. Synthesis of compound **3.6**

EtO₂C ... CO₂Et

Cl ... SR

EtO₂C ... CO₂Et

EtO_2C CO_2Et Cl SR EtO_2C CO_2Et
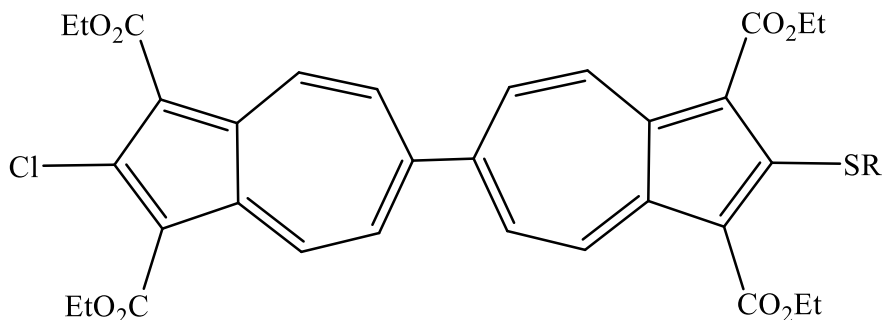
R= -CH₂CH₂COOCH₂CH₃

$R = -CH_2CH_2COOCH_2CH_3$

2-Chloro-1,1',3,3'-tetraethoxycarbonyl-2'-(ethyl-3-thiopropionyl)-6,6'-biazulene- 2-Chloro-1,3-diethoxycarbonyl-6-pinacilatoborylazulene (0.202 g, 0.467 mmol), 1,3-diethoxycarbonyl-2-(ethyl-3-thiopropionyl)-6-iodoazulene (0.248 g, 0.467 mmol), tetrakis(triphenylphosphine) palladium (0.0162 g, 0.0140 mmol), and sodium bicarbonate (0.247 g, 2.95 mmol) were combined in a reaction vessel along with 20 mL of a 1:1 water/ethanol mixture and 10 mL of toluene. The slurry was refluxed at 110°C for 4 hours followed by 8 hours of stirring at room temperature. Upon completion, the reaction was quenched with 100 mL of deionized water, extracted with dichloromethane (3×100 mL), dried with sodium sulfate, and filtered. The solvent was removed under reduced pressure to afford a dark red oil. The oil was subjected to column chromatography (silica gel, 8 cm) with 4:1 hexane/ethyl acetate as eluent. The third (dark red) band was collected, and the solvent was removed under reduced pressure to afford a red oil. The oil was recrystallized by carefully layering pentane over a solution of the oil in dichloromethane and storing it at 5°C overnight. The recrystallization afforded thin red plates **3.6** (0.194 g, 0.274 mmol) in a 57% yield. ¹H NMR (400 MHz, CDCl₃, 25 °C): δ 1.23 (t, $^3J_{HH}$=7.14 Hz, 3H, CH₃), 1.49 (t, $^3J_{HH}$=7.12 Hz, 12H, CH₃), 2.62 (t, $^3J_{HH}$=7.43 Hz, 2H, CH₂), 3.36 (t, $^3J_{HH}$=7.43 Hz, 2H, CH₂), 4.12 (q, $^3J_{HH}$=7.14 Hz, 2H, CH₂), 4.52 (q, $^3J_{HH}$=7.12, Hz, 8H, CH₂), 7.82 (d, $^3J_{HH}$=11.25 Hz, 2H, $H^{5,7}$), 7.93 (d, $^3J_{HH}$=11.26, 2H, $H^{5',7'}$), 9.23 (d, $^3J_{HH}$=11.25 Hz, 4H, $H^{4,8}$), 9.59 (d, $^3J_{HH}$=11.26 Hz, 2H, $H^{4',8'}$) ppm.

III.2.8. Synthesis of compound **3.7**

R= -CH₂CH₂COOCH₂CH₃

R= -CH$_2$CH$_2$COOCH$_2$CH$_3$
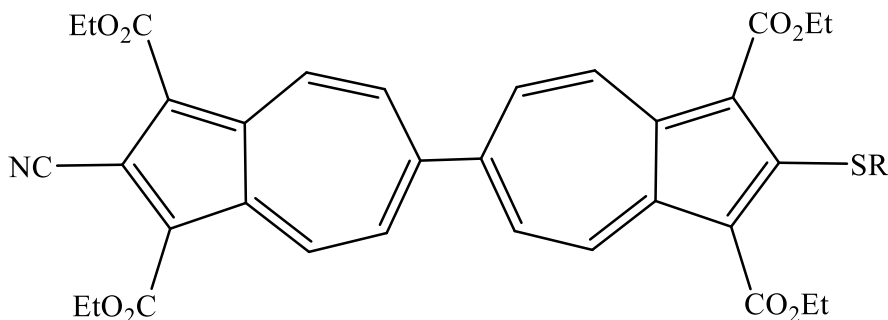
2-Cyano-1,1',3,3'-tetraethoxycarbonyl-2'-(ethyl-3-thiopropionyl)-6,6'-biazulene. - Under argon atmosphere, 2-chloro-1,1',3,3'-tetraethoxycarbonyl-2'-(ethyl-3-thiopropionyl)-6,6'-biazulene (0.272 g, 0.381 mmol), and copper (II) cyanide (0.052 g, 0.575 mmol) were combined with 25 mL of *N,N*-dimethylformamide. The slurry was heated at 120°C for 16 hours and left to cool to room temperature. The reaction was quenched with 100 mL of a 2M solution of sodium cyanide and extracted with a mixture of 1:1 toluene/ethyl acetate (2×100 mL). The organic fraction was dried over anhydrous sodium sulfate, filtered, and the solvent was evaporated under reduced pressure to afford a dark red oil. The oil was subjected to column chromatography (silica gel, 10 cm) with 3:1 hexane/ethyl acetate as eluent. The second (dark orange) band was collected and the solvent was reduced under reduced pressure to afford a dark red oil. The oil was dissolved in dichloromethane and the resulting solution was carefully layered with pentane to crystallize at -5 °C overnight. Thin red flakes of **3.7** were recovered (0.0936g, 0.134mmol) in a 35% yield. Mp: 110-112°C. IR (CH$_2$Cl$_2$): v_{CN} 2230 cm^{-1}. ^{1}H NMR (CDCl$_3$, 400 MHz, 25°C): δ 1.24 (t, ^{3}J$_{HH}$=7.15 Hz, 3H, CH$_3$), 1.50 (t, ^{3}J$_{HH}$=7.10 Hz 6H, CH$_3$), 1.54 (t, ^{3}J$_{HH}$=7.21 Hz 6H, CH$_3$), 2.63 (t, ^{3}J$_{HH}$=7.44 Hz, 2H, CH$_2$), 3.37 (t, ^{3}J$_{HH}$=7.44 Hz, 2H, CH$_2$), 4.13 (q, ^{3}J$_{HH}$=7.15 Hz, 2H, CH$_2$), 4.53 (q, ^{3}J$_{HH}$=7.10 Hz, 4H, CH$_2$), 4.56 (q, ^{3}J$_{HH}$=7.21 Hz, 4H, CH$_2$), 7.81 (d, ^{3}J$_{HH}$=11.17 Hz, 2H, H$^{5',7'}$), 8.06 (d, ^{3}J$_{HH}$=11.20, 2H, H^{5,7}), 9.24 (d, ^{3}J$_{HH}$=11.11.17 Hz, 2H, H$^{4',8'}$), 9.99 (d, ^{3}J$_{HH}$=11.20 Hz, 2H, H^{4,8}) ppm.

III.2.9. Synthesis of compound **3.8**
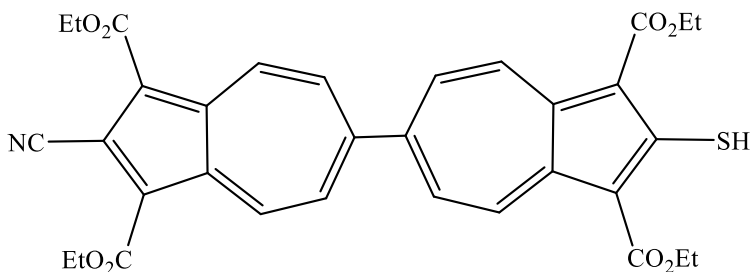
2-Cyano-1,1',3,3'-tetraethoxycarbonyl-2'-mercapto-6,6'-biazulene. – Under argon atmosphere, 2-cyano-1,1',3,3'-tetraethoxycarbonyl-2'-(ethyl-3-thiopropionyl)-6,6'-biazulene (0.070g, 0.100 mmol) was combined with 20.0 mL of ethanol and sonicated to afford a red solution. In a separate reaction vessel, sodium metal (0.010g, 0.435 mmol) and 25.0 mL of ethanol were stirred at room temperature for 30 minutes. The newly formed sodium ethoxide solution was transferred into the biazulene-containing vessel, which triggered a change from a red solution to a purple precipitate. The reaction was stirred at room temperature for 3 hours. Then, 5.0 mL of a 3M solution of sulfuric acid was added dropwise, changing the color of the precipitate to dark red. The reaction was quenched with 100 mL of deionized water and extracted with dichloromethane. The organic layer was washed sequentially with 20 mL portions of deionized water, saturated sodium bicarbonate solution, and brine. Then it was dried with anhydrous sodium sulfate, and the solvent was removed under reduced pressure to afford a red powder. The red powder was subjected to column chromatography (silica gel, 4 cm) using 2:1 hexane/ethyl acetate mixture as eluent. The single, red-colored band was collected, and the solvent was removed under reduced pressure to afford a brown-red powder. The product was subjected to recrystallization by dissolving it in dichloromethane and carefully layering the solution with pentane. This produced dark red needle crystals of **3.8** (0.0433g, 0.0722 mmol) in a 72% yield. Mp: 230-232 °C (dec). Anal. calcd for $C_{33}H_{29}NO_8S$: C, 66.01; H, 4.88; N, 2.34. Found: C, 65.64; H, 4.89; N, 2.23. IR (CHCl$_2$): $\nu_{(CN)}$ =2230 cm^{-1}. IR (KBr): $\nu_{(CN)}$ =2230 cm^{-1}, $\nu_{(SH)}$ =2460 cm^{-1}. UV-Vis (CH$_2$Cl$_2$): λ_{max} (ε=35.5×10^3 M^{-1}cm^{-1}, 25°C): 445 nm. HRMS: calc. (M+Na)= 622.1512, found= 622.154. ^{1}H NMR (CDCl$_3$, 500 MHz, 25°C): δ 1.53 (t, $^3J_{HH}$=7.15 Hz, 6H, CH$_3$), 1.55 (t, $^3J_{HH}$=7.15 Hz, 6H, CH$_3$), 4.55 (q, $^3J_{HH}$= 7.15 Hz, 4H, CH$_2$), 4.55 (q, $^3J_{HH}$= 7.15 Hz, 4H, CH$_2$), 7.81 (s, 1H, SH), 7.90 (d, $^3J_{HH}$= 10.92 Hz, 2H, H$^{5',7'}$), 8.07 (d, $^3J_{HH}$= 10.75 Hz, 2H, H^{5,7}), 9.56 (d, $^3J_{HH}$= 10.92 Hz, 2H, H$^{4',8'}$), 9.99 (d, $^3J_{HH}$= 10.75 Hz, 2H, H^{4,8}) ppm.

III.3 Results and Discussion

III.3.1 Synthetic Overview

Recent synthetic advances in developing symmetrically and asymmetrically substituted 6,6'-biazulenes have expanded the applications of azulenes towards molecular electronics by extending the π-system providing a longer communication range between termini.[7, 8] Asymmetric anchoring groups provide a way of aligning the HOMO and LUMO of the parent molecule to the fermi level of gold electrodes affording rectification and diode-like effects. The substitution targets for this thesis are mercapto and cyano groups, where the latter also serves as a spectroscopic reporter.[6, 9] The synthetic strategy outlined in this thesis takes advantages of other similar schemes recently developed by the Barybin group.[8] However, the synthetic challenge arises in the installation of vastly electronically different mercapto and cyano groups. There are several strategies that one might envision for assembling asymmetrically substituted 6,6'-biazulenes and all involve a thiol protecting group as conditions for the copper mediated cyanation step are not compatible with mercapto groups.[10] The first pathway explored by the author was to synthesize a symmetric 6,6'-biazulenic bridge with protective esters in the 1,1′,3,3' positions through Suzuki coupling and then selectively install cyano and mercapto groups in the 2,2' positions respectively (Scheme **2**). This synthetic pathway was extremely challenging as the symmetric nature of the linker made it impossible to be selective towards the 2 or 2' position.

Scheme 2. Explored synthetic strategy by the author on the assembly of asymmetric functional groups at the termini of the biazulenic π-linker (not achieved).
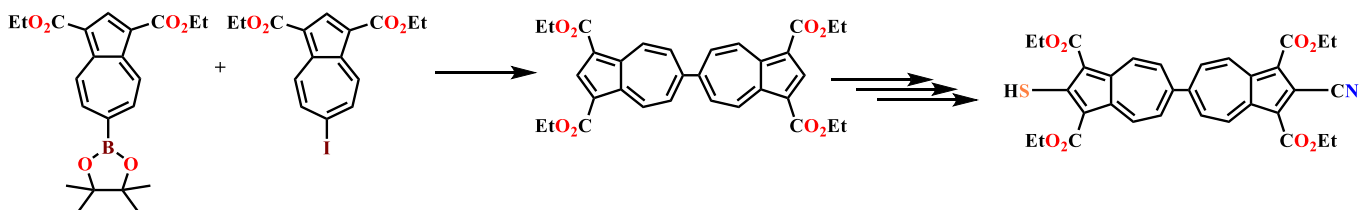
The second synthetic strategy considered by the author was the assembly of azulene derivatives with pre-installed cyano and mercapto groups prior to Suzuki coupling as shown in scheme **3**. Compound **3.3** was subjected to a copper mediated cyanation reaction using CuCN as a cyanide source. This preliminary reaction resulted in substitution of the boryl ester substituent with a cyano group (**3.3a**) as shown in scheme **4**. This selective cyanation arises from the propensity of Cu(I) species to activate boron-carbon (B-C) bonds towards oxidative addition.[11] Moreover, the protective ethoxycarbonyl groups at the 1,3 positions interfere with the substitution reaction by sterically hindering the 2- position where the substitution takes place.[12]

Scheme 3. Explored synthetic strategy for the assembly of asymmetrically substituted 6,6'-biazulenic π-linkers (not achieved).
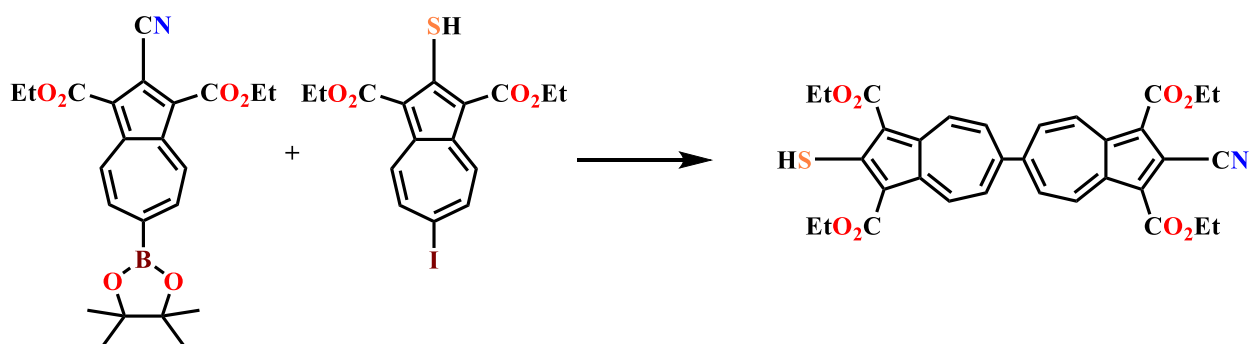
Scheme 4. Synthesis of 2-chloro-6-cyano-1,3-diethoxycarbonylazulene.
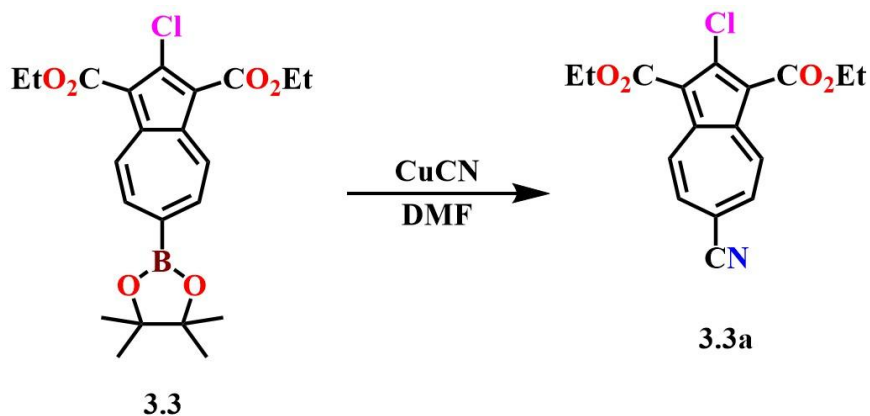
The two previously outlined synthetic strategies were inefficient at producing the desired substitution pattern on the 6,6'-bizulene, so a third strategy was developed. This new strategy involves Suzuki coupling between compounds **3.3** and **3.5** followed by copper mediated cyanation of **3.3** affording **3.7** and cleavage of the protective ester to afford thiol **3.8**. Syntheses for the coupling partners (**3.3** and **3.5**) are shown in Scheme **5**. Treatment of bright yellow 2-aminoazulenyl-1,3-dicarboxylate with bromine affords cyber yellow **3.1** through nucleophilic substitution. Subsequent exposure of **3.1** to bis(pinacolato)diboron in the presence of Pd(II) catalyst in a Miyaura borylation reaction yields bright orange **3.2**. Treatment of **3.2** with dry gaseous HCl produced via the reaction of NaCl and conc. H$_2$SO$_4$ in the presence of isoamyl nitrite produces a green diazonium species in solution that slowly transforms into the chlorinated product **3.3**. Exposure of bright boysenberry colored **3.3** to ethyl-3-mercaptopropionate in the presence of pyridine affords the nucleophilic substitution product **3.4**. Using deep purple **3.4** in a copper mediated deborylation halogenation with CuI produces bright red **3.5** along with considerable yields of the nonhalogenated counterpart of **3.5**.

Scheme 5. Synthesis of coupling partners for assembly of asymmetrically substituted 6,6'-biazulenes.

53
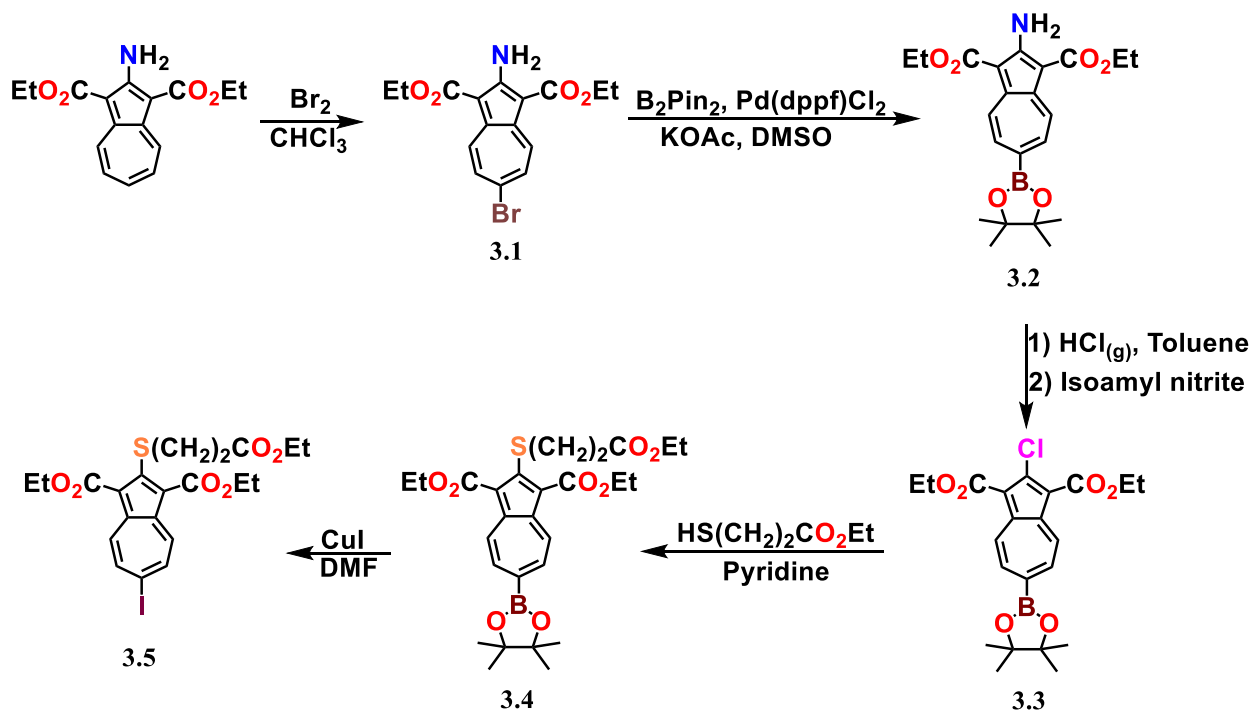
Coupling partners **3.3** and **3.5** are both stable under ambient conditions for months without significant decomposition. Both coupling partners were combined in the presence of Pd(PPh₃)₄ catalyst and potassium acetate under reflux conditions to afford the deep red Suzuki coupling product **3.6** shown in Scheme **6**. Copper mediated cyanation of **3.6** afforded red **3.7** in low yields which may be attributed to steric hindrance interfering with the oxidative addition to the copper species.[12] Cleavage of the protective group of the sulfide with sodium ethoxide forms a green thiolate in solution which is then protonated with 3M H₂SO₄ to afford the deep purple thiol **3.8.**

Scheme 6. Suzuki coupling and further manipulations on asymmetrically substituted 6,6'-biazulenes.
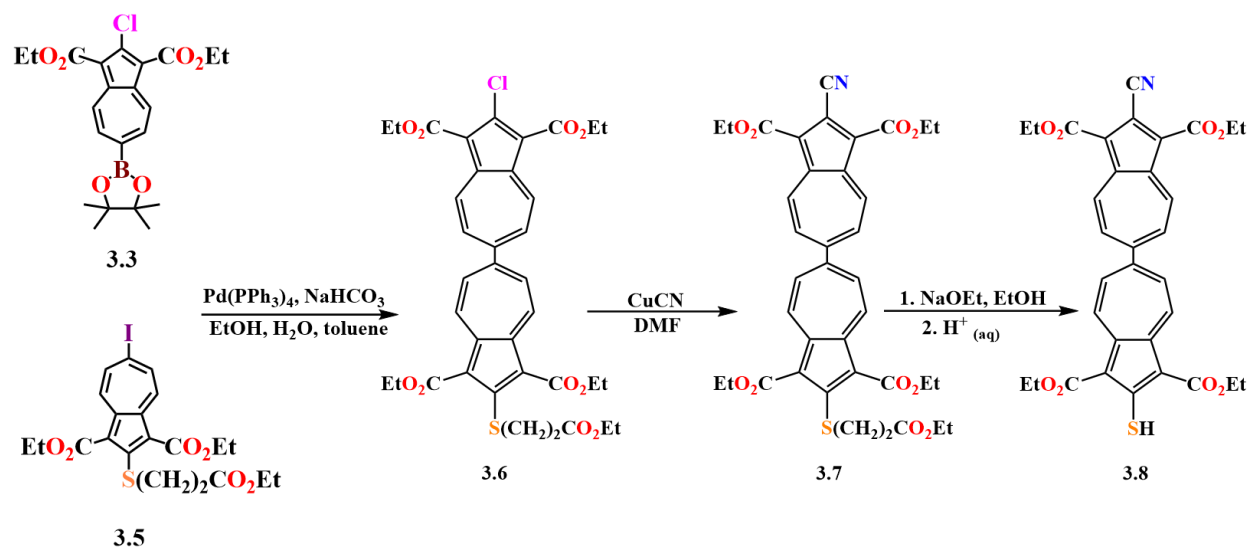
III.3.2. X-Ray Crystallography of **3.6**

Crystallization of **3.6** and **3.8** were achieved by layering pentane over a dichloromethane solution of each respective compound. Crystals for **3.6** adopted irregular shapes resembling thick plate-like shards with deep red coloration. The crystal itself was a weak refractor due to the poor quality of the crystal but a low-resolution crystal structure was generated. In comparison, crystals of **3.8** formed long needles with a purple undertone all shown in fig. **3.1** Work on gathering crystallographic data for compound **3.8** is ongoing.
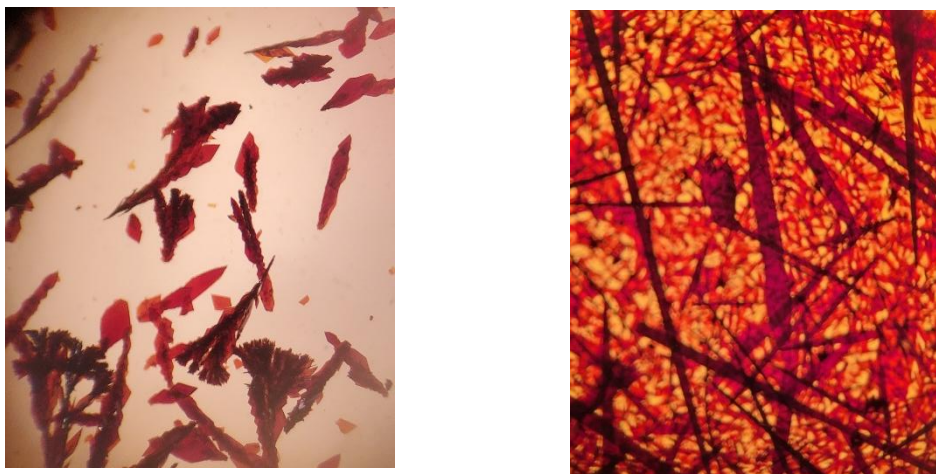
Figure 3.1. Crystals of **3.6** (left) and **3.8** (right) under an optical microscope.

Crystallographic data for crystals of **3.6** (fig. **3.2a**) shows that this compound forms large triclinic unit cell containing six molecules, three in every asymmetric unit. The torsion angle between the 6,6' connections is 36° which is of a considerably lower magnitude compared to the 52° angle obtained through quantum mechanical calculations in the gas phase and can be attributed to crystal packing effects.[7] The torsion angle suggests that efficient conductivity through the molecular backbone might be possible as the azulenic units are not orthogonal to each other.
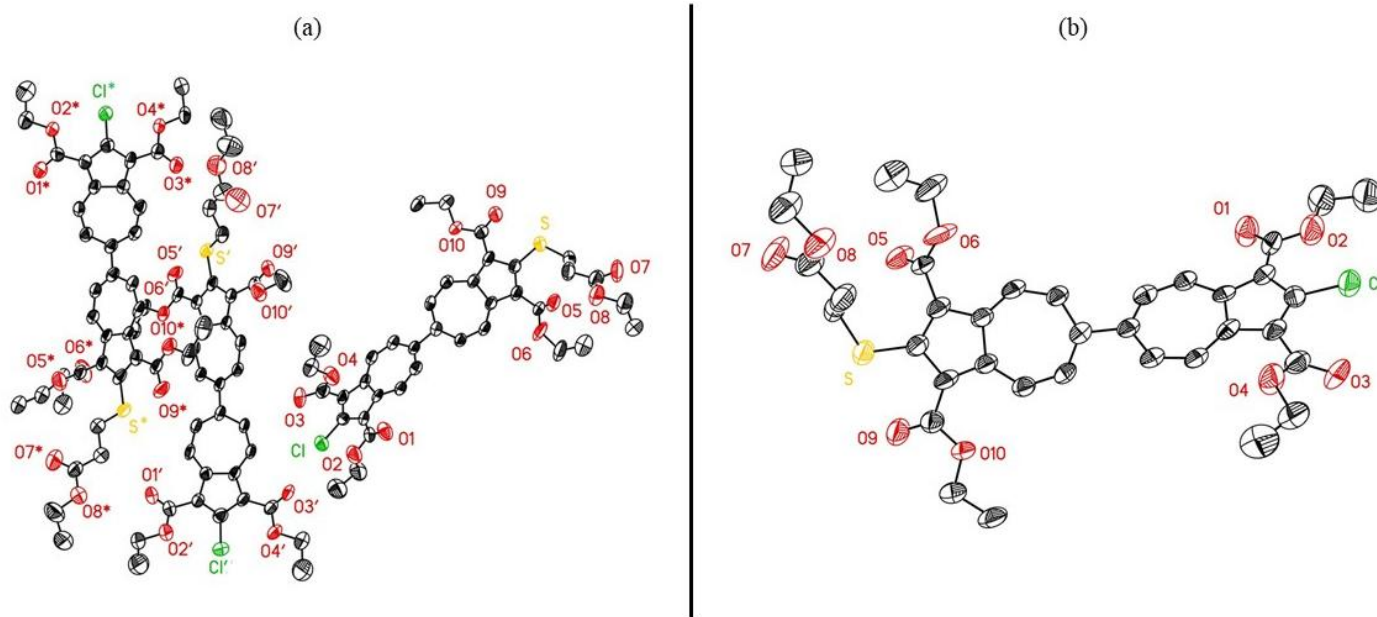
Figure 3.2. (a) ORTEP diagram (50% thermal ellipsoids) of **3.6** in the asymmetric unit containing three independent molecules. (b) Expanded version of the asymmetric unit showing a single molecule.

55

III.3.3. Electronic Absorption Studies

Compounds **3.6**, **3.7**, and **3.8** are red in color. The lowest energy electronic absorption for **3.6** occurs at 443 nm ($\varepsilon = 30.4 \times 10^3$ M^{-1}cm^{-1}) and is 12 nm blue-shifted compared to the transition observed for **3.7** (fig. **3.3**). The blue-shift is due to the greater electron withdrawing effect of the cyano- group of **3.7** compared to the chloro- group of **3.6** affecting the LUMO energy of the biazulenic scaffold.[13, 14] This stabilization reduces the HOMO-LUMO energy gap causing a blue-shift of **3.6** vs. **3.7**. Compound **3.8** shows a slight blue-shift compared to **3.7** with a maximum absorption peak in the visible region at 445 nm ($\varepsilon = 35.3 \times 10^3$ M^{-1}cm^{-1}). This blue-shift is due to the cleavage of the protective tail at the 2'- position to afford a thiol. By cleaving the ester group, the thiol becomes more electron donating, destabilizing the energy of the LUMO, and increasing the HOMO-LUMO energy gap.
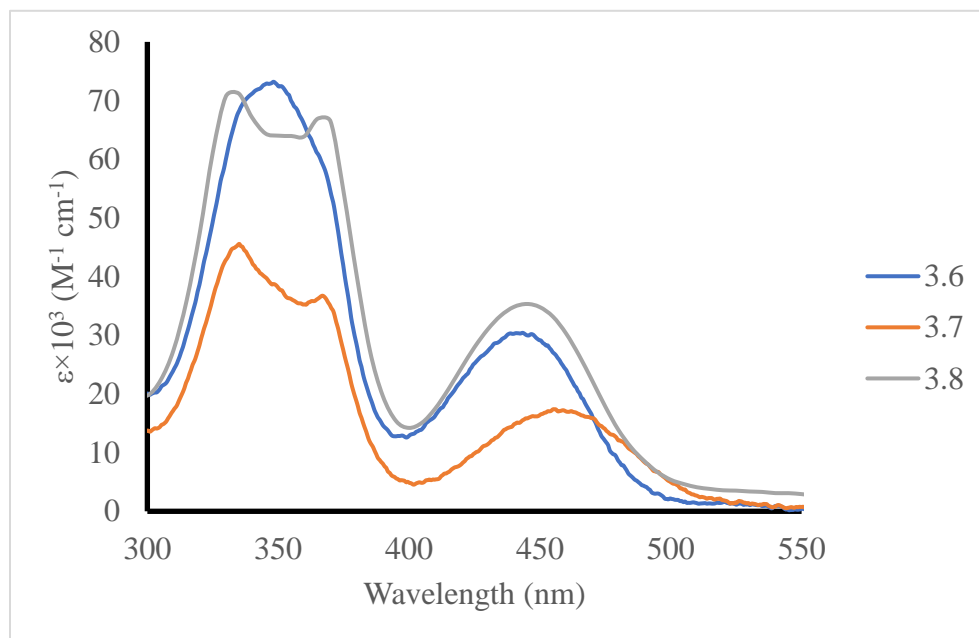
Figure 3.3. UV-Vis spectra of **3.6**-**3.8** in CH$_2$Cl$_2$ at a concentration of 5.0μM at 25°C.

Further evidence of the presence of a thiol group in the biazulenic linker was observed upon deprotonation of the mercapto moiety with a UV-Vis transparent base such as 1,8-diazabicyclo[5.4.0]undec-7-ene (DBU). Excess DBU was added to a 5μM solution of **3.8** to afford the thiolate salt **3.9** (scheme **6**). Compound **3.9** is 250 nm red-shifted compared to compound **3.8**

(fig. **3.4**). This can be attributed to an increase in electron withdrawing effects upon deprotonation from thiol to thiolate, stabilizing the LUMO energy, and reducing the HOMO-LUMO energy gap. Scheme **6** depicts the deprotonation process where the thiol forms an equilibrium with the thiolate species. A drastic change of color occurred immediately after the addition of excess DBU, from orange to forest green. The dark green solution of **3.9** showed signs of decomposition after 30 minutes of being exposed to ambient condition by the formation of a dark precipitate and the discoloration of the green solution to light brown.

Scheme 7. Deprotonation equilibrium of **3.8** with DBU
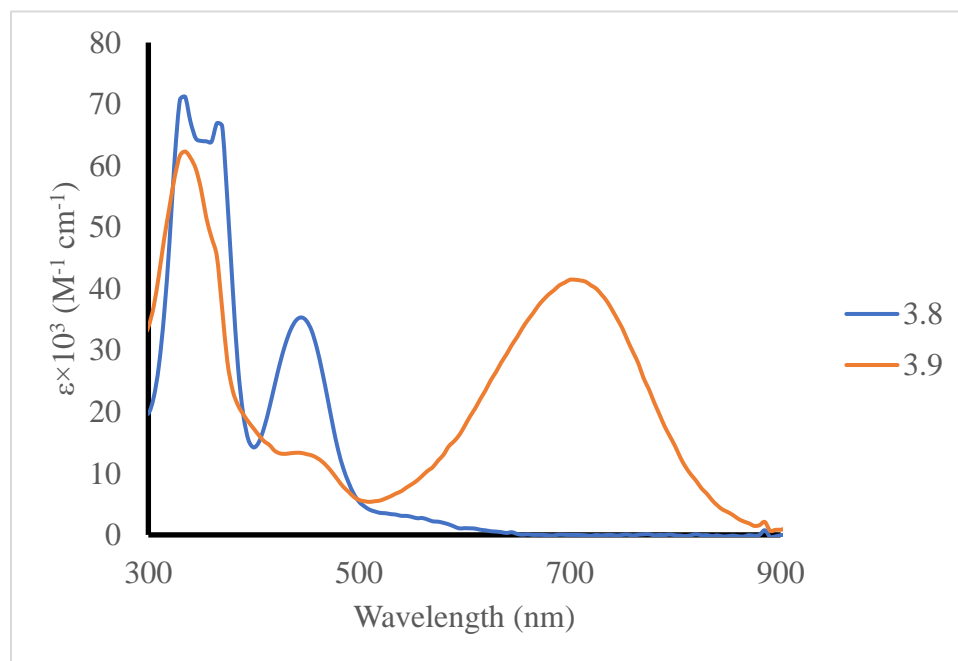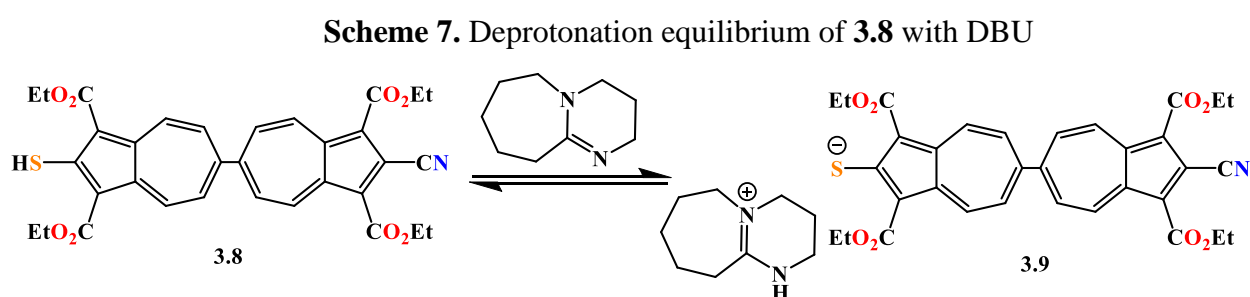
Figure 3.4. UV-Vis spectra of **3.8** and **3.9** in CH$_2$Cl$_2$ at 25°C.

III.3.4. Electrochemical Profile of Asymmetrically Substituted 6,6'-biazulenes

In the past, the Barybin group has observed strong electronic coupling between the 2 and 2' termini of the symmetrically substituted diisocyano analog of **3.8** through cyclic voltammetry and computational methods.[7] When studying the redox profiles of the asymmetrically substituted 6,6'-biazulenic derivatives, it became clear that there was strong electronic coupling between each half of the molecule through a shift of the entire 2e$^-$ wave instead of a separation into two 1e$^-$ reduction waves previously discussed in chapter II. In the case where the asymmetric linker does not exhibit communication through the azulenic sub-units, the single 2e$^-$ reduction wave would split into two 1e$^-$ reduction waves as the asymmetry featured in the molecules would force different reduction potentials for each azulenic sub-unit.[8, 15] As seen in fig. **3.5**, this is not the case for this set of compounds.
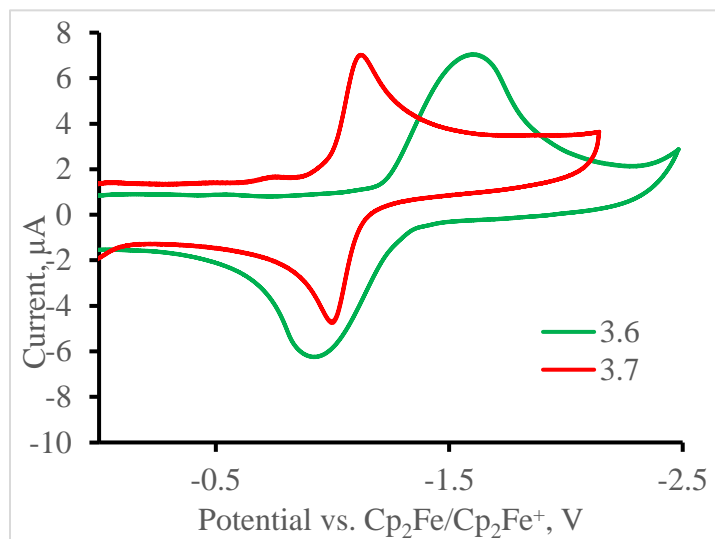
Figure 3.5. Cyclic voltammograms of **3.6** and **3.7** in 0.1M [^{n}Bu$_4$N][PF$_6$] in CH$_2$Cl$_2$ at 25°C referenced against Cp$_2$Fe/Cp$_2$Fe$^+$ couple.

The cyclic voltammograms of **3.6** and **3.7** features a shift of the 2e$^-$ wave reduction potentials suggesting electronic coupling between termini based on the relatively less negative E$_{1/2}$ reduction potentials. As observed, the redox profiles feature a 2e$^-$ reversible reduction consistent

with previous results for other asymmetrically substituted 6,6'-biazulenes.[8, 16] Furthermore, the $E_{1/2}$ potentials for **3.6** (-1.26 V) vs. **3.7** (-1.07 V) are consistent with the change in functional groups from -Cl to -CN. The stronger electron withdrawing effect of the cyano group causes a decrease in electron density through the biazulenic backbone, which decreases electron repulsion, and shifts the redox wave to less negative potentials when compared to the chloro derivative.[17, 18] In this case, the electrochemical profiles for **3.6** and **3.7** suggest electronic coupling between the termini of each azulenic sub-unit and proper substitution of -Cl with -CN group.

III.3.5. FTIR Analysis

Fourier-Transform Infrared Spectroscopy (FTIR) offers insight into the identity of different functionalities in molecules that other characterization techniques might not be sensitive to. Compound **3.8** features -SH and -CN groups which are both IR active, although the -CN group is a relatively strong oscillator compared to -SH. The mercapto functionality usually exhibits a broad, weak signal between ν_{SH}=2600-2550 cm^{-1} and is traditionally resolved in the solid-state. The position of substitution on the azulenic sub-units also influences the energy range in which the features for -SH and -CN stretches will appear due to the difference in electron density between the five- and seven-membered rings.

The solid-state IR spectrum for 2,6-dimercaptoazylenyl-1,3-dicarboxylate (DMA) shows two distinct -SH features corresponding to the 2 and 6 substitutions (fig. **3.6**).[16] The two distinct thiol signals arise from the intramolecular hydrogen bonding interactions between 2-SH and the carbonyl oxygen in the ester protecting groups in the 1 and 3 positions. The frequency for $\nu_{2\text{-SH}}$=2430 cm^{-1} and the intensity of the signal are both consistent with a weaker oscillator due to hydrogen bonding and $\nu_{6\text{-SH}}$=2540 cm^{-1} is consistent with a free thiol.
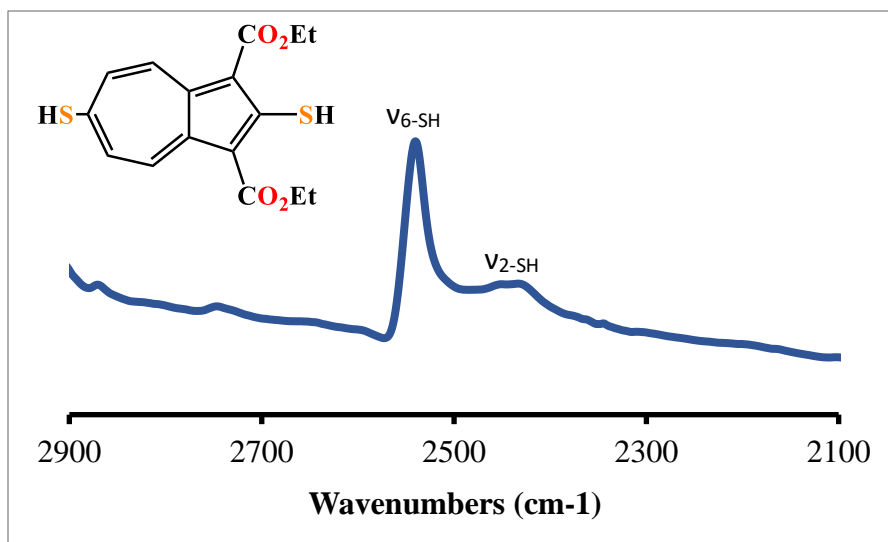
Figure 3.6. FTIR spectrum of DMA in KBr.[19]

Cyano groups are generally more resolved than thiols both in the solid-state and in solution FTIR spectroscopy and have been used as spectroscopic reporters in previous work.[9, 20] Azulenes with a -CN substituent on the second position exhibit a sharp but weak signal at $\nu_{2\text{-CN}}=2223$ cm^{-1} which is at higher energy than the 6-CN isomer due to the electron rich five- membered ring vs. the electron deficient seven- membered ring of the azulenic scaffold.[21] The solid-state FTIR spectrum for compound **3.8** (fig. **3.7**) shows characteristic features consistent with -SH and -CN moieties, which suggests the desired substitution pattern in the 6,6'-biazulenic motif. The -CN signal ($\nu_{CN}=2230$ cm^{-1}) shows a slight blue-shift from the literature value due to the substitution pattern at the 6- position of the azulenic sub-unit. The thiol signal ($\nu_{SH}=2460$ cm^{-1}) is also consistent with the expected shift for a hydrogen bonded thiol at the 2'- position of the biazulenic framework, although blue-shifted from literature sample values due to the electron withdrawing nature of the 2-cyanoazulenyl motif at the 6- position of the azulenic sub-unit.[19] However, there is an artifact at $\nu=2585$ cm^{-1} that could be attributed to molecules in the crystal lattice that so not participate in hydrogen bonding interactions through the thiol moiety. To unambiguously assign the thiol feature, a deuterium exchange experiment could be performed and will be discussed in more detail in chapter IV of this thesis.
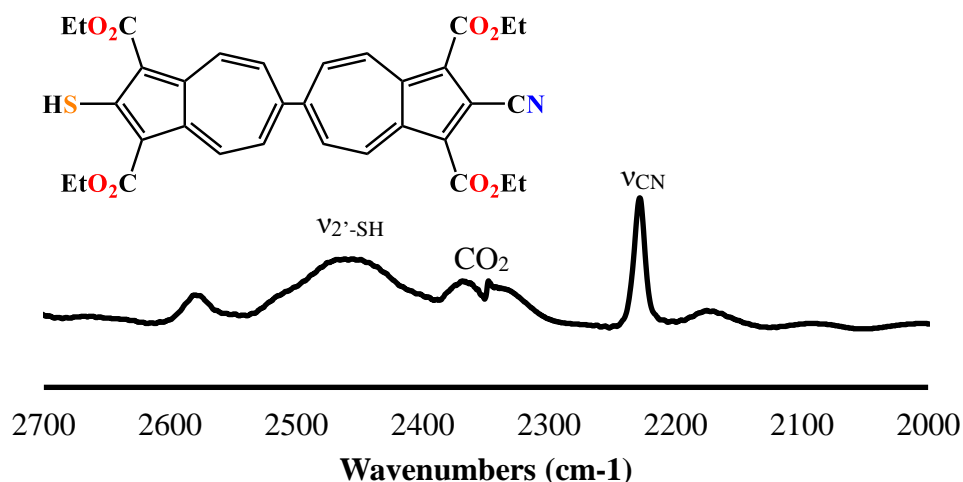
Figure 3.7. FTIR of compound **3.8** in KBr

An interesting way of probing communication between termini in compound **3.8** would be to deprotonate the thiol at the 2'- position of the biazulenic framework with DBU to produce compound **3.9** and study the response of the -CN feature in the IR spectrum. Figure **3.8** shows the IR spectra of **3.8** and **3.9** in CH_2Cl_2 showing the response of the -CN feature upon deprotonation of the thiol. The highest energy peak at ν_{CN}=2230 cm^{-1} in the **3.8** spectrum does not change significantly upon deprotonation, but there are two newly formed features in the frequency range for -CN moieties. The most intense of the two features, ν=2212 cm^{-1} could be assigned to the thiolate species in chemical equilibrium with thiol **3.8** as the red-shift is consistent with having a relatively more electron-rich substituent at the 6- position of the biazulenic scaffold which would weaken the -CN stretch. The third peak seen at ν=2199 cm^{-1} could be attributed to some decomposition side product upon exposure to ambient conditions. A possible side product might include disulfide species which would create a symmetrical tetrazulene species, giving rise to a single -CN signal at even lower energies.
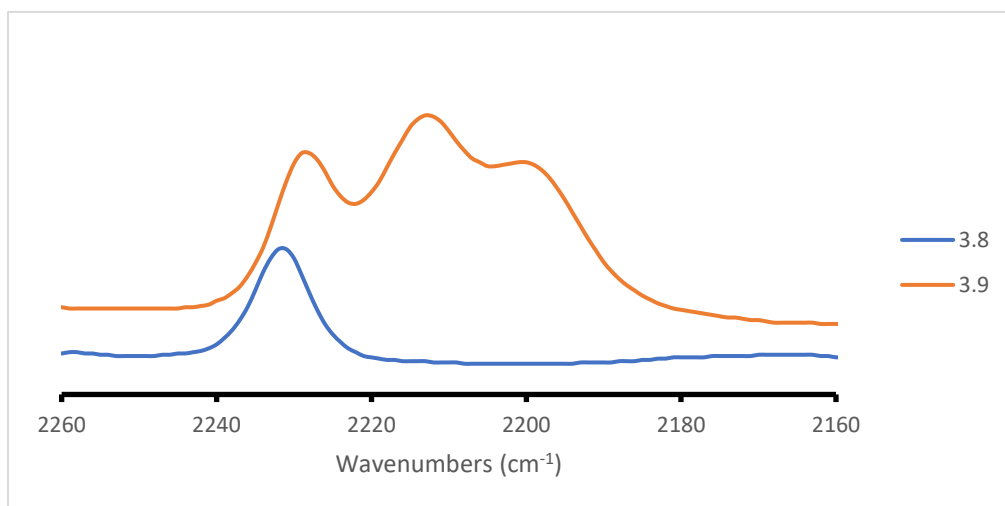
Figure 3.8. FTIR of compounds **3.8** and **3.9** in CH_2Cl_2.

III.3.6. Self-Assembled Monolayers

Self-assembly of compound **3.8** on Au(111) surfaces should create uniform monolayers oriented upright with respect to the surface. Mercapto functionalities are not easily resolved using Reflection-Absorption Infrared Spectroscopy (RAIRS) due to the small number of molecules being irradiated with incident infrared radiation arising from the incident angle required for the spectroscopic technique. However, cyano substituents should provide sufficient oscillatory strength to function as a spectroscopic reporter based on literature reports.[9, 20]

Ongoing work involves the formation of SAMs on Au(111) surfaces. Up until now, no evidence of SAM formation has been observed for compound **3.8** using conventional monolayer formation methods. The first batch of Au(111) samples submerged in a 2 mM solution of **3.8** in CH_2Cl_2 produced a cloudy film on the surface noticeable to the naked eye. This suggests the formation of aggregates held together by π-interactions deposited on the surface, creating a multilayer film on the surface which could indicate that the solution was too concentrated to form uniform SAMs. To solve this, the concentration of the solution was reduced by three orders of magnitude and a second batch of samples was created. After 24 hours, the second batch was examined and there was no noticeable cloudy film, but there was no sign of SAM formation evidenced by RAIR and the ellipsometric film thickness was not consistent with the calculated length of compound **3.8**. The next variable altered was the solvent, which was changed from

CH$_2$Cl$_2$ to THF to account for any solubility issues that may be causing precipitation of the compound on the gold surface. However, there was no spectroscopic evidence suggesting the formation of SAMs for this trial either. Other changes in variables were explored such as preparing the samples under inert conditions using distilled CH$_2$Cl$_2$ as solvent, increasing the submersion time of the gold surface in solution, and sonicating the gold samples as an additional cleaning step, but none of these changes made a difference on the RAIR spectra of the samples.

A batch of samples was prepared and left in a refrigerator over a period of 48 hours, hoping that the lower temperature would allow for the formation of monolayers as the kinetic energy for the molecules is reduced. Figure **3.9** appears to show a small feature in the energy range consistent with a -CN functionality. However, the absence of a sharp peak suggests that the film is not oriented perpendicular to the surface. Experimental ellipsometric thickness was too large compared to the theoretically calculated thickness of **3.8** suggesting that the film is not a monolayer, but rather, a multilayer film possibly consisting of aggregates held together by π-stacking interactions. In the hopes that self-assembly in even cooler temperatures would create well-ordered monolayers, a final batch of samples was left to form at -20°C. After 24 hours, the samples were cleaned with neat CH$_2$Cl$_2$ and dried with nitrogen to reveal a thick cloudy film over the gold surface sample. Upon collecting an RAIR spectrum, no -CN signals were observed and the ellipsometric thickness measured was well over 200 nm. Although disappointing, these results give possible insight on the intermolecular interactions of compound **3.8**.

The Barybin group has shown examples of intramolecular hydrogen bonding between the -SH functionality and the carbonyl oxygen in the protective ester groups at the 1,3 positions of the azulenic framework through IR and XRD studies.[19] Compound **3.8** should also exhibit this intramolecular hydrogen bonding as the 2'-mercapto substitution is subject to the same effects. Moreover, compound **3.8** also contains a cyano group which have also been shown to partake in hydrogen bonding interactions due to the lone pair of electrons in the nitrile nitrogen. In 2013, Senthilkumar and coworkers showed significant hydrogen bonding between several isomers of a nitrile substituted small molecule and H$_2$S molecules in a theoretical investigation using B3LYP, MP2 perturbation methods, 6-311 + + G(d,p) basis set.[22] The combination of these two interactions might interfere with the formation of ordered monolayers. By decreasing the temperature, all the π-stacking and hydrogen bonding interactions should increase accounting for the thick multilayer

film observed for the low temperature experiments. However, in 2000, Ousaki and coworkers studied the structure of SAMs of decanethiol on Au(111) by varying the temperature of solution. They studied the samples with STM and found that monolayers formed at 78°C showed less defects and better ordering when compared to a set of lower temperatures.[23] Therefore, suggestions for future experiments lay in increasing the temperature of the immersion solution, constraint by the solvent, and varying the immersion time. The higher temperature of solution should break some of the inter- and intramolecular interactions and reducing the immersion time could potentially reduce aggregation on the surface.
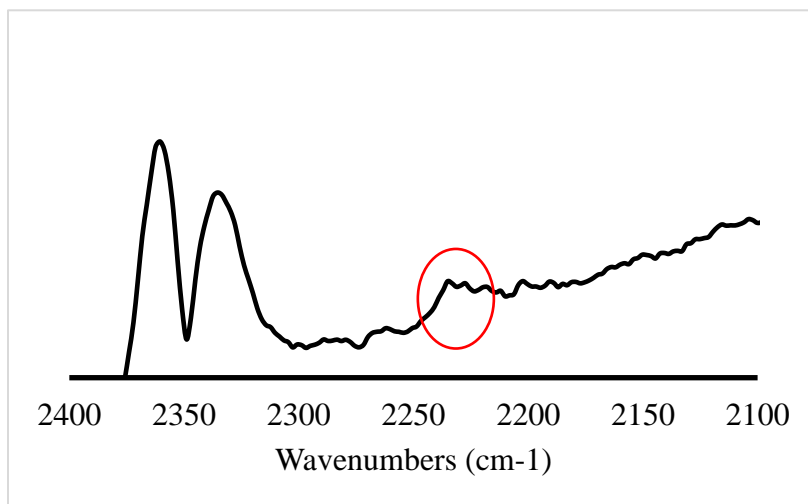
Figure 3.9. RAIR spectrum of **3.8** on Au(111) surface prepared at ~12°C.

III.4 Conclusions and Outlook

The project described in the third chapter of this thesis shows an efficient synthesis for the development of asymmetrically substituted 6,6'-buazulenic molecular linkers using Suzuki coupling, and further manipulations of the coupled product to achieve a 2-cyano-2'-mercapto substitution pattern along the molecular axis of the biazulenic scaffold. X-Ray crystallography and elemental analysis confirm the identity of compound **3.8** and it features an interazulenic torsion angle of 36° due to crystal packing effects. Electronic absorption studies show shifts consistent

with the electronic effects expected for each synthetic step in the 6,6'-biazulenic framework and deprotonation experiments with DBU further evidences the presence of the mercapto moiety. Cyclic voltammograms of compounds **3.6** and **3.7** show electronic coupling between the azulenic sub-units in the asymmetrically substituted biazulenic motif by the shift of the single 2e$^-$ reduction wave. FTIR analysis of compound **3.8** reveal features consistent with the desired substitution pattern in the biazulenic framework. Electronic coupling was further evidenced by a shift of the -CN feature in the IR spectrum upon deprotonation of **3.8**. The formation of SAMs of compound **3.8** on Au(111) was not observed through IR spectroscopic or ellipsometric methods. Several changes to the monolayer formation protocol were implemented but none showed evidence of monolayer growth. Speculation as to why ordered monolayers did not form at lower preparation temperature include inter- and intramolecular hydrogen bonding interactions between the thiol and cyano group, and thiol and carbonyl oxygen, respectively. Future experimental suggestions involve increasing the temperature of the solution during sample preparation and varying the immersion times of the gold sample in said solution to reduce intermolecular interactions and to reduce the chance for aggregation on the surface.

III.5 References

1.	Bürgi, T., Properties of the gold–sulphur interface: from self-assembled monolayers to clusters. *Nanoscale* **2015,** *7* (38), 15553-15567.

2.	Ulman, A., *An Introduction to Ultrathin Organic Films From Langmuir-Blodgett to Self-Assembly*. Academic Press: San Diego, CA, 1991.

3.	Watanabe, H.; Kato, H., Thermal Conductivity and Thermal Diffusivity of Twenty-Nine Liquids: Alkenes, Cyclic (Alkanes, Alkenes, Alkadienes, Aromatics), and Deuterated Hydrocarbons. *Journal of Chemical & Engineering Data* **2004,** *49* (4), 809-825.

4.	Tachibana, M.; Yoshizawa, K.; Ogawa, A.; Fujimoto, H.; Hoffmann, R., Sulfur−Gold Orbital Interactions which Determine the Structure of Alkanethiolate/Au(111) Self-Assembled Monolayer Systems. *The Journal of Physical Chemistry B* **2002,** *106* (49), 12727-12736.

5.	Cuevas, J. C. S., E., *Molecular Electronics: An Introduction to Theory and Experiment*. World Scientific: Singapore, 2010; Vol. 1.

6.	Van Dyck, C.; Ratner, M. A., Molecular Rectifiers: A New Design Based on Asymmetric Anchoring Moieties. *Nano Letters* **2015,** *15* (3), 1577-1584.

7.	Maher, T. R.; Spaeth, A. D.; Neal, B. M.; Berrie, C. L.; Thompson, W. H.; Day, V. W.; Barybin, M. V., Linear 6,6′-Biazulenyl Framework Featuring Isocyanide Termini: Synthesis, Structure, Redox Behavior, Complexation, and Self-Assembly on Au(111). *Journal of the American Chemical Society* **2010,** *132* (45), 15924-15926.

8.	Applegate, J. C.; Okeowo, M. K.; Erickson, N. R.; Neal, B. M.; Berrie, C. L.; Gerasimchuk, N. N.; Barybin, M. V., First π-linker featuring mercapto and isocyano anchoring groups within the same molecule: synthesis, heterobimetallic complexation and self-assembly on Au(111). *Chemical Science* **2016,** *7* (2), 1422-1429.

9.	Neal, B. M.; Vorushilov, A. S.; DeLaRosa, A. M.; Robinson, R. E.; Berrie, C. L.; Barybin, M. V., Ancillary nitrile substituents as convenient IR spectroscopic reporters for self-assembly of mercapto- and isocyanoazulenes on Au(111). *Chemical Communications* **2011,** *47* (38), 10803-10805.

10.	Molloy, J. J.; O'Rourke, K. M.; Frias, C. P.; Sloan, N. L.; West, M. J.; Pimlott, S. L.; Sutherland, A.; Watson, A. J. B., Mechanism of Cu-Catalyzed Aryl Boronic Acid Halodeboronation Using Electrophilic Halogen: Development of a Base-Catalyzed Iododeboronation for Radiolabeling Applications. *Organic Letters* **2019,** *21* (7), 2488-2492.

11.	Zhang, G.; Lv, G.; Li, L.; Chen, F.; Cheng, J., Copper-catalyzed halogenation of arylboronic acids. *Tetrahedron Letters* **2011,** *52* (16), 1993-1995.

12.	Yamazaki, Y.; Naganuma, J.; Gotoh, H., A theoretical, dynamical evaluation method of the steric hindrance in nitroxide radicals using transition states of model reactions. *Scientific Reports* **2019,** *9* (1), 20339.

13.	Xin, H.; Gao, X., Application of Azulene in Constructing Organic Optoelectronic Materials: New Tricks for an Old Dog. *ChemPlusChem* **2017,** *82* (7), 945-956.

14.	Xin, H.; Hou, B.; Gao, X., Azulene-Based π-Functional Materials: Design, Synthesis, and Applications. *Accounts of Chemical Research* **2021,** *54* (7), 1737-1753.

15.	Qu, X.; Persson, K. A., Toward Accurate Modeling of the Effect of Ion-Pair Formation on Solute Redox Potential. *Journal of Chemical Theory and Computation* **2016,** *12* (9), 4501-4508.

16.	Holovics, T. C.; Robinson, R. E.; Weintrob, E. C.; Toriyama, M.; Lushington, G. H.; Barybin, M. V., The 2,6-Diisocyanoazulene Motif: Synthesis and Efficient Mono- and Heterobimetallic Complexation with Controlled Orientation of the Azulenic Dipole. *Journal of the American Chemical Society* **2006,** *128* (7), 2300-2309.

17.	Elgrishi, N.; Rountree, K. J.; McCarthy, B. D.; Rountree, E. S.; Eisenhart, T. T.; Dempsey, J. L., A Practical Beginner's Guide to Cyclic Voltammetry. *Journal of Chemical Education* **2018,** *95* (2), 197-206.

18.   Kissinger, P. T.; Heineman, W. R., Cyclic voltammetry. *Journal of Chemical Education* **1983,** *60* (9), 702.

19.   Scheetz, K. J.; Spaeth, A. D.; Vorushilov, A. S.; Powell, D. R.; Day, V. W.; Barybin, M. V., The 2,6-dimercaptoazulene motif: efficient synthesis and completely regioselective metallation of its 6-mercapto terminus. *Chemical Science* **2013,** *4* (11), 4267-4272.

20.   Wächter, T.; Scheetz, K. J.; Spaeth, A. D.; Barybin, M. V.; Zharnikov, M., Dynamics of Electron Transfer in Azulene-Based Self-Assembled Monolayers. *The Journal of Physical Chemistry C* **2017,** *121* (25), 13777-13785.

21.   Robinson, R. E.; Holovics, T. C.; Deplazes, S. F.; Powell, D. R.; Lushington, G. H.; Thompson, W. H.; Barybin, M. V., Five Possible Isocyanoazulenes and Electron-Rich Complexes Thereof: A Quantitative Organometallic Approach for Probing Electronic Inhomogeneity of the Azulenic Framework. *Organometallics* **2005,** *24* (10), 2386-2397.

22.   Venkatachalam, U.; Senthilkumar, L.; Kolandaivel, P., Theoretical investigations on the hydrogen bonding of nitrile isomers with H2O, HF, NH3 and H2S. *Molecular Simulation* **2013,** *39*, 908.

23.   Yamada, R.; Wano, H.; Uosaki, K., Effect of Temperature on Structure of the Self-Assembled Monolayer of Decanethiol on Au(111) Surface. *Langmuir* **2000,** *16* (13), 5523-5525.

Chapter IV

IV: Conclusions and Outlook for Future Work

IV.1. Conclusions and Outlook for Future Work

The research presented in this thesis involved the synthesis and spectroscopic characterization of a new 6,6'-biazulenic π-linker terminated with -SH and -CN substituents at the 2 and 2' positions of the biazulenic scaffold. A low-resolution crystal structure for 2-chloro-1,1',3,3'-tetraethoxycarbonyl-2'-(ethyl-3-thiopropionyl)-6,6'-biazulene was obtained and it revealed an interplanar angle of 36° between the two azulenyl moieties. Electronic absorption studies performed on compounds **3.6**, **3.7**, and **3.8** showed maximum absorptions for the S→π* biazulenyl transition at 443, 460, and 445 nm respectively, which is consistent with the expected shifts based on the electronic properties of the functionalities in each compound. The installation of the mercapto terminus at the 2-position of the biazulenic framework was confirmed by ^{1}H NMR spectroscopy, FTIR spectroscopy, and deprotonation of the -SH unit to form the corresponding biazulenyl thiolate. The electronic absorption spectra of the biazulenyl thiolate derivative showed the disappearance of the absorption peak at 445 nm corresponding to the thiol derivative and the appearance of a broader feature with maximum absorption at 715 nm. This shift is consistent with deprotonation of the thiol derivative since the installation of a more electron withdrawing group would reduce the HOMO-LUMO energy gap.

The redox profiles of compounds **3.6** and **3.7** were examined through cyclic voltammetry which indicated electron delocalization across both azulenic sub-units based on the less negative $E_{1/2}$ reduction potentials relative to the irreversible reduction of monomeric azulenyl derivatives.[1] The voltammogram features a single 2e$^-$ reduction wave, typically observed for 6,6'-biazulene derivatives in solvents of moderate polarity such as CH_2Cl_2. The 6,6'-biazulenic systems are often subject to potential compression/inversion as evidenced by the single 2e$^-$ reduction wave as opposed to two 1e$^-$ reductions. This potential compression/inversion can be attributed to an increase in planarity of the 6,6'-biazulenic motif upon the first reduction and to contact ion-pairing effects between the [$^nBu_4N$]$^+$ and the singly-reduced 6,6'-biaulenyl species.

FTIR studies show features consistent with -CN and -SH functionalities. Further evidence of electronic coupling between each azulenic sub-unit was obtained by monitoring the shift of the -CN stretching vibration band with FTIR spectroscopy upon deprotonation of the thiol group. The FTIR spectrum showed two new peaks in the -CN stretch range red-shifted with respect to the

reference -CN peak that are attributed to the thiolate species and an additional decomposition product, possibly a disulfide species.

There was no RAIR spectroscopic or ellipsometric evidence that supported the formation of ordered SAMs of the -CN and -SH terminated 6,6'-biazulene, **3.8**, on Au(111). Instead, visual evidence of a thick cloudy film over the gold surface samples and ellipsometric thicknesses well over 200 nm suggest multilayer aggregates deposited on the surface. Several changes to the general sample preparation procedure, which included decreasing the concentration of the immersion solution, change in solvents, improved surface cleaning procedures, sample preparation under inert atmosphere, and increasing the immersion time of the gold surface sample in solution, were implemented but none of these changes improved SAM formation. RAIR spectra of samples prepared at 5°C seem to show a small and relatively broad peak in the ν_{CN} frequency range, which indicates disorder in the molecular film based on RAIR selection rules. Ellipsometric film thicknesses of these samples were over 200 nm, which further suggests multilayer film or aggregates. Samples prepared at -20°C, holding concentration (5 μM) and immersion time (24 hours) identical to the 5°C sample preparation experiment, generated a cloudy film over the surface sample, similar to experiments conducted at higher concentrations (2 mM). Speculation as to the reason why these thick cloudy films formed revolves around intramolecular hydrogen bonding interactions between the -SH terminus and the oxygen of the carbonyl group in the protective ester substituent, and possibly, intermolecular hydrogen bonding interactions between the -CN and -SH functionalities. Moreover, 6,6'-biazulene derivatives are prone to π-stacking interactions that could deposit on the gold surface to create multilayer films or aggregates. These interactions would increase with higher solution concentrations and lower temperatures, which is consistent with experimental observations. Further modifications for future experiments include increasing the solution temperature to break some of these intra- and intermolecular interactions, as well as reducing the immersion times to avoid major aggregate deposition on the surface.

Another exciting future project will involve probing the extent of conductivity and rectification of SAMs of compound **3.8** using conductive atomic force microscopy (C-AFM). C-AFM is a microscopy technique that provides simultaneous topographical and conductivity maps at the nanoscale.[2] This method is capable of decoupling topography and conductivity which makes it an attractive alternative to STM, where conductivity controls the feedback loop. The C-AFM

set-up requires additional components that are not normally found in a usual AFM experiment. Those components are: i) a tip coated with a conductive material, ii) a voltage source that applies a potential difference between the tip and the sample, and iii) an amplifier that amplifies the very small currents to be easily measurable, and drives an analog-to-digital converter (ADC) which converts analog signals into digital ones. The setup loop is shown in fig. **4.1** where a tip coated with a conductive material is connected to a current amplifier (in principle, the current could be measured anywhere on the circuit), which amplifies the current signal at a given DC bias, applied via the sample holder; this gives a conductivity image. At the same time, a topography image is generated based on the changes detected at the Position Sensitive Photo-Detector (PSDS) caused by the deflection of the cantilever due to the topography of the sample.[3]
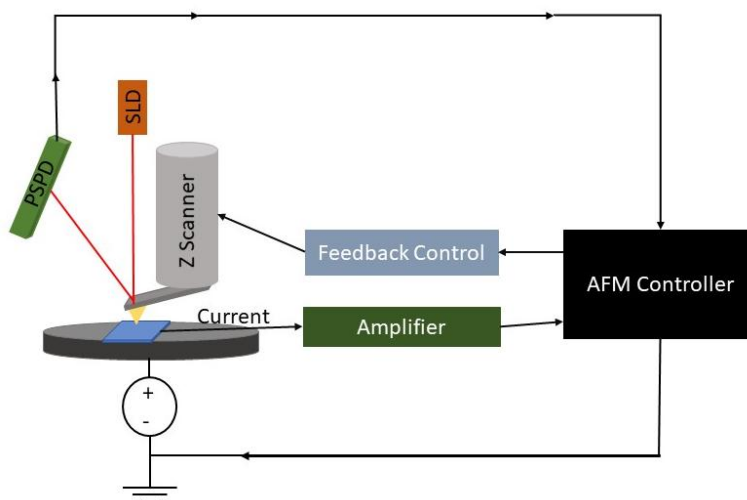
Figure 4.1. Schematic of a C-AFM setup where the light source is a super luminescent diode (SLD).

It is imperative that C-AFM measurements are performed on SAMs of compound **3.8** to evaluate its usefulness as a component in molecular electronic devices. Assuming that monolayers of compound **3.8** form upright with respect to the surface through a thiolate junction, the C-AFM tip would come into contact with the -CN termini and would produce data for conductivity through the 6,6'-biazulenic backbone. Furthermore, the extent of rectification or diode behavior, expected due to the substitution pattern with electron withdrawing -CN and electron donating -SH along the molecular axis, could be examined by identifying any asymmetry in the recorded I-V curve.

However, the -CN functionality would not be attached to the metal coated tip which would reduce conductivity, and the -CN group only serves as a junction group to gold electrodes.[4, 5] Figure **4.2** shows the set-up expected for monolayers of compound **3.8** on Au(111).
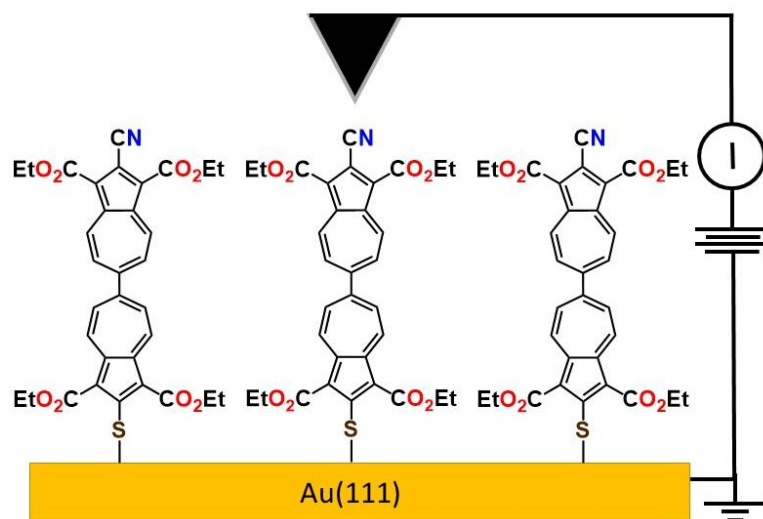
Figure 4.2. Example for the C-AFM set up with SAMs of compound **3.8** on Au(111).

Further investigation of the electronic properties of the new 6,6'-biazulenic π-linker described herein can be accomplished using resonant Auger electron spectroscopy (RAES) using the core hole clock (COC) method as described in a similar study by Prof. Zharnikov in collaboration with the Barybin and Berrie groups that investigates the dynamics of electron transfer in azulene-based SAMs. In their investigation of 6-cyano-2-mercaptoazulene SAMs on Au(111), they used the nitrile group as a REAS-addressable tail group. They found efficient electron transport to the surface for a strongly conjugated molecular orbital with the adjacent seven-membered ring and a small trace of electron transport for an orbital localized in the nitrile moiety.[6] It would be interesting to characterize SAMs of **3.8** and evaluate their electron transport dynamics, considering the addition of a second azulenic unit, competing dipoles, and the 2-CN connectivity.

Ongoing work in the Barybin group to synthesize a molecular rectifier based on azulenic units and using the same functionalities as compound **3.8** is underway. The Barybin group has proposed a terazulene derivative that would satisfy all of Ratner and Van Dyk's requirements for efficient molecular rectification which include a HOMO aligning anchoring group, a π-decoupling

bridge, and a LUMO aligning anchoring group. The proposed terazulene is shown in fig. **4.3**, and it features 2,1'-3',2'' carbon atom connectivity and 5,5''-dimercapto-6'-cyano substitution pattern. Dual anchoring through the mercapto junctions on Au(111) would provide rigidity to the system, the substitution pattern would allow for alignment of HOMO and LUMO of the terazulenic scaffold to the fermi level of gold, and the even-odd connectivity of the terazulenic motif decouples HOMO and LUMO without the need for an aliphatic decoupling bridge. Hopefully, the work described herein will complement future molecular rectification concepts by comparing electronic behaviors of bi- and terazulenes assembled with different connectivities.
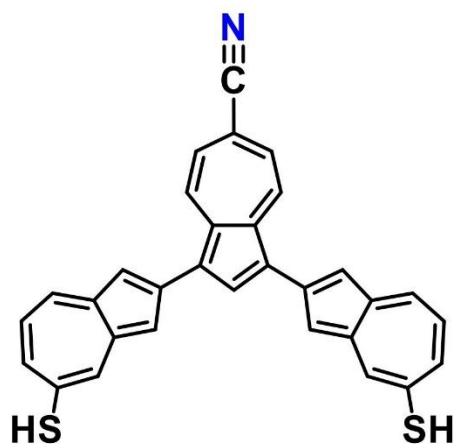
Figure 4.3. Proposed terazulenic derivative featuring 2,1'-3',2'' carbon atom connectivity of the azulenic components between the mercapto and cyano functionalities.

IV.2 References

1. 	Maher, T. R.; Spaeth, A. D.; Neal, B. M.; Berrie, C. L.; Thompson, W. H.; Day, V. W.; Barybin, M. V., Linear 6,6′-Biazulenyl Framework Featuring Isocyanide Termini: Synthesis, Structure, Redox Behavior, Complexation, and Self-Assembly on Au(111). *Journal of the American Chemical Society* **2010,** *132* (45), 15924-15926.
2. 	Holler, J. S., D.; Crouch, S., *Principles of Instrumental Analysis*. 6 ed.; Cengage Learning: 2005.
3. 	Lanza, M., *Conductive Atomic Force Microscopy: Applications in Nanomaterials*. Wiley: 2017.
4. 	Dobler, C.; Tönshoff, C.; Bettinger, H. F.; Chassé, T.; Casu, M. B., Cyano-Functional Group as an Anchoring Tool for Organic Small Molecules on Gold. *The Journal of Physical Chemistry C* **2017,** *121* (25), 13660-13665.
5. 	Holze, R., Competition of anchoring groups in adsorption on gold electrodes—a comparative spectroelectrochemical study of 4-mercaptobenzonitrile and aromatic nitriles. *Journal of Solid State Electrochemistry* **2013,** *17* (7), 1869-1879.
6. 	Wächter, T.; Scheetz, K. J.; Spaeth, A. D.; Barybin, M. V.; Zharnikov, M., Dynamics of Electron Transfer in Azulene-Based Self-Assembled Monolayers. *The Journal of Physical Chemistry C* **2017,** *121* (25), 13777-13785.

Appendix

Table S1. Crystal and Refinement Data for 2-Chloro-1,1',3,3'-tetraethoxycarbonyl-2'-(ethyl-3-thiopropionyl)-6,6'-biazulene (**3.6**).

	3.6 (q72k_0m)
Empirical formula	$C_{36.57}H_{35.63}ClO_{10}S$
Formula weight	702.63
Temperature	200 K
Wavelength	0.71073 Å
Crystal system	Triclinic
Space group	P-1
a	14.506(3) Å
b	17.756(3) Å
c	22.246(6) Å
a	87°
β	82°
γ	67°
Volume	5237(2) $Å^3$
Z	6
Density (calculated)	1.340 g/cm^3
Absorption coefficient	2.012 mm^{-1}
F(000)	2208.00
Crystal size	$0.12 \times 0.12 \times 0.015$ mm^3
Theta range	5.396 to 118.752°
Index ranges	$-14h \leq 15, -19 \leq k \leq 19, -24 \leq l \leq 24$
Reflections collected	41543
Independent reflections	14476 $[R_{int} = 0.1251, R_{sigma} = 0.1645]$
Completeness/θ_{max}	94.9%/59.38°
Absorption correction	Multi-scan
Max./Min. Transmission	0.752 and 0.475
Refinement method	Full-matrix least-squares on F^2
Data/restraints/parameters	14476/1/1298
Goodness-of-fit on F^2	1.149
Final R indices [I>2σ(I)]	$R_1 = 0.1269, wR_2 = 0.3168$
R indices (all data)	$R_1 = 0.1947, wR_2 = 0.3832$
Largest diff. peak & hole	1.17 and -0.53 $e.Å^{-3}$

Table S2. Atomic Coordinates and Equivalent Isotropic Displacement Parameters ($Å2×103$) for **3.6**. U(eq) is defined as one third of the trace of the orthogonalized U_{IJ} tensor.

Atom	x	y	z	U(eq)
Cl1	6832.0(18)	4311.3(14)	6374.3(11)	64.1(6)
C32	5062(9)	-518(6)	841(5)	76(3)
S1	3248(2)	1944.2(15)	792.7(12)	70.2(8)
C28	3673(11)	39(6)	2944(7)	101(5)
O4	8061(5)	4248(5)	4461(3)	78(2)
O10	3778(6)	4225(4)	1022(3)	67.9(18)
O3	7763(6)	4998(4)	5287(4)	78(2)
O5	2685(6)	1093(4)	2095(4)	75(2)
O1	4025(6)	3794(5)	6261(3)	82(2)
C22	4437(12)	3934(10)	7350(5)	102(4)
O6	4005(7)	691(4)	2611(4)	96(3)
C34	6290(11)	-1871(7)	944(7)	95(4)
O8	5922(6)	-976(4)	1043(4)	86(2)
C6	6309(6)	4203(5)	5758(4)	47(2)
C4	5357(6)	3887(4)	5162(4)	42.0(18)
C8	6148(5)	4075(4)	4755(4)	40.9(19)
C2	4533(6)	3457(5)	4382(4)	47(2)
C31	4784(9)	376(6)	929(6)	76(3)
O9	3260(7)	3486(4)	481(4)	97(3)
C14	4059(6)	2309(5)	2370(4)	49(2)
C23	4798(12)	4188(11)	7869(6)	114(5)
C33	4155(12)	-675(8)	2540(7)	110(5)
C10	5782(6)	3881(5)	3722(4)	50(2)
C7	6718(6)	4273(4)	5164(4)	49(2)

Atom	x	y	z	U(eq)
C5	5474(6)	3971(4)	5774(4)	44.4(19)
C9	6251(6)	4110(4)	4138(4)	47(2)
C1	5025(6)	3549(5)	3824(4)	46.6(19)
C18	4026(7)	3050(5)	2019(4)	51(2)
O7	4583(7)	-812(4)	586(5)	104(3)
C38	3956(11)	5468(7)	751(6)	90(4)
C37	3653(10)	4813(6)	540(5)	80(3)
C30	3679(9)	843(6)	829(5)	72(3)
C15	3722(7)	1854(5)	1996(4)	54(2)
C20	4542(6)	3787(4)	2781(4)	50(2)
C12	4675(6)	2504(4)	3333(4)	46.4(19)
C3	4667(6)	3604(4)	4954(4)	45.4(19)
C17	3703(7)	3012(5)	1456(4)	56(2)
C24	7551(7)	4541(6)	4985(5)	60(2)
C25	8866(11)	4535(8)	4256(6)	97(2)
C16	3548(7)	2268(5)	1442(4)	53(2)
C13	4381(6)	2083(5)	2929(4)	50(2)
C35	5854(12)	-2247(7)	1450(6)	98(4)
C11	4734(6)	3262(5)	3273(4)	46.8(19)
C27	3425(8)	1175(5)	2214(4)	61(3)
C19	4243(7)	3688(5)	2225(4)	52(2)
C21	4797(8)	3891(5)	6282(4)	58(2)
C26	9186(16)	4377(12)	3640(7)	156(4)
O2	5065(7)	3993(6)	6821(4)	91.6(17)
C36	3554(8)	3563(5)	940(5)	61(2)

Atom	x	y	z	U(eq)
S1*	9379.0(19)	8955.7(14)	6679.9(12)	64.0(7)
C38*	10212(8)	7279(5)	4656(7)	81(4)
C33*	9611(13)	9020(8)	7846(6)	108(5)
Cl1*	6742(3)	13908.4(17)	784.7(14)	90.8(10)
O4*	6268(5)	12498(4)	710(3)	66.3(18)
O10*	9720(5)	8145(3)	4774(4)	67.5(19)
O2*	7888(6)	14611(4)	1359(3)	73(2)
O9*	9874(5)	7855(4)	5744(4)	74(2)
C25*	5959(10)	12034(6)	314(5)	77(3)
O3*	6226(6)	11632(4)	1450(3)	75(2)
O1*	7949(7)	14545(4)	2351(4)	92(3)
C37*	9616(7)	8358(5)	5348(5)	55(2)
C18*	8836(6)	9894(4)	5053(4)	43.7(19)
C11*	8112(6)	11318(5)	4053(4)	49(2)
C14*	8513(6)	10664(5)	5394(4)	48(2)
O8*	10386(7)	8838(5)	8719(4)	91(2)
C19*	8804(6)	9848(5)	4442(5)	52(2)
O7*	10259(13)	9948(8)	8185(7)	187(7)
C26*	5946(14)	12426(9)	-296(6)	119(6)
C36*	11103(11)	8433(10)	9643(7)	112(5)
C17*	9164(6)	9249(5)	5449(4)	51(2)
C15*	8678(6)	10438(5)	6004(4)	53(2)
C10*	7325(6)	11534(5)	3101(4)	55(2)
C6*	7044(7)	13368(6)	1426(4)	59(2)
C1*	7865(6)	11791(5)	3482(4)	50(2)

Atom	x	y	z	U(eq)
C8*	7155(6)	12433(5)	2196(4)	49(2)
C20*	8489(6)	10459(5)	3998(5)	52(2)
C4*	7589(6)	13010(4)	2354(4)	45.1(19)
C13*	8141(6)	11456(5)	5177(4)	50(2)
C40*	10132(10)	9331(7)	8243(6)	86(4)
C39*	10214(10)	7148(7)	3964(7)	99(4)
C7*	6837(6)	12666(5)	1605(5)	53(2)
C32*	9259(11)	9602(7)	7316(6)	88(4)
C12*	7984(6)	11735(5)	4589(4)	52(2)
C23*	8054(17)	15643(13)	709(9)	156(4)
C9*	7035(7)	11808(5)	2550(4)	58(2)
C35*	10917(12)	9064(10)	9152(7)	114(5)
C24*	6404(7)	12212(5)	1262(4)	55(2)
C16*	9079(6)	9568(5)	6045(5)	58(3)
C3*	8060(6)	12966(5)	2880(4)	52(2)
C2*	8189(7)	12434(5)	3359(4)	55(2)
C21*	7784(8)	14292(6)	1897(5)	63(3)
C5*	7495(7)	13582(5)	1894(4)	56(2)
C27*	8518(8)	11058(6)	6470(5)	63(3)
C22*	8103(12)	15341(8)	1335(6)	97(2)
C31*	7310(20)	12228(15)	7079(12)	97(2)
C30*	7240(30)	11970(20)	7760(14)	156(4)
O6*	7610(7)	11490(6)	6662(5)	103(3)
C28*	9250(40)	11530(20)	7120(20)	97(2)
O5*	9263(7)	11153(6)	6639(4)	91.6(17)

Atom	x	y	z	U(eq)
C29*	10290(40)	11490(30)	7240(20)	97(2)
S1'	6422.6(19)	9778.1(13)	3086.0(11)	59.5(6)
Cl1'	9176(2)	4934.6(17)	9013.0(13)	81.2(8)
O6'	6051(4)	10577(3)	4996(3)	52.2(14)
O5'	5651(5)	10863(3)	4057(3)	68.7(18)
O9'	6492(6)	7818(4)	2963(3)	72.6(19)
C24'	8265(8)	4401(6)	7881(5)	68(3)
O10'	8021(6)	7088(4)	3239(3)	73.7(19)
O2'	9508(7)	6467(5)	9039(4)	91(3)
C27'	6035(6)	10359(4)	4431(4)	49(2)
O4'	8696(7)	3853(4)	8275(4)	96(3)
C13'	6842(6)	8876(4)	5352(4)	46(2)
C15'	6518(6)	9484(4)	4323(4)	44.3(19)
C17'	7066(6)	8295(5)	3762(4)	47(2)
C1'	7964(6)	6942(4)	6285(4)	46(2)
C14'	6860(6)	8827(4)	4733(4)	45(2)
C10'	7861(6)	6186(4)	6378(4)	49(2)
C18'	7220(6)	8070(4)	4370(4)	42.9(19)
C22'	9868(14)	6981(9)	9376(6)	114(6)
C16'	6666(6)	9155(5)	3730(4)	48(2)
C20'	7810(6)	6981(4)	5181(4)	47(2)
O1'	9832(8)	7084(5)	8218(4)	101(3)
C12'	7196(6)	8266(4)	5778(4)	46.7(19)
O3'	7721(8)	4319(5)	7555(4)	104(3)
C33'	8227(13)	9229(12)	290(7)	127(6)

Atom	x	y	z	U(eq)
C3'	8720(7)	7018(5)	7225(4)	55(2)
C11'	7648(6)	7412(5)	5722(4)	45.3(19)
C21'	9513(8)	6615(6)	8459(5)	69(3)
C30'	7175(9)	9113(5)	2443(5)	68(3)
O7'	8286(9)	8461(7)	1364(6)	136(4)
C31'	7329(9)	9655(6)	1936(5)	74(3)
C19'	7609(7)	7272(5)	4607(4)	53(2)
C32'	7838(10)	9179(9)	1381(6)	87(3)
C36'	8199(12)	6472(7)	2756(7)	115(6)
C2'	8373(7)	7281(5)	6673(4)	56(2)
C25'	8593(12)	3070(7)	8254(6)	97(2)
C4'	8738(6)	6334(5)	7565(4)	51(2)
C7'	8521(7)	5135(5)	7876(4)	54(2)
C9'	8032(6)	5654(5)	6858(4)	50(2)
O8'	7757(7)	9654(6)	878(4)	102(3)
C8'	8387(6)	5707(5)	7403(4)	52(2)
C34'	8085(14)	9807(12)	-201(8)	134(6)
C23'	9680(20)	6821(14)	9980(9)	207(13)
C6'	8914(7)	5415(6)	8336(5)	60(2)
C26'	8955(17)	2591(12)	8794(9)	156(4)
C28'	5567(7)	11450(4)	5134(5)	55(2)
C35'	7144(8)	7723(5)	3283(4)	57(2)
C5'	9069(7)	6117(5)	8148(4)	55(2)
C29'	5562(8)	11541(6)	5784(5)	69(3)

Table S3. Bond Lengths for 2-Chloro-1,1',3,3'-tetraethoxycarbonyl-2'-(ethyl-3-thiopropionyl)-6,6'-biazulene.

Atom	Atom	Length/Å		Atom	Atom	Length/Å
Cl1	C6	1.707(8)		C19*	C20*	1.410(12)
C32	O8	1.323(14)		O7*	C40*	1.177(14)
C32	C31	1.494(14)		C36*	C35*	1.497(19)
C32	O7	1.224(13)		C17*	C16*	1.441(14)
S1	C30	1.809(9)		C15*	C16*	1.427(12)
S1	C16	1.747(9)		C15*	C27*	1.482(14)
C28	O6	1.539(13)		C10*	C1*	1.428(13)
C28	C33	1.472(19)		C10*	C9*	1.355(13)
O4	C24	1.306(13)		C6*	C7*	1.418(12)
O4	C25	1.457(14)		C6*	C5*	1.440(13)
O10	C37	1.436(11)		C1*	C2*	1.395(11)
O10	C36	1.362(11)		C8*	C4*	1.472(11)
O3	C24	1.229(12)		C8*	C7*	1.438(13)
O5	C27	1.202(11)		C8*	C9*	1.382(12)
O1	C21	1.203(11)		C4*	C3*	1.415(12)
C22	C23	1.485(18)		C4*	C5*	1.386(12)
C22	O2	1.414(14)		C13*	C12*	1.390(12)
O6	C27	1.337(11)		C7*	C24*	1.486(12)
C34	O8	1.486(13)		C23*	C22*	1.47(2)
C34	C35	1.472(18)		C3*	C2*	1.371(12)
C6	C7	1.393(13)		C21*	C5*	1.476(12)
C6	C5	1.418(12)		C27*	O6*	1.267(13)
C4	C8	1.494(11)		C27*	O5*	1.262(11)
C4	C5	1.416(12)		C31*	C30*	1.56(4)
C4	C3	1.417(11)		C31*	O6*	1.53(3)
C8	C7	1.449(12)		C28*	O5*	1.28(4)
C8	C9	1.361(12)		C28*	C29*	1.55(7)
C2	C1	1.382(12)		S1'	C16'	1.754(8)
C2	C3	1.364(12)		S1'	C30'	1.841(11)
C31	C30	1.537(15)		Cl1'	C6'	1.705(9)
O9	C36	1.191(11)		O6'	C27'	1.339(11)
C14	C18	1.484(11)		O6'	C28'	1.463(9)
C14	C15	1.438(12)		O5'	C27'	1.212(10)
C14	C13	1.373(12)		O9'	C35'	1.216(11)
C10	C9	1.381(12)		C24'	O4'	1.302(11)
C10	C1	1.423(11)		C24'	O3'	1.194(12)

Atom	Atom	Length/Å		Atom	Atom	Length/Å
C7	C24	1.464(13)		C24'	C7'	1.487(12)
C5	C21	1.433(13)		O10'	C36'	1.498(13)
C1	C11	1.518(12)		O10'	C35'	1.331(12)
C18	C17	1.409(13)		O2'	C22'	1.488(13)
C18	C19	1.400(12)		O2'	C21'	1.303(13)
C38	C37	1.509(14)		C27'	C15'	1.454(11)
C15	C16	1.403(12)		O4'	C25'	1.459(12)
C15	C27	1.471(12)		C13'	C14'	1.380(12)
C20	C11	1.386(12)		C13'	C12'	1.390(11)
C20	C19	1.404(12)		C15'	C14'	1.415(11)
C12	C13	1.404(12)		C15'	C16'	1.425(12)
C12	C11	1.380(11)		C17'	C18'	1.413(12)
C17	C16	1.426(11)		C17'	C16'	1.410(11)
C17	C36	1.452(13)		C17'	C35'	1.473(13)
C25	C26	1.393(15)		C1'	C10'	1.409(10)
C21	O2	1.352(12)		C1'	C11'	1.493(11)
S1*	C32*	1.814(12)		C1'	C2'	1.387(12)
S1*	C16*	1.734(9)		C14'	C18'	1.479(11)
C38*	O10*	1.444(11)		C10'	C9'	1.370(12)
C38*	C39*	1.569(19)		C18'	C19'	1.411(11)
C33*	C40*	1.486(16)		C22'	C23'	1.37(2)
C33*	C32*	1.532(15)		C20'	C11'	1.403(12)
Cl1*	C6*	1.687(9)		C20'	C19'	1.378(12)
O4*	C25*	1.456(11)		O1'	C21'	1.174(12)
O4*	C24*	1.315(11)		C12'	C11'	1.405(11)
O10*	C37*	1.323(12)		C33'	O8'	1.487(17)
O2*	C21*	1.312(12)		C33'	C34'	1.44(2)
O2*	C22*	1.444(12)		C3'	C2'	1.380(13)
O9*	C37*	1.210(10)		C3'	C4'	1.392(11)
C25*	C26*	1.492(16)		C21'	C5'	1.516(12)
O3*	C24*	1.198(11)		C30'	C31'	1.494(14)
O1*	C21*	1.215(12)		O7'	C32'	1.186(15)
C37*	C17*	1.477(12)		C31'	C32'	1.472(17)
C18*	C14*	1.475(12)		C32'	O8'	1.356(15)
C18*	C19*	1.375(13)		C25'	C26'	1.47(2)
C18*	C17*	1.379(11)		C4'	C8'	1.468(11)
C11*	C1*	1.492(12)		C4'	C5'	1.425(12)
C11*	C20*	1.413(12)		C7'	C8'	1.403(12)

Atom	Atom	Length/Å		Atom	Atom	Length/Å
C11*	C12*	1.390(13)		C7'	C6'	1.430(13)
C14*	C15*	1.421(12)		C9'	C8'	1.401(12)
C14*	C13*	1.385(11)		C6'	C5'	1.384(12)
O8*	C40*	1.337(13)		C28'	C29'	1.463(14)
O8*	C35*	1.469(15)				

Table S4. Bond Angles for 2-Chloro-1,1',3,3'-tetraethoxycarbonyl-2'-(ethyl-3-thiopropionyl)-6,6'-biazulene.

Atom	Atom	Atom	Angle/°		Atom	Atom	Atom	Angle/°
O8	C32	C31	113.1(10)		C9*	C8*	C7*	126.1(8)
O7	C32	O8	121.9(10)		C19*	C20*	C11*	129.9(9)
O7	C32	C31	124.9(10)		C3*	C4*	C8*	125.4(7)
C16	S1	C30	107.4(4)		C5*	C4*	C8*	108.8(7)
C33	C28	O6	103.3(12)		C5*	C4*	C3*	125.9(7)
C24	O4	C25	114.6(8)		C14*	C13*	C12*	129.6(9)
C36	O10	C37	117.9(7)		O8*	C40*	C33*	110.5(9)
O2	C22	C23	107.1(10)		O7*	C40*	C33*	126.7(11)
C27	O6	C28	118.0(8)		O7*	C40*	O8*	122.6(12)
C35	C34	O8	109.8(11)		C6*	C7*	C8*	107.3(7)
C32	O8	C34	117.1(9)		C6*	C7*	C24*	128.6(8)
C7	C6	Cl1	122.7(7)		C8*	C7*	C24*	124.1(7)
C7	C6	C5	111.4(7)		C33*	C32*	S1*	105.7(8)
C5	C6	Cl1	125.7(7)		C13*	C12*	C11*	131.3(8)
C5	C4	C8	109.2(6)		C10*	C9*	C8*	130.3(8)
C5	C4	C3	126.6(7)		O8*	C35*	C36*	106.7(12)
C3	C4	C8	124.0(8)		O4*	C24*	C7*	112.4(7)
C7	C8	C4	104.5(7)		O3*	C24*	O4*	122.6(8)
C9	C8	C4	127.1(7)		O3*	C24*	C7*	124.9(9)
C9	C8	C7	128.2(7)		C17*	C16*	S1*	123.3(7)
C3	C2	C1	130.8(8)		C15*	C16*	S1*	129.0(8)
C32	C31	C30	109.5(8)		C15*	C16*	C17*	107.7(8)
C15	C14	C18	106.1(7)		C2*	C3*	C4*	130.5(8)
C13	C14	C18	127.2(7)		C3*	C2*	C1*	130.2(8)
C13	C14	C15	126.6(7)		O2*	C21*	C5*	114.0(8)
C9	C10	C1	129.4(8)		O1*	C21*	O2*	122.5(8)
C6	C7	C8	108.5(7)		O1*	C21*	C5*	123.4(8)
C6	C7	C24	125.7(8)		C6*	C5*	C21*	126.6(8)
C8	C7	C24	125.7(8)		C4*	C5*	C6*	107.8(7)
C6	C5	C21	129.6(8)		C4*	C5*	C21*	125.6(8)
C4	C5	C6	106.4(7)		O6*	C27*	C15*	116.3(8)
C4	C5	C21	123.8(7)		O5*	C27*	C15*	120.0(10)
C8	C9	C10	131.0(7)		O2*	C22*	C23*	107.1(11)
C2	C1	C10	125.7(8)		O6*	C31*	C30*	111.2(19)
C2	C1	C11	116.8(7)		C27*	O6*	C31*	122.8(13)
C10	C1	C11	117.5(8)		O5*	C28*	C29*	115(4)
C17	C18	C14	108.1(7)		C27*	O5*	C28*	126(2)
C19	C18	C14	125.5(8)		C16'	S1'	C30'	105.3(4)
C19	C18	C17	126.4(7)		C27'	O6'	C28'	116.2(6)
O10	C37	C38	106.4(9)		O4'	C24'	C7'	113.4(8)
C31	C30	S1	116.5(7)		O3'	C24'	O4'	123.2(8)

Atom	Atom	Atom	Angle/°		Atom	Atom	Atom	Angle/°
C14	C15	C27	124.2(8)		O3'	C24'	C7'	123.4(8)
C16	C15	C14	108.1(7)		C35'	O10'	C36'	116.8(9)
C16	C15	C27	126.6(8)		C21'	O2'	C22'	114.7(9)
C11	C20	C19	129.4(7)		O6'	C27'	C15'	113.8(7)
C11	C12	C13	129.4(8)		O5'	C27'	O6'	121.3(7)
C2	C3	C4	131.3(8)		O5'	C27'	C15'	124.9(9)
C18	C17	C16	107.5(7)		C24'	O4'	C25'	116.8(8)
C18	C17	C36	131.3(8)		C14'	C13'	C12'	130.5(7)
C16	C17	C36	121.1(8)		C14'	C15'	C27'	130.5(8)
O4	C24	C7	113.3(8)		C14'	C15'	C16'	108.3(7)
O3	C24	O4	122.2(9)		C16'	C15'	C27'	121.2(7)
O3	C24	C7	124.5(10)		C18'	C17'	C35'	124.5(7)
C26	C25	O4	110.6(11)		C16'	C17'	C18'	108.0(7)
C15	C16	S1	127.8(6)		C16'	C17'	C35'	126.7(8)
C15	C16	C17	110.1(8)		C10'	C1'	C11'	118.8(7)
C17	C16	S1	122.0(7)		C2'	C1'	C10'	124.8(8)
C14	C13	C12	130.2(7)		C2'	C1'	C11'	116.4(6)
C20	C11	C1	117.3(7)		C13'	C14'	C15'	127.2(7)
C12	C11	C1	114.9(7)		C13'	C14'	C18'	126.3(7)
C12	C11	C20	127.8(8)		C15'	C14'	C18'	106.5(8)
O5	C27	O6	122.2(8)		C9'	C10'	C1'	131.4(8)
O5	C27	C15	124.1(8)		C17'	C18'	C14'	107.8(6)
O6	C27	C15	113.4(8)		C19'	C18'	C17'	127.2(8)
C18	C19	C20	130.2(8)		C19'	C18'	C14'	124.9(8)
O1	C21	C5	126.4(9)		C23'	C22'	O2'	106.3(12)
O1	C21	O2	120.3(9)		C15'	C16'	S1'	122.1(6)
O2	C21	C5	113.1(8)		C17'	C16'	S1'	128.5(7)
C21	O2	C22	117.4(9)		C17'	C16'	C15'	109.4(7)
O10	C36	C17	113.2(8)		C19'	C20'	C11'	129.6(7)
O9	C36	O10	120.1(8)		C13'	C12'	C11'	131.5(8)
O9	C36	C17	126.7(9)		C34'	C33'	O8'	110.6(15)
C16*	S1*	C32*	108.4(5)		C2'	C3'	C4'	129.8(7)
O10*	C38*	C39*	107.3(9)		C20'	C11'	C1'	118.7(7)
C40*	C33*	C32*	111.4(9)		C20'	C11'	C12'	124.6(7)
C24*	O4*	C25*	116.5(7)		C12'	C11'	C1'	116.7(7)
C37*	O10*	C38*	115.0(8)		O2'	C21'	C5'	112.2(8)
C21*	O2*	C22*	116.9(8)		O1'	C21'	O2'	122.3(9)
O4*	C25*	C26*	106.8(8)		O1'	C21'	C5'	125.4(10)
O10*	C37*	C17*	113.8(7)		C31'	C30'	S1'	107.2(7)
O9*	C37*	O10*	121.8(9)		C32'	C31'	C30'	110.9(9)
O9*	C37*	C17*	124.4(10)		C20'	C19'	C18'	132.3(8)
C19*	C18*	C14*	124.5(6)		O7'	C32'	C31'	124.9(12)
C19*	C18*	C17*	126.8(8)		O7'	C32'	O8'	122.6(14)
C17*	C18*	C14*	108.7(8)		O8'	C32'	C31'	112.5(11)

Atom	Atom	Atom	Angle/°		Atom	Atom	Atom	Angle/°
C20*	C11*	C1*	116.1(8)		C3'	C2'	C1'	131.2(7)
C12*	C11*	C1*	119.1(7)		O4'	C25'	C26'	109.0(11)
C12*	C11*	C20*	124.7(8)		C3'	C4'	C8'	126.6(8)
C15*	C14*	C18*	106.2(6)		C3'	C4'	C5'	126.9(8)
C13*	C14*	C18*	128.3(8)		C5'	C4'	C8'	106.5(7)
C13*	C14*	C15*	125.4(8)		C8'	C7'	C24'	124.7(8)
C40*	O8*	C35*	116.8(10)		C8'	C7'	C6'	106.8(7)
C18*	C19*	C20*	131.6(8)		C6'	C7'	C24'	128.5(8)
C18*	C17*	C37*	131.5(9)		C10'	C9'	C8'	129.3(7)
C18*	C17*	C16*	108.7(7)		C32'	O8'	C33'	116.7(12)
C16*	C17*	C37*	119.6(8)		C7'	C8'	C4'	108.2(7)
C14*	C15*	C16*	108.7(8)		C9'	C8'	C4'	126.5(7)
C14*	C15*	C27*	121.3(7)		C9'	C8'	C7'	125.2(7)
C16*	C15*	C27*	129.8(8)		C7'	C6'	Cl1'	124.4(7)
C9*	C10*	C1*	130.6(8)		C5'	C6'	Cl1'	125.2(8)
C7*	C6*	Cl1*	125.5(7)		C5'	C6'	C7'	110.3(8)
C7*	C6*	C5*	109.4(8)		C29'	C28'	O6'	107.1(7)
C5*	C6*	Cl1*	125.0(7)		O9'	C35'	O10'	123.7(9)
C10*	C1*	C11*	116.5(7)		O9'	C35'	C17'	124.5(9)
C2*	C1*	C11*	118.1(8)		O10'	C35'	C17'	111.8(8)
C2*	C1*	C10*	125.4(8)		C4'	C5'	C21'	121.7(8)
C7*	C8*	C4*	106.7(7)		C6'	C5'	C21'	130.1(8)
C9*	C8*	C4*	127.2(8)		C6'	C5'	C4'	108.1(8)
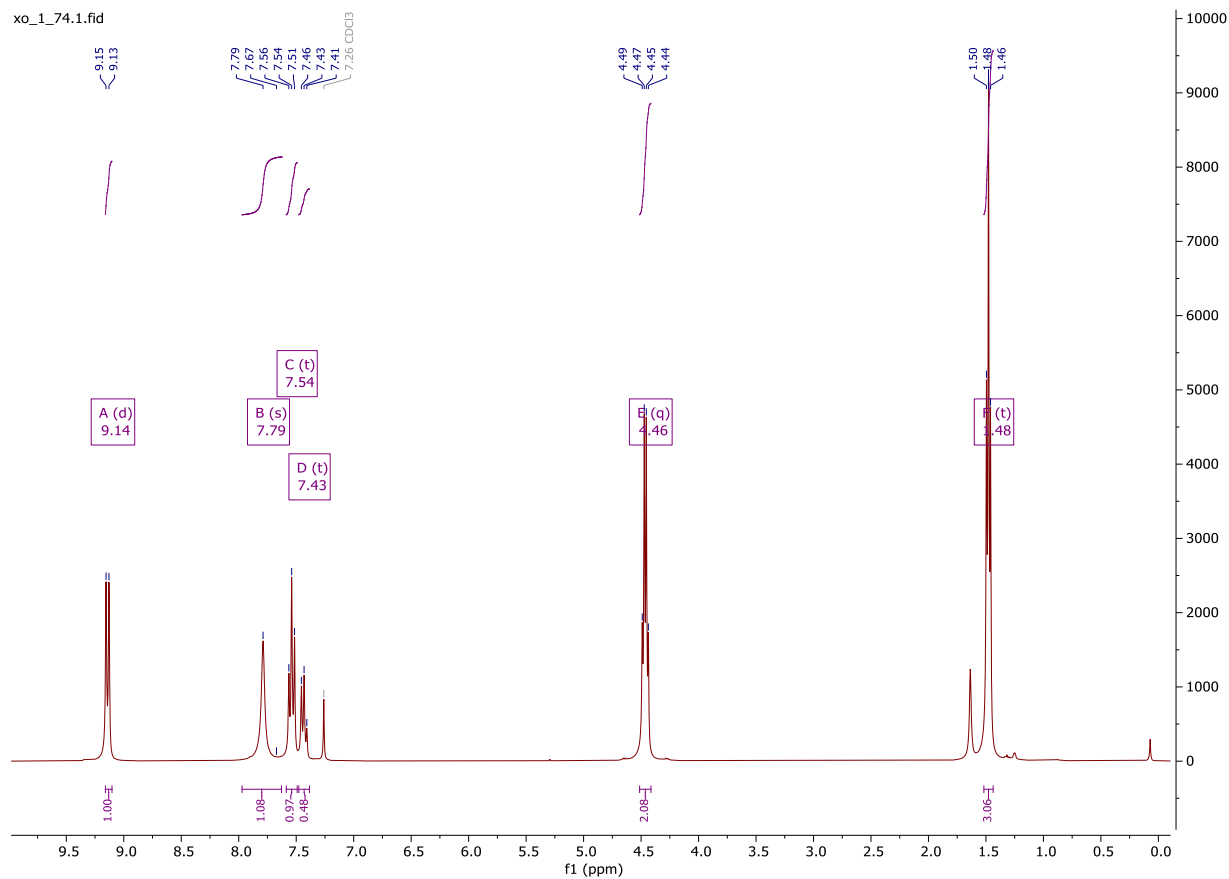
Figure S1. ^{1}HNMR (400 MHz) of 2-amino-1,3-diethoxycarbonylazulene in CDCl$_3$ at 25°C.
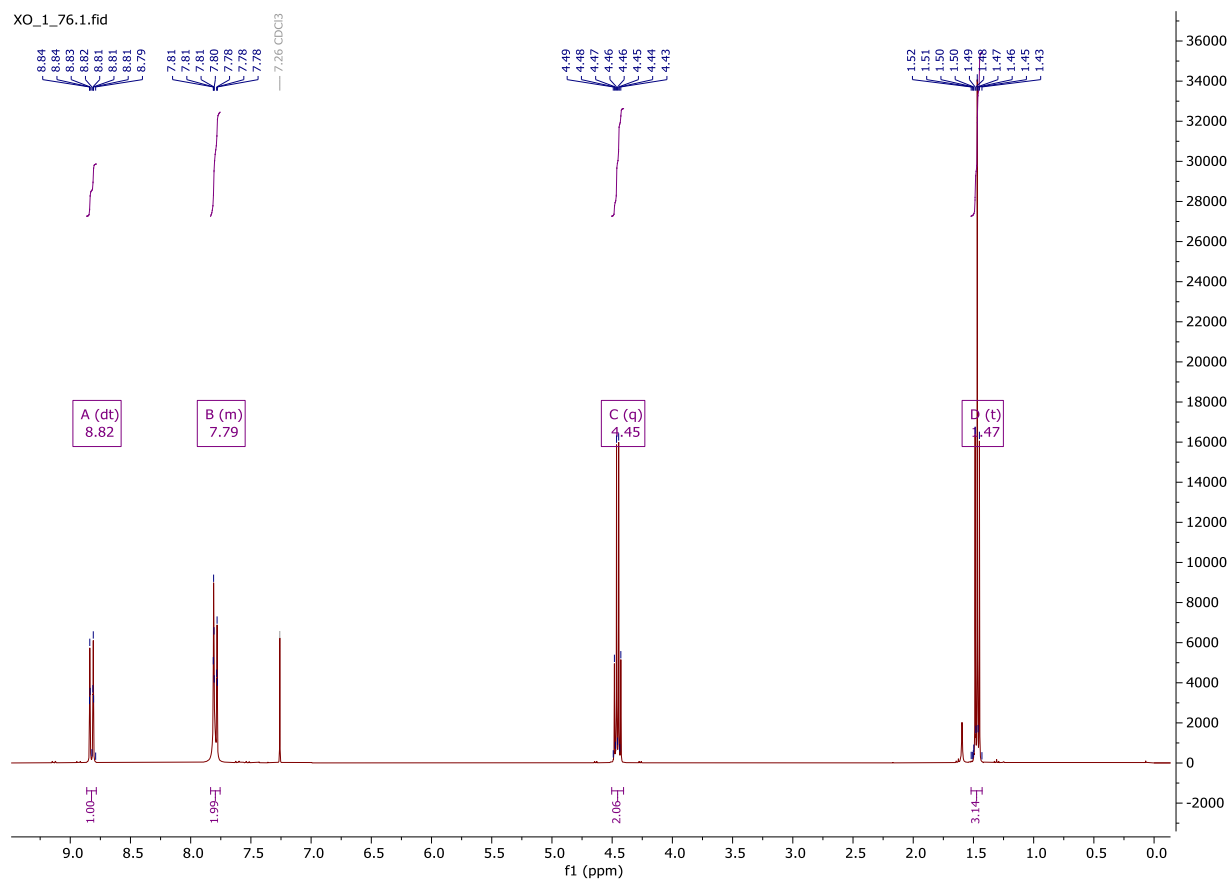
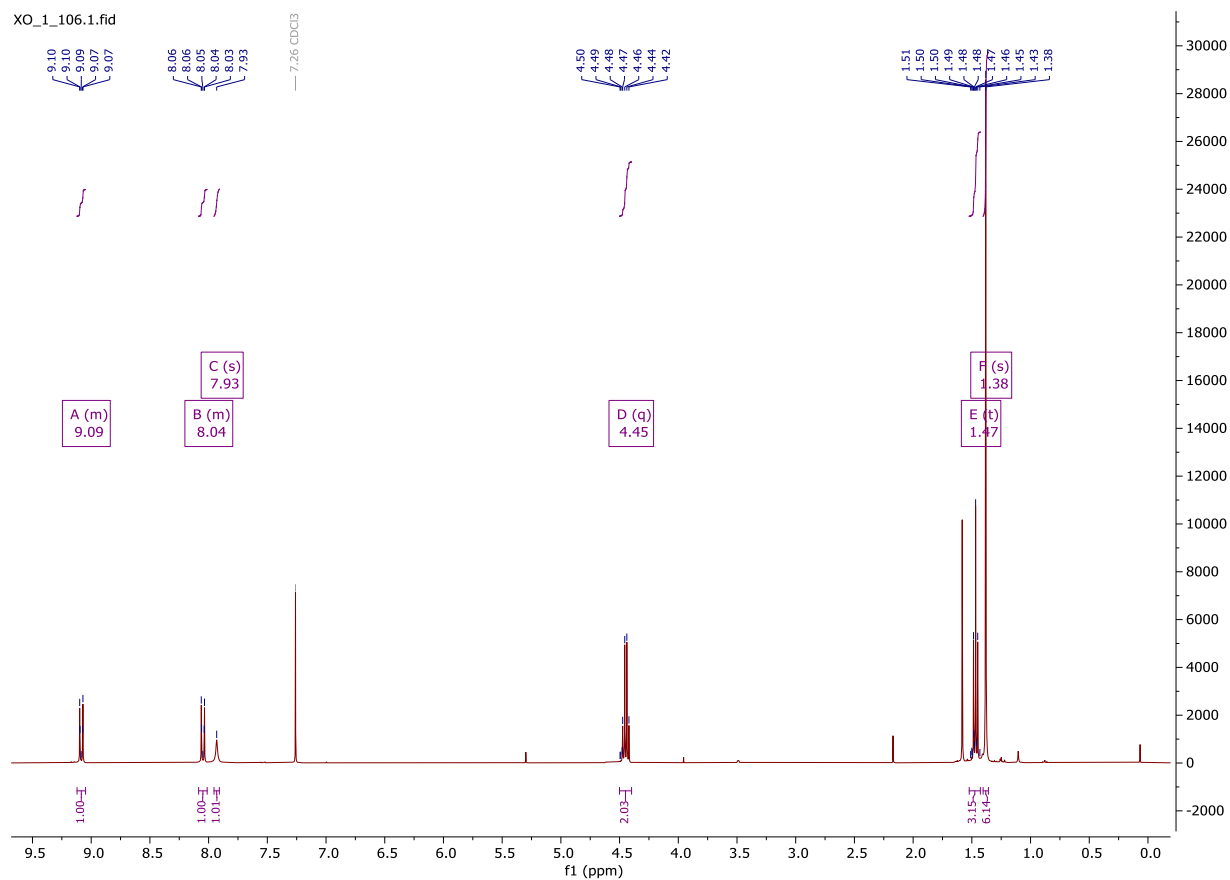**Figure S2.** ^{1}HNMR (400 MHz) of 2-amino-6-bromo-1,3-diethoxycarbonylazulene in CDCl$_3$ at 25°C.

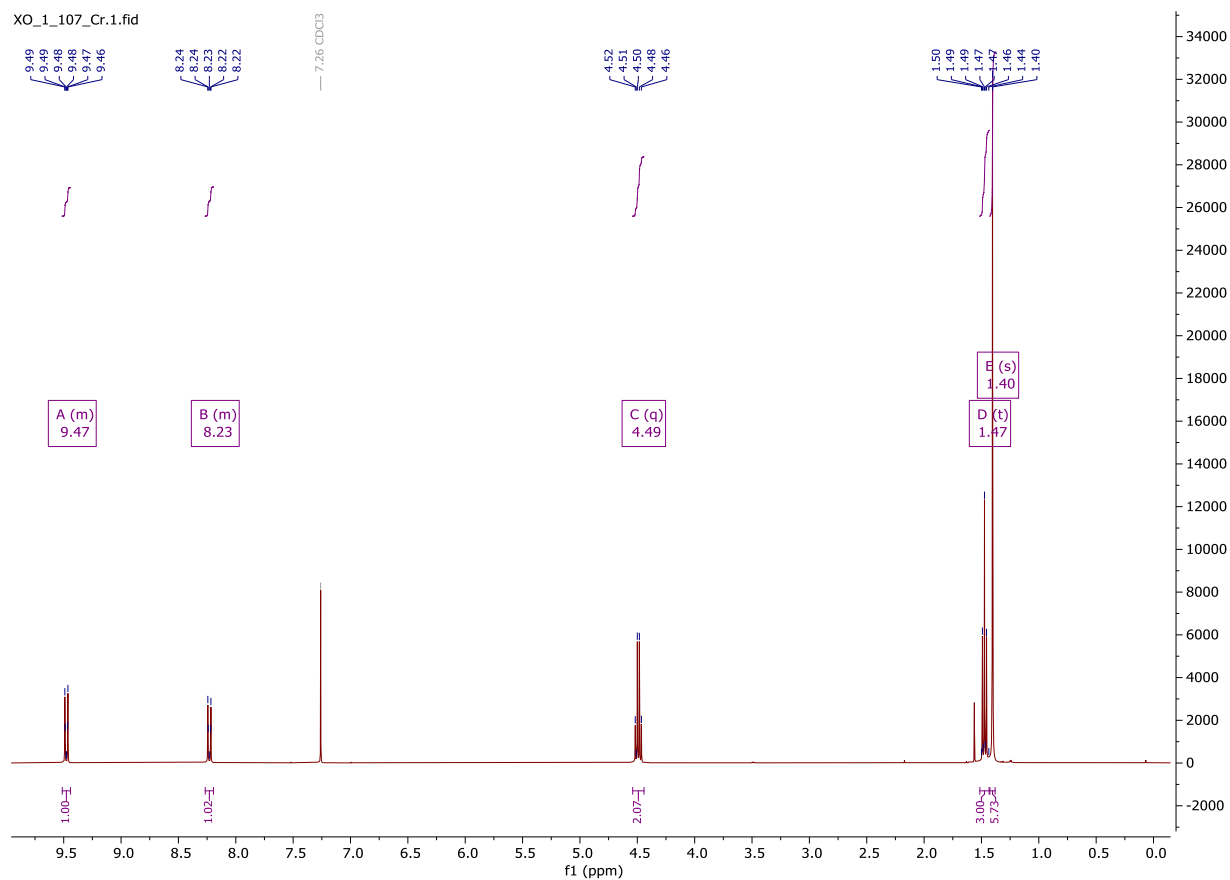**Figure S3.** ^{1}HNMR (400 MHz) of 2-amino-6-pinacolatoboryl-1,3-diethoxycarbonylazulene in CDCl$_3$ at 25°C.

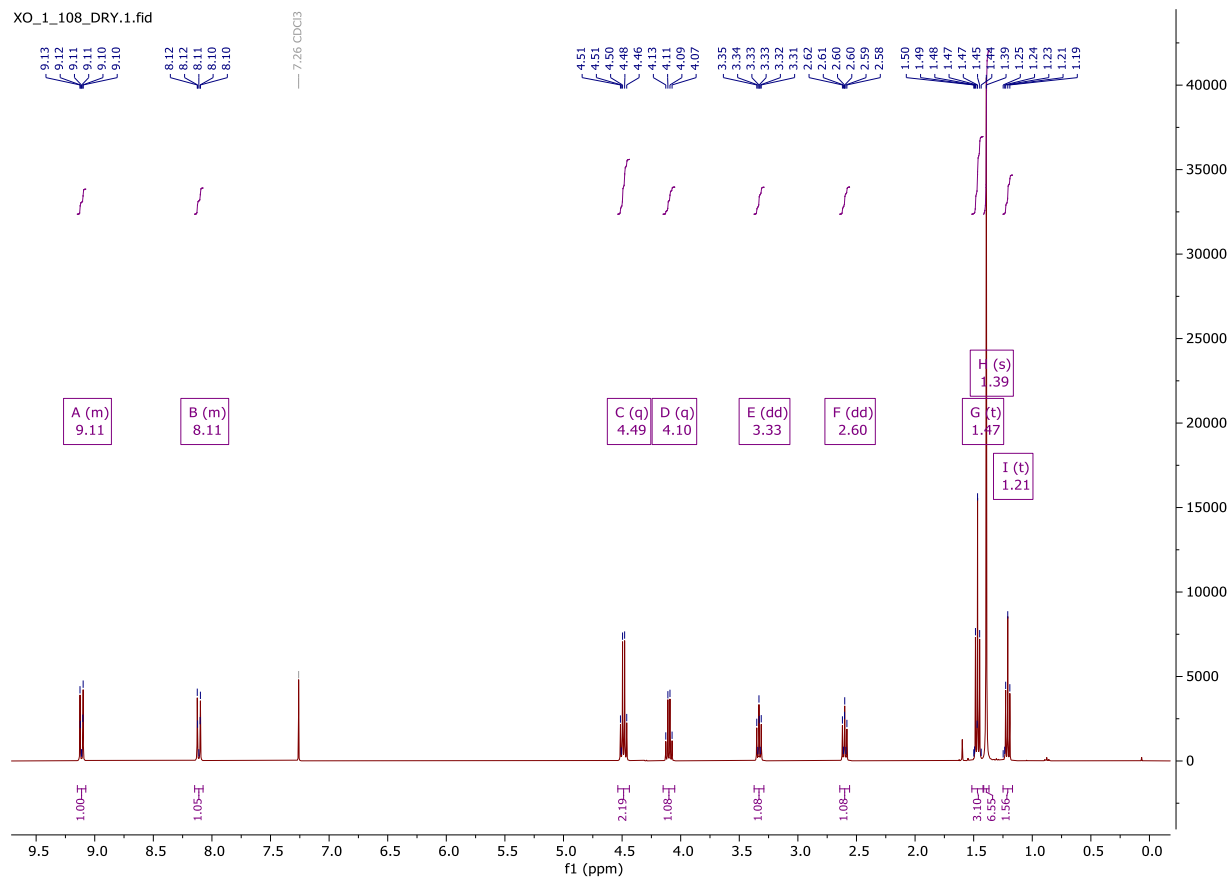**Figure S4.** ^{1}HNMR (400 MHz) of 2-chloro-6-pinacolatoboryl-1,3-diethoxycarbonylazulene in CDCl$_3$ at 25°C.

Figure S5. ^{1}HNMR (400 MHz) of 1,3-diethoxycarbonyl-2-(ethyl-3-mercaptopropionyl)-6-pinacolatoborylazulene in CDCl$_3$ at 25°C.
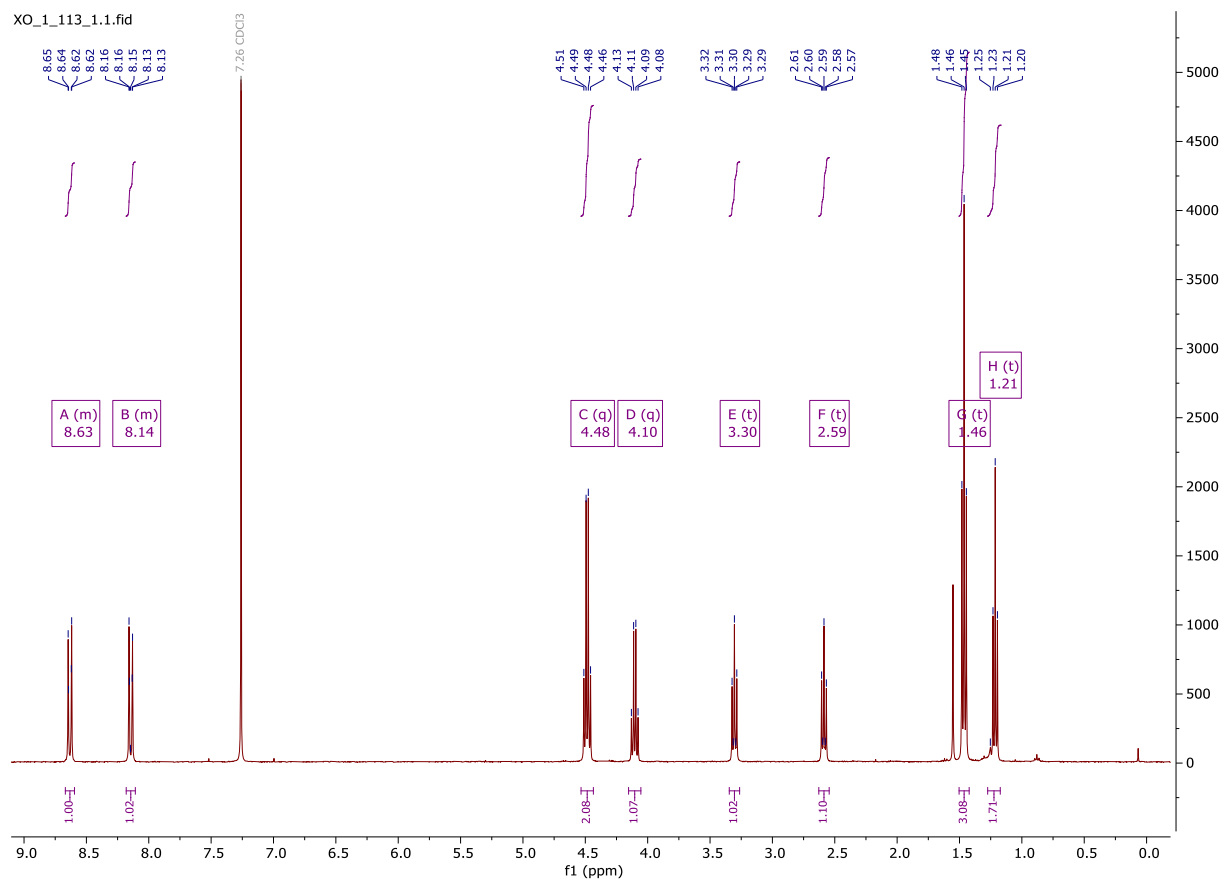
Figure S6. ^{1}HNMR (400 MHz) of 1,3-diethoxycarbonyl-6-iodo-2-(ethyl-3-mercaptopropionyl)azulene in CDCl$_3$ at 25°C.
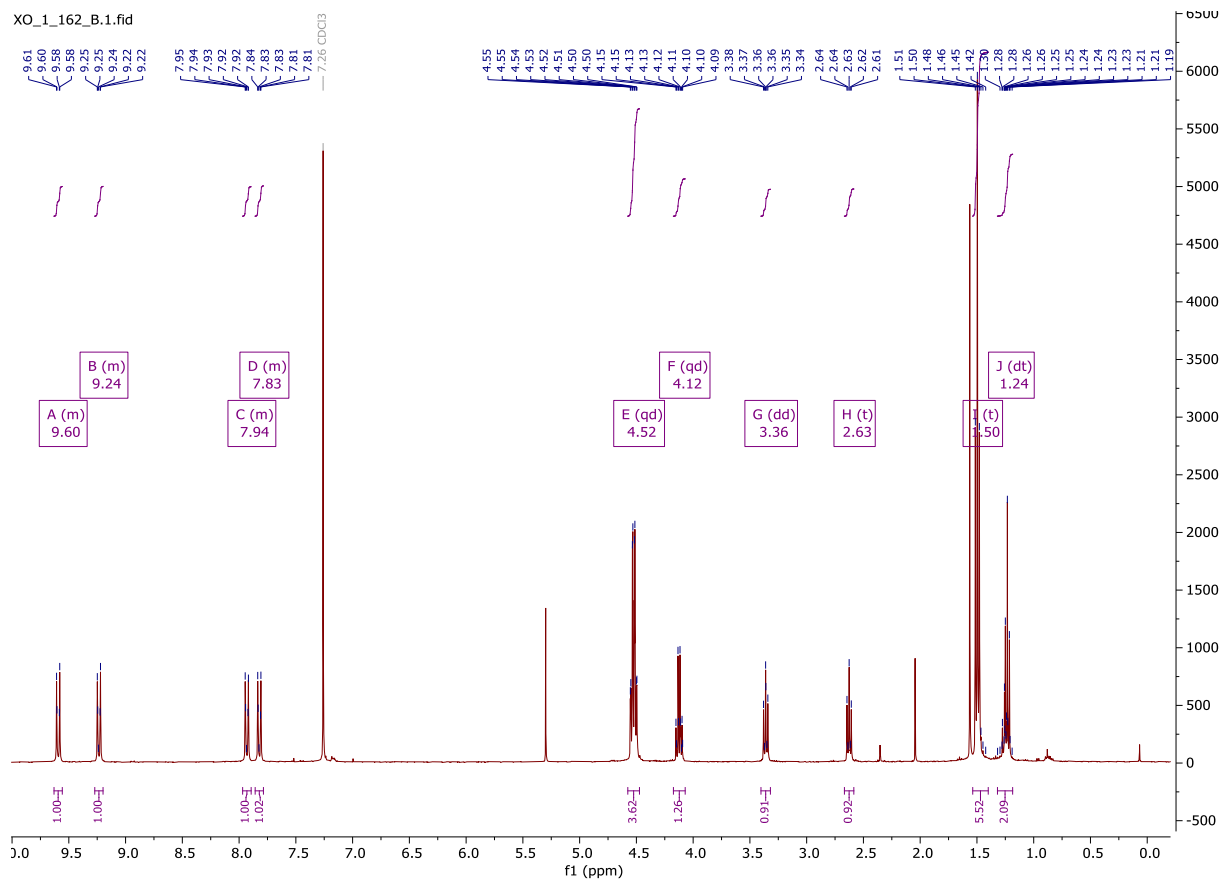
Figure S7. ^{1}HNMR (400 MHz) of 2-chloro-1,1',3,3'-tetraethoxycarbonyl-2'-(ethyl-3-thiopropionyl)-6,6'-biazulene in CDCl$_3$ at 25°C.
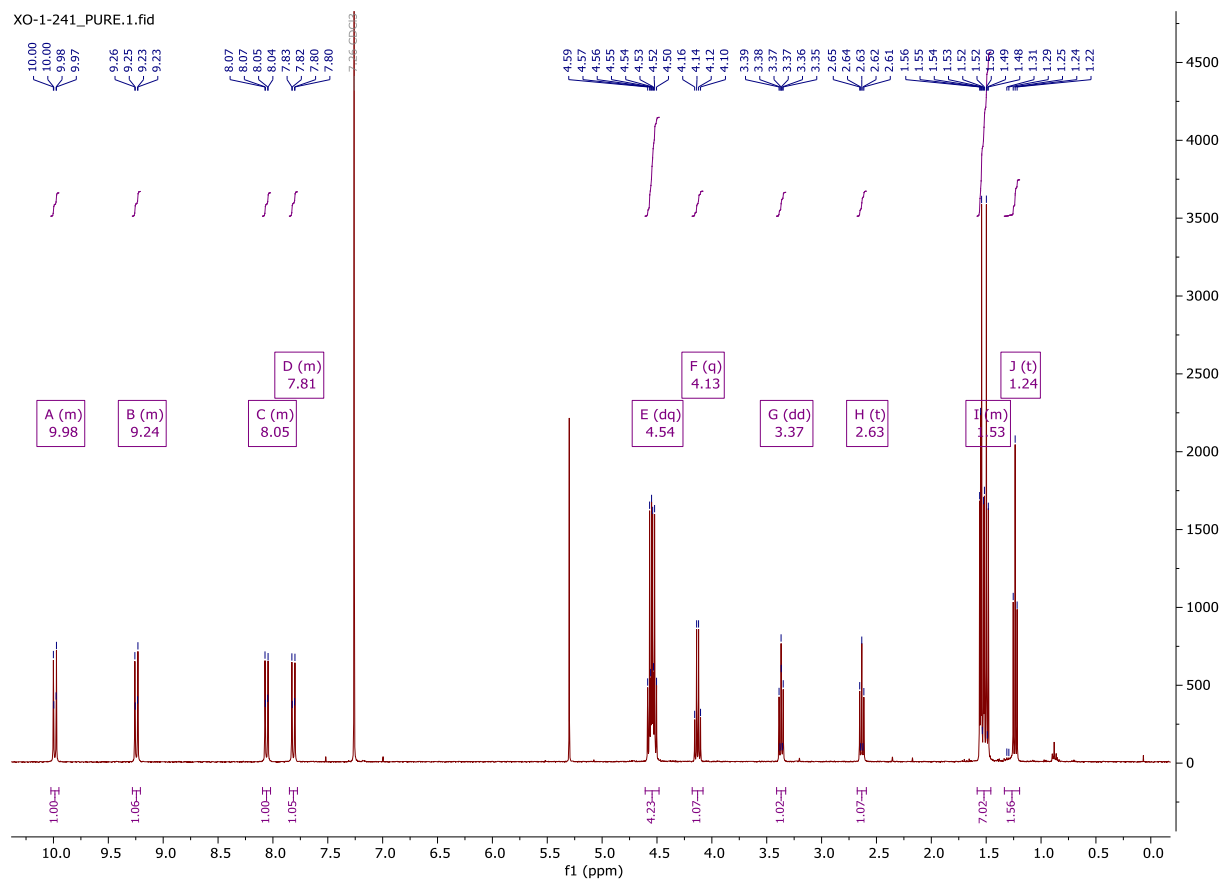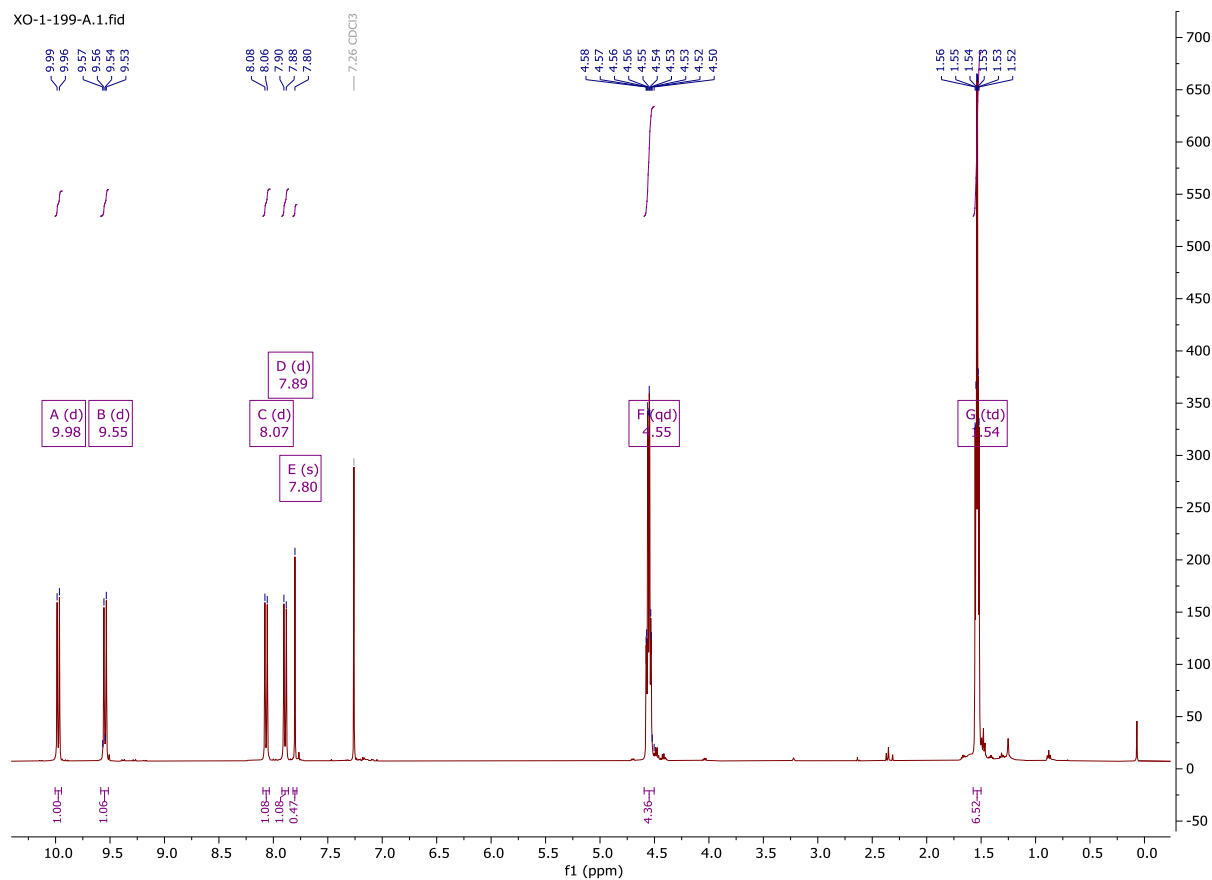
Figure S8. ^{1}HNMR (400 MHz) of 2-cyano-1,1',3,3'-tetraethoxycarbonyl-2'-(ethyl-3-thiopropionyl)-6,6'-biazulene in CDCl$_3$ at 25°C.

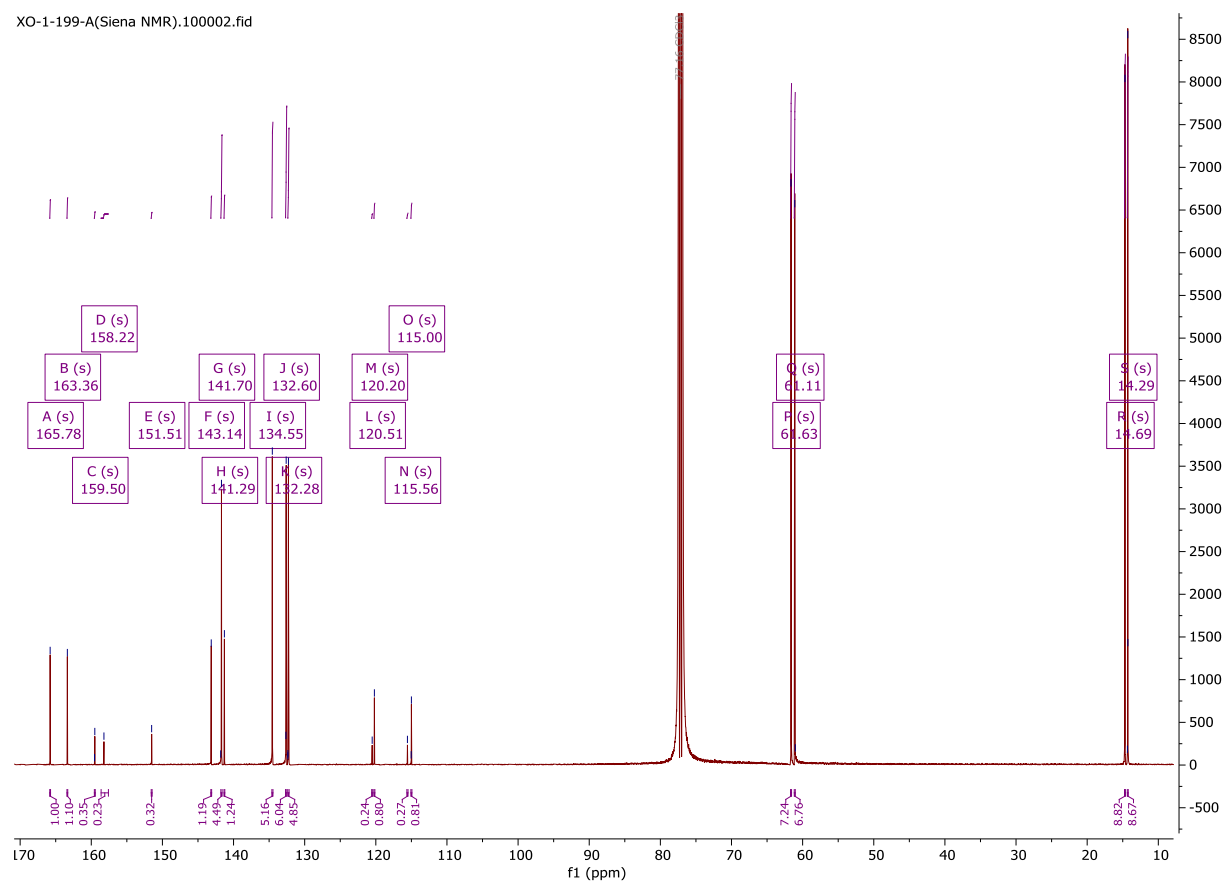**Figure S9.** ^{1}HNMR (500 MHz) of 2-cyano-1,1',3,3'-tetraethoxycarbonyl-2'-mercapto-6,6'-biazulene in CDCl$_3$ at 25°C.

Figure S10. ^{13}CNMR (500 MHz) of 2-cyano-1,1',3,3'-tetraethoxycarbonyl-2'-mercapto-6,6'-biazulene in CDCl$_3$ at 25°C.
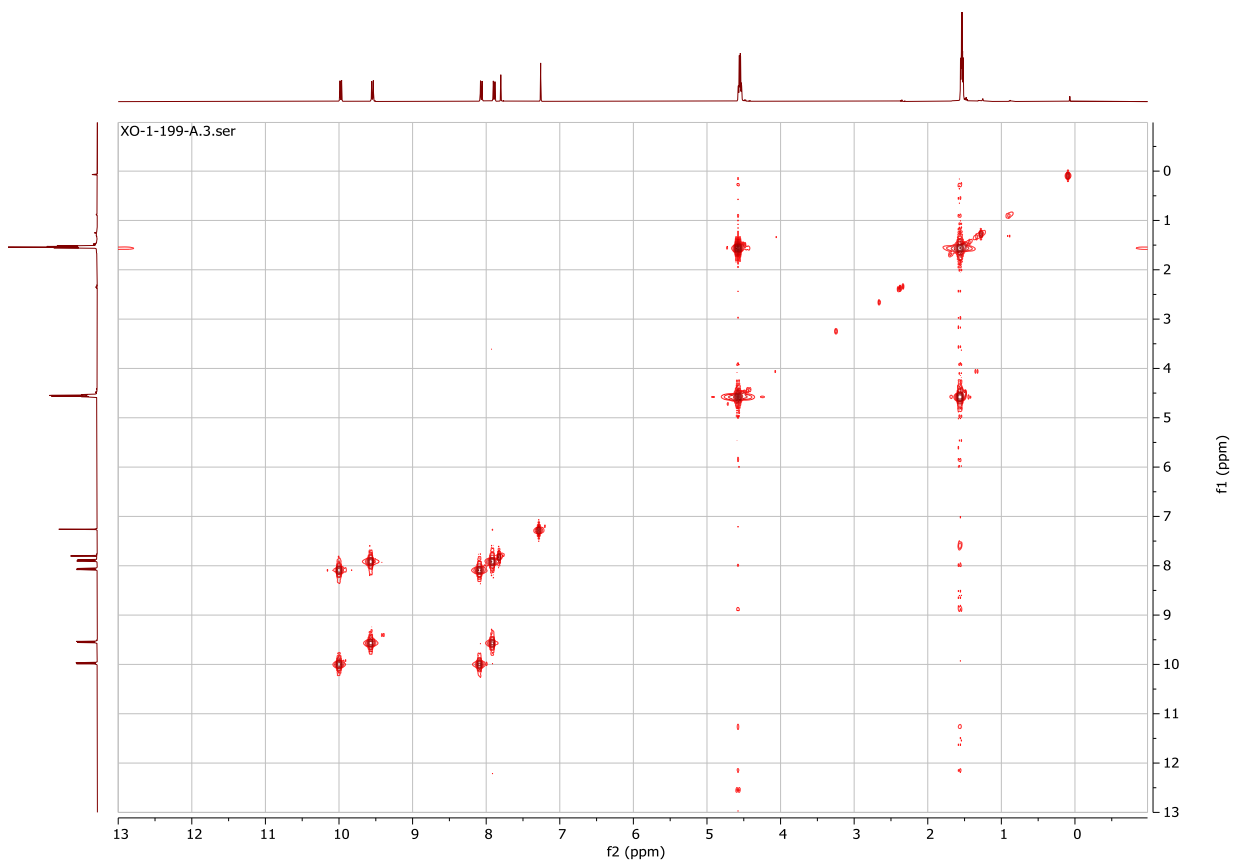
Figure S11. COSY 2D NMR (500 MHz) of 2-cyano-1,1',3,3'-tetraethoxycarbonyl-2'-mercapto-6,6'-biazulene in CDCl$_3$ at 25°C.
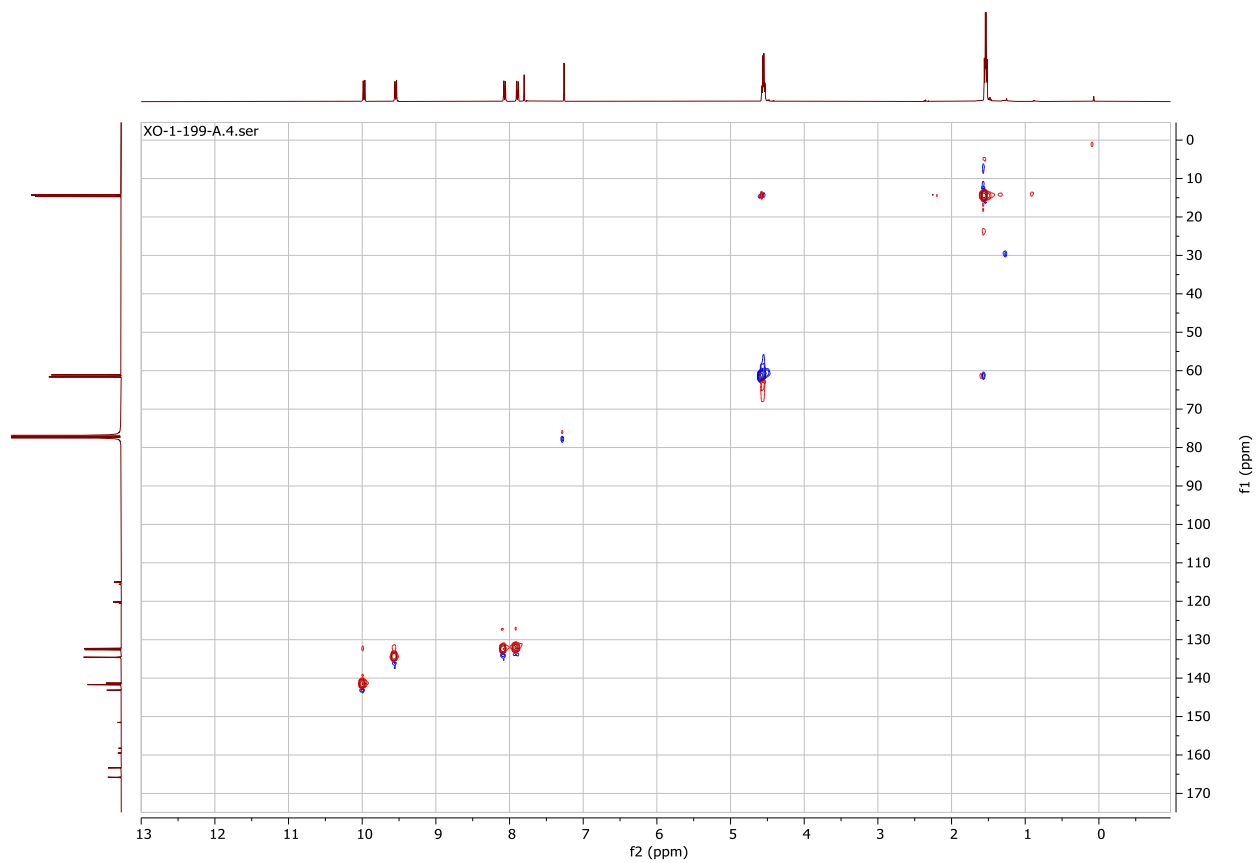
Figure S12. HSQC 2D NMR (500 MHz) of 2-cyano-1,1',3,3'-tetraethoxycarbonyl-2'-mercapto-6,6'-biazulene in CDCl$_3$ at 25°C.